Modern Raman spectroscopy for investigation of host-pathogen interactions

by

Michael Andreas Ochsenkühn

Doctor of Philosophy

UNIVERSITY OF EDINBURGH

November 2010

Declaration of Authorship

I, Michael Andreas Ochsenkühn, declare that this thesis titled, "Modern Raman spectroscopy for investigation of host-pathogen interactions" and the works presented in it are my own. I confirm that:

- This work was done wholly or mainly while in candidature for a research degree at the University of Edinburgh.
- Where any part of this thesis has previously been submitted for a degree or any other qualification at this University or any other institution, this has been clearly stated.
- Where I have consulted the published work of others, this is always clearly attributed.
- Where I have quoted from the work of others, the source is always given. With the exception of such quotations, this thesis is entirely my own work.
- I have acknowledged all main sources of help.
- Where the thesis is based on work done by myself jointly with others, I have made clear exactly what was done by others and what I have contributed myself.

Signed: _____

Date: _____

"Don't think about the problem, think about the solution!"

fic. character First Order Wizard Zedicus Zoriander, by Terry Goodkind

Abstract

Biomedical sciences are in need of more versatile and more sensitive approaches for research and also for diagnostic purposes. In particular, intracellular detection and imaging of disease relevant proteins is a challenge. Although the state of the art method of intracellular imaging is fluorescence, it suffers from several drawbacks. Raman is an alternative imaging modality and this work investigates the use of different Raman techniques for detection and imaging of cellular constituents. In one aspect of the work, surface-enhanced Raman spectroscopy using gold nanoshells excitable at a wavelength of 780 nm was investigated. Initially the investigation of the uptake of the 150 nm diameter nanoparticles showed that NS are taken up voluntarily by a non-standard endocytosis mechanism into mammalian fibroblast cells. Furthermore it was shown that internalized particles have no detrimental influence on cell growth or cell viability. That these nanoparticles are non toxic was further confirmed by testing for markers of apoptosis and necrosis. Preliminary surface-enhanced Raman spectroscopy (SERS) studies produced spectra from intracellular compartments with an enhancement factor of 10^{10}. To yield high specificity of the intracellular Raman protein sensor, two different approaches were studied. The first is based on the application of DNA aptamers which form a stacked G-quadruplex on target protein binding. A SERS sensor based on the well characterized Thrombin binding aptamer (TBA) yielded high reproducibility, high target specificity, and a limit of detection down to 0.1 fM. Further studies on a similar stacked G-quadruplex forming aptamer confirmed that observed detection signal is produced by the aptamer assuming its secondary structure but also showed that the stabilization and formation of the G-quadruplex secondary structure is strongly buffer dependent. A second sensing approach was based on a peptide (a3(IV)NC1) influential in Goodpasture's syndrome, an autoimmune disease. With the help of this peptide we found that an intracellular redoxpotential of -200 mV is necessary to make it accessible for the protease Cathepsin D. We found that SERS sensing has the ability to study the binding of Cathepsin D, its activity and with the help of a synthesized amino-acid SERS library the direct detection of the remaining peptide products. Finally this work concludes with imaging the changes of lipid droplet structure and distribution in fibroblast cells during the infection process of the murine cytomegalovirus (MCMV) in fixed and in living cells by coherent anti-Stokes Raman based on a Synchro-lock phase coupled

setup. This showed that CARS imaging is able to non-invasively investigate the changes of lipid structures during different stages of the infection process and therefore promises to be a valuable tool in biological research.

Acknowledgements

This work involved many people which I'm grateful for advice, discussion and ideas. Although I will try to remember everyone it might be that I wouldn't be able to thank everyone here personally.

First of all I want to thank my supervisor Dr. Colin Campbell, who gave me the opportunity to work with him on this exciting very versatile project. I'm especially grateful for the freedom he granted me, making it possible to develop my own ideas. Of our workgroup I want to mention Helene Stoquert, who always held up the spirits, Craig Auchinvole and Alessandro Ceroni, my fellow PhD companions, but also the master students, like Joanna Borek, for interesting discussions. A big thanks also goes to the workgroup of Prof. Eleanor Campbell, who gave me the opportunity to work with them and use their equipment and a special thanks to Oleg Nerushev, Andrei Gromov and Johan Ekweis for their help. Richard Phelps of the QMRI in Edinburgh I have to thank for supplying me with an application for my work and therefore the possibility to come to a successful close of the project.

Also I have to thank Professor Kishan Dholakia of the University of St. Andrews and his group for fruitful work we conducted together especially Dr. Philip Jess who made first investigations possible. Here I also have to mention our collaborators from the Division of Pathway medicine under Professor Peter Ghazal, in particular Dr. Sarah Rodriguez who introduced me into the exciting world of tissue culture and was a very good teacher. But also all others like Mathieu Blanc, Diwakar Kumar, Dr. Kai Kropp, Michael Chisholm and Paul Lacaze with whom working was always a pleasure.

Further appreciation goes to Iain Robinson, Chrissy Wong, Hugh Vass from COSMIC for the very interesting work we were conducting together and Dr. Andy Downes from Dr. Alistair Elficks workgroup for allowing me to use some of their facilities.

On a more personal note I would like to thank my grandmother Walburga and my uncle Franz, for their support and encouragement during the whole time. Not to forget are all the people which make live enjoyable during hard times but are also there to celebrate when the lab is treating you well for once.

Contents

List of Figures

List of Tables

Abbreviations

3T3	**3**-day **T**ransfer, inoculum **3** x 10^5 cells
A	**A**bsorbance
AA	**A**mino-**A**cid
AFM	**A**tomic **F**orce **M**icroscopy
APTES	3-**A**mino**P**ropyl**T**ri **E**thoxy**S**ilane
AS	**A**nti-**S**tokes
BB	**B**inding **B**uffer
CARS	**C**oherent **A**nti-stokes **R**aman **S**cattering
CCD	**C**harge-**C**oupled **D**evice
CyA	**Cy**ste**A**mine
CS	**C**alf **S**erum
CTB	**C**ell**T**iter **B**lue
DMEM	**D**ulbecco's **M**odified **E**agle's **M**edium
EDC	1-**E**thyl-3-[3-**D**imethylaminopropyl]**c**arbodiimide Hydrochlorid
EDTA	**E**thylene**D**iamine**T**etraacetic **A**cid
EM	**E**lectro**M**agnetic
F	**F**luorescence
FLIM	**F**luorescence **L**ivetime **I**maging **M**icroscopy
FRET	**F***ö*rster **R**esonance **E**nergy **T**ransfer
FWHM	**F**ull **W**idth **H**alf **M**aximum
GDB	**G**-quadruplex **D**isrupting **B**uffer

GFA	**G**-quadruplex **F**orming **A**ptamer
GFP	**G**reen **F**luorescent **P**rotein
GSH	**G**lutathione
GSSG	**G**lutathione reduced
GTP	**G**uanidin **T**ri**P**hosphate
HS	**H**uman **S**erum
HNF	**H**olographic **N**otch **F**ilter
HCV	**H**epatitis **C** **V**irus
GNP	**G**old**N**ano**P**article
IE2	**I**mmediate **E**arly promoter **2**
IBA	**I**nsulin **B**inding **A**ptamer
IC	**I**nternal **C**onversion
ISC	**I**nter **S**ystem **C**rossing
MBA	4-**M**ercapto**B**enzoic **A**cid
MCH	**M**er**C**apto-**H**exanol
MPA	**M**ercapto **P**ropionic **A**cid
MOI	**M**ultiplicity **O**f **I**nfection
MCMV	**m**urine **C**yto**M**egalo-**V**irus
NIH	American **N**ational **I**nstitut of **H**ealth
NP	**N**ano**P**article
NS	**N**ano **S**hell
NS-TBA	**N**ano **S**hell **T**hrombin **B**inding **A**ptamer
NS-GFA	**N**ano **S**hell **G**-quadruplex **F**orming **A**ptamer
NS-4MBA	**N**ano **S**hell **4-M**ercapto **B**enzoic-**A**cid
NS-MCH	**N**ano **S**hell **M**er**C**apto-**H**exanol
P	**P**hosphorescence
PALM	**P**hoto**A**ctivated **L**ocalization **M**icroscopy
PBS	**P**hosphate **B**uffered **S**aline
PFU	**P**laque **F**orming **U**nit

hαT	**h**uman α **T**hrombin
RT	**R**oom-**T**emperature (298 K)
S	**S**tokes
SAM	**S**elf **A**ssembled **M**onolayer
SERS	**S**urface **E**hanced **R**aman **S**cattering
SEM	**S**canning **E**lectron **M**icroscopy
SPR	**S**urface **P**lasmon **R**esonance
STED	**ST**imulated **E**mission **D**epletion
TC	**T**issue **C**ulture
TBA	**T**hrombin **B**inding **A**ptamer
TCEP	**T**ris(2-**C**arboxy**E**thyl)**P**hosphine
TEM	**T**ransmission **E**lectron **M**icroscopy
TIRF	**T**otal **I**nternal **R**eflection **F**luorescence
TPF	**T**wo **P**hoton **F**luorescence
TTP	**T**hymidin **T**ri**P**hosphate

Physical Constants

Speed of Light	c	$=$	$2.997\ 924\ 58 \times 10^{8}\ \frac{m}{s}$
Planck constant	h	$=$	$6.626\ 068 \times 10^{-34} \frac{m^2 kg}{s}$
Dirac constant	$\hbar$	$=$	$1.054\ 571\ 628 \times 10^{-34} \frac{m^2 kg}{s}$
Ideal gas constant	R	$=$	$8.314\ 472 \times 10^{-34} \frac{J}{Kmol}$
Faraday constant	F	$=$	$9.648\ 534\ 15 \times 10^{4} \frac{C}{mol}$
Avogadro constant	N_A	$=$	$6.022\ 141\ 5 \times 10^{23}$

To my Grandma...

Chapter 1

Introduction

1.1 Investigations of biological samples by optical spectroscopy

Since the origin of man, we have been fascinated with the processes surrounding us and in particular "what makes us tick or sick". One of the most important pieces of information in earlier times was what is edible, what causes nausea or what gives a very early death, (which may have happened often). Nature has provided animals with a multitude of senses, which can warn us but also transmit pleasure and enjoyment. Although all of our senses are well developed, with astonishing olfactory and aural capabilities we have always tried to understand our surroundings with our eyes. Therefore it's no surprise that increasingly sophisticated devices have been invented to visualize and understand what we could not see with our bare eyes. However, before devices could be designed, which could be used to help us see even better, an understanding of what "seeing" is had to be developed. As far back as 300 BC, Euclid developed a hypothesis that rays emanate from our eyes, touching the objects in our view. Not long after, the great mathematician Archimedes of Sicily (287-212 BC) who is known to have investigated reflection and refraction, and is said in legend to have built a device to bundle sunlight and using its energy to destroy Roman war ships.[1] The Roman emperor Nero some two centuries later (37-68 AC) was reported to wear a monocle to watch battles

to help with his short sightedness; this gives a hint that the concept of lenses had been known at this time. Ptolemy (Claudius Ptolemaeus, 85-165 AC) investigating refraction, found the small angle approximation to Snell's law, which states the relation between angles of incidence and refraction at the boundary between two different media, ($n_1 sin\Theta_1 = n_2 sin\Theta_2$), but he still held Euclid's hypothesis. This idea was finally laid to rest by the Arab Scholar Abu Ali Hasan Ibn al-Haitham (965-1040) who also described the increase in apparent size of sun and moon near the horizon and whose works had great influence in Europe.

Modern optics probably had its start with Roger Bacon (1220-1292 AC), lecturer at the University of Oxford, who experimentally proved the principles of reflection and refraction. Later the German Johannes Kepler (1571-1630 AC) known for his explanation of the movement of planets, was also the first to give a correct explanation of how eyeglasses work, and explained the function of pupil, cornea and retina. His life coincides with the appearance of telescopes, patented 1608 by Hans Lippershy, and also the first reported microscope which was invented by the Dutchman Hans Jansen in 1595. At this point the paths of optics divided. Telescopes were used by Galileo to investigate what happens outside the spacecraft we call earth and established his heliocentric system which led later to the Copernican system. Furthermore Newton, in all his self-doubt and paranoia, could not have proven the laws of gravity without looking beyond the limits of our world comparing the motions of other planets. The other path follows the development of the microscope which allows us to see smaller objects than can be seen with our eyes (200 μm). Microscopes quickly developed and after only ca. 100 years Antonie van Leeunwenhoek (1632- 1723), (who published an impressive 375 papers with the English Royal Society), reached magnifications of up to 300 times. He discovered red bloodcells (1673), infusoria (1675), spermatozoa (1677) and bacteria (1683). Improvement of the established microscope systems to a spaced lens system by Joseph Jackson Lister (1786-1869) corrected chromatic aberration and tackled spherical aberration as well, allowed him to observe shape differences of mammalian blood cells. Around the same time Gauss provided the mathematical basis of optical imaging theory and with the availability of reproducible high quality microscopy systems, from the company founded by Carl Zeiss, contemporary microscopy was born.[2]

Like our eyes, bright field microscopy has its limitations which are mainly caused by the wave nature of light. We are only able to observe dark or strongly refracting objects down to a minimal size of 0.2 μm, with a loss of clarity for everything that is outside the focal plain. Therefore it is no wonder smaller objects like virion particles, were only discovered relatively recent. Techniques enhancing, for example, image contrast or tackling the diffraction limit problem, like oblique illumination or dark field microscopy broadens the range of applications for microscopes to a degree. Even the use of electron microscopes suffers from limitations in the information that can be obtained i.e. shapes and forms can be discerned but biological processes or interactions of (bio-)molecules cannot be defined. However we are not at the end of the capabilities of microscopes. To this point we have only looked at one dimension. The second dimension concerns the nature of light itself and the fact that the image we look at through a microscope carries much more information than a standard microscope can observe.

Spectroscopy depends on diffraction, the ability to separate light into its components, as observed by Francesco Maria Grimaldi who found that light can "break into pieces".[3] Newton stated that light consists of small particles with different sizes, which only interact weakly with mass, as did Abu Ali Hasan Ibn al-Haitham before, calling the light particles "corpuscles". The first diffraction grating used by James Gregory (1638-1675) was a bird's feather and Thomas Young used two closely spaced slits and was able to deduce from the observed interference the wave nature of light. With this knowledge Christiaan Huygens postulated a theory of light based on rays of light consisting of waves, which was supported by Fresnels calculations.[4] The most common view of light as electromagnetic (EM) radiation goes back to Michael Faraday (1845) who observed that linearly polarized light is rotated when moving along the magnetic field direction in the presence of a transparent dielectric (Figure 1.1) with λ being the wavelength, E the amplitude of the electric field and M the amplitude of the magnetic field. He also postulated that light was EM waves of high-frequency able to travel in a vacuum. This led James Clark Maxwell to discover that EM waves travel at constant speed and described electric and magnetic fields by deriving equations which were then confirmed experimentally by Heinrich Herzt. The final missing part is Einsteins description of energy and therefore also light in special relativity with $E=mc^2$, which confirms

the particle character of light. Planck came up with the black body radiation theory, and postulated the quantum theory with E=hf=hc/λ, which could nearly explain every phenomenon of light and gained him the Nobel prize in 1918.

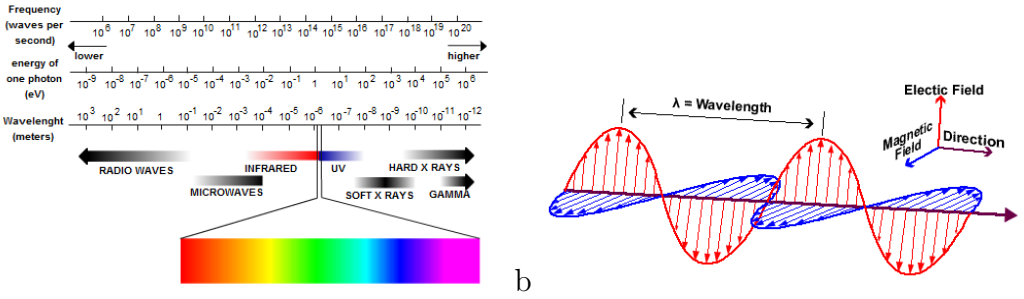

a b

FIGURE 1.1: a) The spectrum of light, with the region of visible light between 400-700 nm (violet to red). b) Depiction of electromagnetic radiation with the wavelength λ its electric field component and the magnetic field component.[5]

Looking at these different approaches to understand the behavior of light, we can state that light can be seen as electromagnetic radiation and possess four main components, intensity, wavelength, polarization and phase. The human eye can only perceive light with a wavelength between 400-700 nm and therefore limits the microscopically observable range. When light encounters matter (particles, molecules, atoms) all its properties play a role, but the most important fact is that light is always interacting and not simply reflected. This basically means light is in every case absorbed, and is either backscattered without change, elastic or Rayleigh scattering, or is transformed into EM radiation of different energy, inelastic scattering with shorter or longer wavelength anti-Stokes/Stokes scattering. These are immediate processes which occur in femto-seconds. There are also processes which depend on the electronic structure of the interacting particle/molecule actively converting the incident light into different forms of radiation (fluorescence) and internal conversion (IC) like rotation, translation and vibration. Another emission type called phosphorescence can only follow an inter system crossing, spin inversion into an excited triplett state (10^{-7} - 10^{-5} sec). The Jablonski diagram helps describe these different processes as shown in Figure 1.2.[6]

Now that we have shed light on light we can think about how this helps us to understand biological processes. To understand medical or biological processes

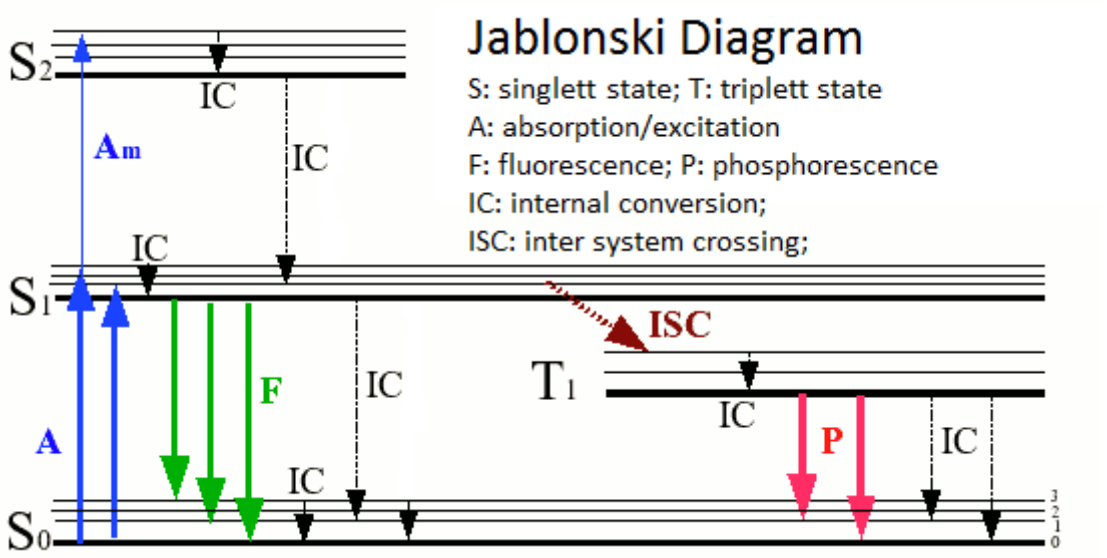

FIGURE 1.2: Jablonski diagram explaining the different transition processes leading to fluorescence and phosphorescence emission. Fluorescence only occurs from the first excited state to the groundstate but only from the first electronic state (0) and therefore follows internal conversion (IC) in cases of higher electronic states. In the case of phosphorescence an inter system crossing (ISC) to a triplet state is needed before emission can happen.

molecular imaging is used in modern applications, which is able to elucidate, physiological, like bloodstream, metabolic, in the sense of compound uptake into cells, or targeted questions, for example which kind of markers can be found on different kind of cells.

1.2 Modern molecular imaging techniques

Molecular imaging is based on the use of molecular probes or biomarkers in very low concentrations to detect biological processes without disturbing their function.[7] Imaging techniques can be categorised into radiolabeled, magnetic resonance imaging (MRI) and optical techniques. Radiolabeled and MRI techniques are widely clinical used but still undergo ongoing improvement. Optical techniques are for now mostly used in research areas and just recently emerge into clinical areas. The different techniques have characteristic strengths and weaknesses which will be reviewed in the following.

1.2.1 Clinical imaging

Radiolabeled techniques are widely used in clinical diagnostics and applications vary from perfusion, viability or myocardial blood flow studies, but also allow targeting of apoptosis, stem cells and metabolic pathways. They are based on the labeling of compounds specifically taken up for example by cancer cells labeled with weak radioactive isotopes. The radiolabels consist of certain istopes of atoms like, ^{11}C, ^{15}F, ^{123}I, or heavy metals like ^{111}In, ^{64}Cu, ^{68}Ga. Before application the labels have to be generated and can only be used for a very short time described by their half life time, eg. ^{11}C 20.39 min.[8] Therefore the application timeframe is very short and is even shorter as the labeling has to be done of site as well as the handling is hazardous not only for the radiochemist but also for the patient which limits the frequent use of the technique on one person. The two main methods here are positron emission tomography (PET), which is based on $\beta+$ emission and transformation with an electron into energy and single photon emission computed tomography (SPECT) in which γ radiation is detected directly. Their resolution lies at 4-5 and 10-16 mm, respectively.[9] PET and SPECT are still able to detect down to 10^{-11} - 10^{-12} molar and 10^{-10} - 10^{-11} molar, respectively, and minimally perturb the biological system.[8] Application to the patient also tends to be a challenge as the radiolabels not only have to be transported quickly and specifically to the target tissue but also has to be excluded out of the system as fast as possible to keep the radiation damage, produced by the ionizing irradiation of the labels, as low as possible. Another very powerful imaging modality is MRI. It provides excellent soft tissue contrast. When a material (such as tissue) is placed within a strong magnetic field, (1.53 Tesla are common) the proton spins align to create a multitude of dipoles oriented in parallel to the main magnetic field direction.[8] For localization contrast agents with magnetic moments, like Ga^{3+}, Mn^{2+}, Fe^{3+}, are used, but also present a pharmacological challenge, as heavy metals need strong chelators to render their toxicity innocuous. MRI can obtain very good resolution of 10-100 μm and tissue transmission, but lacks high sensitivity as a 10^{-3} - 10^{-5} molar of agent are needed. A combination of techniques like PET-MRI allows for high specificity and very good spatial and real time resolution, but also combine their major drawbacks, like costly machinery, hazardous and low contrast through

free label.[9] Optical imaging, is cost effective and widely available and might evolve into the future for clinical imaging as well.

1.2.2 Optical imaging

Optical imaging techniques are able to tackle technical disadvantages of state of the art clinical imaging techniques, as the hazards of radiolabeling or the costly instruments for MRI, and promise gentle and inexpensive ways of imaging. For now optical techniques are used in many preclinical trials involving labeled target molecules applied for different kinds of medical questions. Applications range from monitoring dissemination of viral and bacterial infections, chronic and acute inflammation, tumor development, drug discovery and gene expression on a research tissue culture or animal model scale. The two dominant techniques are fluorescence or bio luminescence, but others emerge involving nanoparticles. Bioluminescence imaging (BLI) is a very attractive technique for applications in imaging of bacterial and viral infections and can give insight in acute disease progression or response to drugs.[10] The acquired signals stems from an enzymatic reaction between, mostly, the firefly (*Photius pyralis*) luciferase and its substrate, luciferine and is driven by adenosine-triphosphate (ATP). For the protein to be expressed in the organism of interest the genetic information has to be encoded, therefore cloned, into the organism, which is relatively simple in bacteria and viruses also the yeast *Saccharomyces cerevisiae* but still stays a challenge in mammalian cells as reported by Gupta *et al.* (2003).[11] Also, the luciferine has to be provided for the reaction, but can be easily applied by intra venal injection and is known to be taken up into tissue, even in the placenta.[12] The advantage of this technique is that a reasonable strong signal can be obtained spontaneously without separate excitation by an external light source, and therefore gives high contrast, but only the red part of the luciferine luminescence with a peak emission at 560 nm can be used for tissue imaging because of attenuation. Red shifted luciferine variants are under development and will tackle this issue, which limits the technique, to date, to subcutaneous investigations.[13]

Fluorescence is very powerful and different techniques developed to deal with different applications like F*ö*rster Resonance energy transfer (FRET), total internal reflection fluorescence (TIRF), Fluorescence life time imaging (FLIM) or the the very exciting super resolution fluorescence imaging techniques, like the illumination-based simulated emission depletion (STED)[14] or probe-based photoactivated localization microscopy (PALM)[15] which are able to image down to 10s of nms.[16, 17] They all have in common the use of a dye molecule which has to be excited by light of a certain wavelength and emits red shifted light as described above. The strengths of fluorescence microscopy lies first of all in its versatility. FRET depends on the non-radiative energy transfer from one excited fluorophore, donor, to another, acceptor, which is, as a result, emitting fluorescence. The energy transfer occurs when donor/acceptor are in close proximity to each other and therefore allow the investigation of molecular interactions or conformational changes greater then 100 $\mathring{A}$, 10 nm, and through that can give information about protein function.[18] For example it was recently reported that FRET was used to show the connection between the breast cancer metastasis suppressor BRMS1 and a cytosolic sorting protein SNX6 by Rivera *et al.*. [19] TIRF is a very gentle technique, low photodamage, with high signal-to-noise ratio, to obtain localized information through illumination through a prism producing an evanescent wave for samples of a depth of 100-200 nm, and allows studies of the cellular membrane[20] as for example reported by Hoover *et al.* (2009) investigating cell adhesion on gold surfaces.[21] FLIM is able to acquire data about all sorts of environmental properties, like pH, viscosity, refractivity, molecular collisions and rotations independent of signal intensity, ergo dye concentration, and can be used in thick samples.[17] For example it has been used to distinguish different types of fluorophores in cancerous tissue.[22] The mentioned super resolution imaging, which allows observation of structures smaller than 250 nm along the x-y axis, and makes it for the first time possible for optical techniques to overcome the diffraction limit.[16]

Fluorescence imaging is normally done in tissue culture *in vitro* set-ups, seldom *in vivo*, as light of lower wavelengths is absorbed by tissue or leads to auto fluorescence. The development of NIR fluorescence dyes has made further entry into this area possible, but still disadvantages, like photobleaching or the impact of

labeling on protein structures and living organisms, prevails. Quantum dots consist of a core made of from groups IIVI (e.g., CdTe and CdSe) and III-V (e.g., InP and InAs) of the periodic table and are nano meter sized particles which also emit a fluorescence signal. They can be tuned and the signal enhanced by an inert layer of ZnS also decreasing the toxicity of the heavy metal cores. They have the advantage that their photon efficiency is higher than of ordinary fluorescent dyes and also are less prone to photobleaching. They can furthermore be designed for different wavelengths and are easily attachable to every kind of molecule and are often used for the labeling of membrane proteins. Live cell imaging is possible with QD, and a very impressive study was carried out by Dahan *et al.* (2003) examining individual glycine receptors (GlyR) in rat spinal cord neuronal cultures showing their potential *in vitro*.[23] QDs are also on the verge of *in vivo* imaging applications satisfying the need for cancer-specific biomarkers as for example reported by Kim *et al.* (2010).[24, 25] Not only fluorescent nanoparticles (NP) can be used for imaging, but also metal nanoparticles which have special properties. The use of metal NPs, especially inert goldnanoparticles (GNP) is various as their properties depend on their size and shape, like spheres, rods,[26] urchins,[27] prisms,[28] disks,[29] shells,[30] and stars.[31] The ease of preparation, in most cases, makes them attractive not only for imaging but also immunostaining,[32] labeling,[33] sensing[34] and drug delivery.[35] The origin of their different properties will be explained further on, here only a short insight in their use in state of the art imaging. NPs can also be specifically attached to molecules, but in contrast to the above techniques absorb light, act as acceptors, rather than emit it. This leads to signal depression when light of the right wavelength is used and is used for quenching. A combination of QDs and metal NPs can also be used in the same way as FRET in which close proximity of both leads to a radiationless energy transfer between the two particle types, QD as donor and GNPs as acceptor, which leads to a quenching. This particle resonance energy transfer (PRET) has been used by Oh et al. (2005) in a simple biomolecule inhibition assay between biotin and streptavidin.[36]

All the above mentioned optical imaging techniques rely on staining with dyes or contrast agents which allows indirect detection via one label or combination of labels. This always includes elaborate preparation, linking of targets with agents,

or introduction of agents into the sample of interest. The information, although multiplexing is possible, can only give information about one specific event and what we look at is secondary information, not the molecule of interest itself.
In this work we are facilitating a different approach, giving first hand information of the molecule or process of interest. Raman spectroscopy in general is able to give direct information of molecules and their surroundings and recent developments help overcoming limitations of Raman spectroscopy with higher sensitivity and greater versatility. The limitations can be overcome by using modern instruments or modern techniques like surface-enhanced Raman spectroscopy (SERS) or coherent anti-Stokes Raman scattering (CARS) which are investigated for the application with biological systems in this work.

1.3 Introduction to Raman spectroscopy

1.3.1 The Raman effect

Raman spectroscopy is an inelastic scattering technique that probes the vibrational energy levels within molecules and was first reported by C.V. Raman, who was awarded the Nobel prize in Physics in 1930 for the discovery that light changes its wavelength on interaction with matter. Nowadays, Raman spectroscopy is an established technique and is regularly used in chemistry to investigate chemical substances and is often used in combination with infra-red absorption spectroscopy as the two techniques are mutually complementary i.e. vibrational transitions that are Raman active are not IR active (Figure 1.3). In Raman scattering, the light interacts with the molecule and distorts (polarizes) the cloud of electrons round the nuclei to form a short lived state, called a 'virtual state'. This state is not stable and the photon is quickly re-radiated.[37] (Figure 1.3c,d). The detected energy changes in vibrational spectroscopy are those required to cause nuclear motion and therefore can probe the elemental composition of a molecule. This all sounds like the perfect technique for analytical label-free spectroscopy, but its major drawback is a very low probability for setting a molecular vibration in motion, only one in 10^6-10^8 photons are scattered inelastically. Thus the signal is extremely weak and

can be obscured by fluorescence or the Rayleigh scattered light. However with modern spectrographs, CCD (charge-coupled device) cameras and optics, this is becoming less of a problem and Raman is emerging as an exciting technique for probing every kind of system, even proving very valuable for biological studies.[38] The main advantages of Raman spectroscopy are that the technique does not depend on the excitation wavelength allowing the experimentalist to choose a wavelength suitable for the sample under study and the ability to probe large biochemical compounds, such as cells or tissues, without the need for markers. Raman spectroscopy is a versatile technique capable of engaging large ensembles of molecules, however, it can take a reasonable amount of time to record a good signal, on the order of minutes, and has difficulty recording signals from single molecules.[39]

a

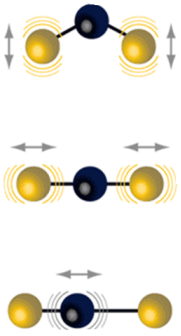

b

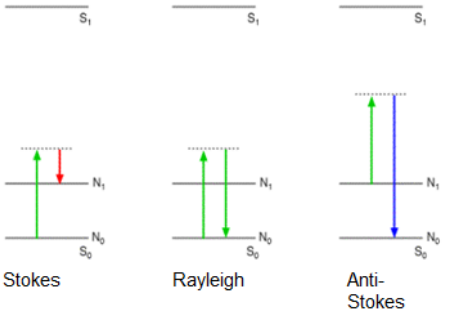

c

$$I_{S_R} \propto \left(\frac{\delta\alpha}{\delta t}\right) \qquad (1.1)$$

I_{S_R}	Raman scattering intensity	
α	Polarisability	
t	Time	

d

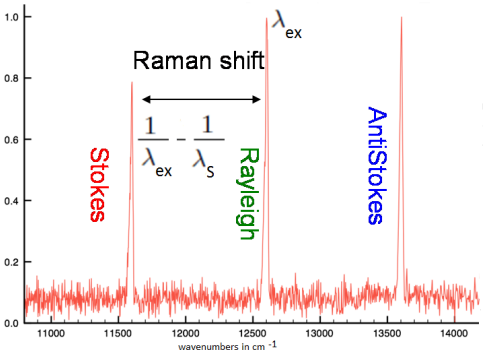

FIGURE 1.3: a) Raman active vibrations of a three atomic molecule (like H_2O). b)Excitation processes leading to Stokes, Raleigh and Anti-Stokes scattering. c) Equation for the selection rule of Raman active stretches, change in dipol-moment. d) Stokes and anti-Stokes shift of the inelastic Raman scattering.[5]

1.3.2 Surface-enhanced Raman Spectroscopy (SERS)

Surface-enhanced Raman spectroscopy is a scientific advance which was found by chance as Fleischmann *et al.* (1974) tried to measure Raman spectra of pyridine on a electrochemically roughened silver surface.[40] The measured signal was much higher than expected and they explained this finding on the basis of the amount of molecules in the excitation beam compared to polished surfaces. It took until 1977 that a concentration-independent enhancement was proposed, by van Duyne.[41] Nowadays SERS is often employed in order to increase the sensitivity and signal strength of Raman Spectroscopy as it can produce a Raman signal enhancement of up to 10^{14}.[42] This massively improves the sensitivity and opens up the possibility of rapid single molecule studies. The enhancement of the Raman signal occurs when a molecule is in close proximity to a metal nanoparticle or nano-structured metallic surface, silver and gold providing the largest enhancement (silver > gold>copper>lithium,sodium), due to their surface plasmon resonance.[42] SPR happens when a metal nano-structure, at its boundary to another dielectric, is excited by light. The free electrons on the metal surface are excited to surface plasmon polaritons, which can be simply described by surface oscillating evanescent waves of charge differences (Figure 1.4), which store the energy of the incoming light close to the metal surface.[43] In the case of SPR the wavelength of the light corresponds with the resonance frequency of the surface plasmons depending on size, roughness and form of the metal structures. For SERS there are two theories that attempt to explain the enhancement of the Raman signal. The first is the electromagnetic theory that describes an interaction between the incoming radiation and the plasmon resonance causing an enhancement in the local electric field as seen in Equation 1.3 and the second is a charge transfer where a bond is formed between the metallic surface and the molecule. For the molecule to experience an increase in its polarisability and therefore its Raman cross-section it has to be orientated perpendicular to the surface plasmon wave vector. Therefore only some of the Raman active modes of a molecule near the metal surface are enhanced. It is commonly agreed that the enhancement is caused not by just one of these mechanisms but that both contribute to the signal increase of them.[43] SERS is a powerful technique in the study of single molecules[44] and has been used in applications such as biohazard detection[45]

through to the study of biomolecule structures, e.g. proteins.[46] or even DNA sequence detection[47]. Investigations of whole cells by SERS have been made, but only at locations in the cell where the gold nanoparticles can be found can be examined.[48]

$$E_r = E_0 \cos\Theta + g(\frac{a^3}{r^3}) * E_0 \cos\Theta \tag{1.2}$$

with

$$g = (\frac{\epsilon_1(\nu_L) - \epsilon_0}{\epsilon_1(\nu_L) - 2\epsilon_0}); \tag{1.3}$$

E_r	Energy of resulting EM surface wave
E_0	Energy of incident EM wave
Θ	Incident EM wave angle
a	Particle radius
$\epsilon_{1;2}$	dielectric constants of metal and dielectric at the metal surface
g	Constant related to the dielectric constants
ν_L	surface plasmon wave frequency

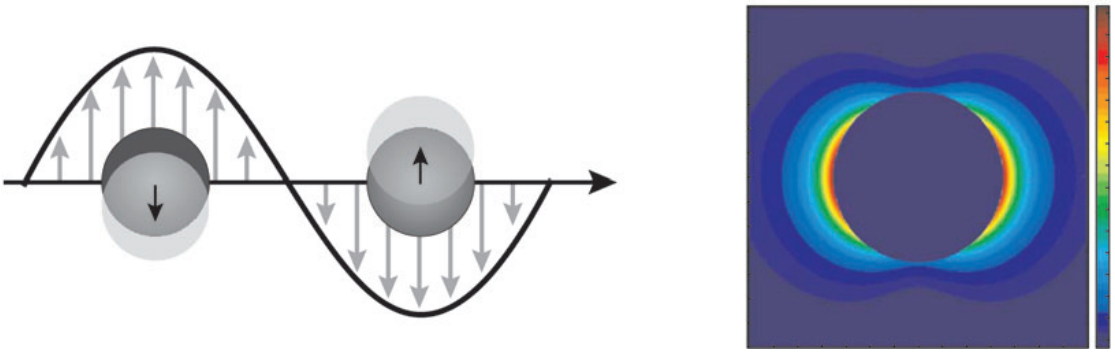

FIGURE 1.4: a) Illustration of the localized surface plasmon resonance effect. (b) Extinction efficiency (ratio of cross-section to effective area) of a spherical silver nanoparticle of 35-nm radius in vacuum —E—^{2} contours for a wavelength corresponding to the plasmon extinction maximum. Peak —E—^{2} = 85.[43]

1.3.3 Coherent anti-Stokes Raman Scattering (CARS)

CARS is a non-linear technique closely related to the Raman effect that employs pulsed lasers to examine the vibrational levels in molecules. CARS is normally employed in the study of samples that suffer from high interference as it enhances the anti-Stokes transitions and therefore blocks any red-shifted light transitions

like fluorescence. Anti-stokes transitions occur when a photon interacts with the atoms of a molecule in an excited vibrational state. The energy of the motion can then be transferred to the scattered photon, and this process manifests itself in the release of a photon with a shorter wavelength, higher energy. CARS is a pump-probe nonlinear technique that employs two pulsed lasers that have a wavelength difference corresponding to the energy of the Raman transition, to be probed. The two beams combine to force the molecule into the excited state thus when it relaxes, due to interaction with the probe laser, the photon it scatters will have the molecular vibrational energy, for that transition, transferred to it as shown in Figure 1.5. This technique results in a signal increase and the fact that the output is coherent means it is emerging as a popular technique for the study of traditionally difficult high noise samples and situations. CARS is a relatively new technique but has been applied successfully in the study of biological samples in applications such as three dimensional cell imaging [49] and has been shown to be endoscope-compatible in principle.[50] CARS is emerging as an important technique for examining the vibrational structure of previously challenging samples. However, the technique does require a complex laser set-up and there is a concern that applying pulsed sources to biological samples can lead to photon damage.[51]

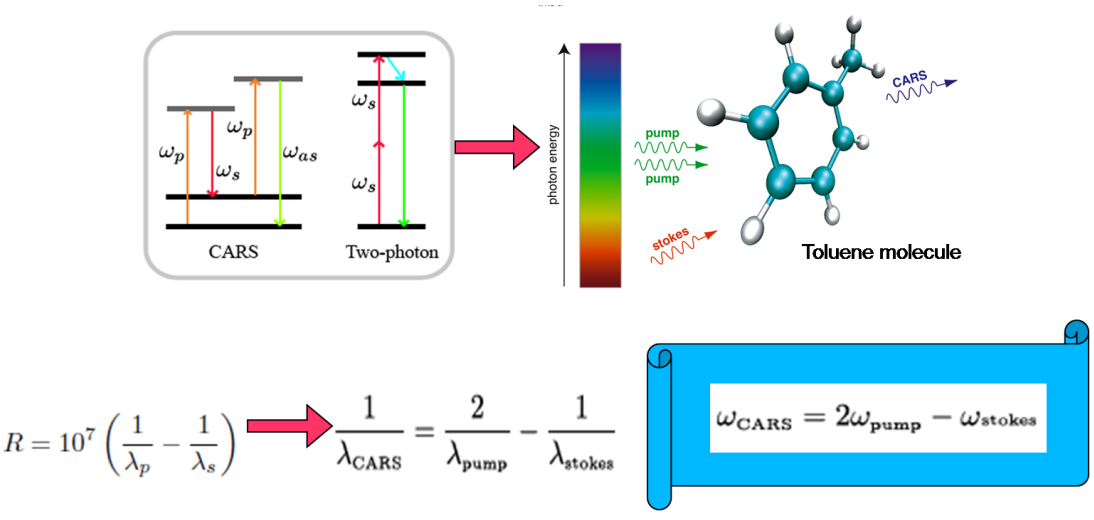

FIGURE 1.5: Development of excited state on toluene leading to Coherent anti-Stokes Raman Signal (CARS)

1.4 Biomolecular sensing

According to the IUPAC definition a biosensor consists of three different parts, biomolecule/transducer/physicochemical detector.[52] The first part is biological in the sense that the molecule is derived from a biological system. Here we find DNA, RNA or proteins in use. Very often and widespread are antibodies, because of their specific binding properties and ubiquity. But contrary to a misleading interpretation of their name "biosensor" the obtained information is not necessarily about the biomolecule which is bound to the transducer element, but rather gives information or simply is used as a binding partner for the molecule of interest. The transducer is basically a translator, converting a signal, like changes in the conformation of a protein, or environmental conditions, present pH or redox potential, into information that can be detected by a physical detector, like a CCD camera in the case of Raman spectroscopy. This is then the mentioned third element a sensitive piece of equipment reporting information obtained from the biomolecule via the transducer making its interpretation possible.

1.4.1 Biomolecules

Three different possible biomolecule types, antibodies, DNA aptamers and peptides, seemed to be attractive in particular for this work, because of their unique properties. Their origin, current applications and possible advantages and disadvantages for SERS based biosensors will be addressed shortly in the following sections.

1.4.1.1 Antibodies

Antibodies are globular proteins of ∼150 kDa possessing a binding specificity to a certain antigen. They are used by the immune system of vertebrate, for example in blood, to localize and inactivate foreign molecules, organism and viruses (Figure 1.6. The binding site has amino-acids modified with sugars, therefore they are also classified as glycoproteins. For their role in fighting pathogens they are also

called immunoglobulins or Ig's appearing in monomeric (IgD, IgE, IgG), dimeric (IgA) and pentameric form (IgM), and appear in different locations or for different purposes as for example IgE binding to allergens and protection against parasitic worms.[39, 53] In this work antibodies have not been investigated as the possible change in Raman signal was questionable, as they are large molecules and the areas of change might not lie within the Raman enhancing area of a few nanometers above the enhancing metal surface. Also the spectra of antibodies and target proteins may be similar. Never the less, a SERS sensor based on the observation of conformational changes on target binding of a antibody have been just recently reported and also prove the general feasibility of this approach.[54]

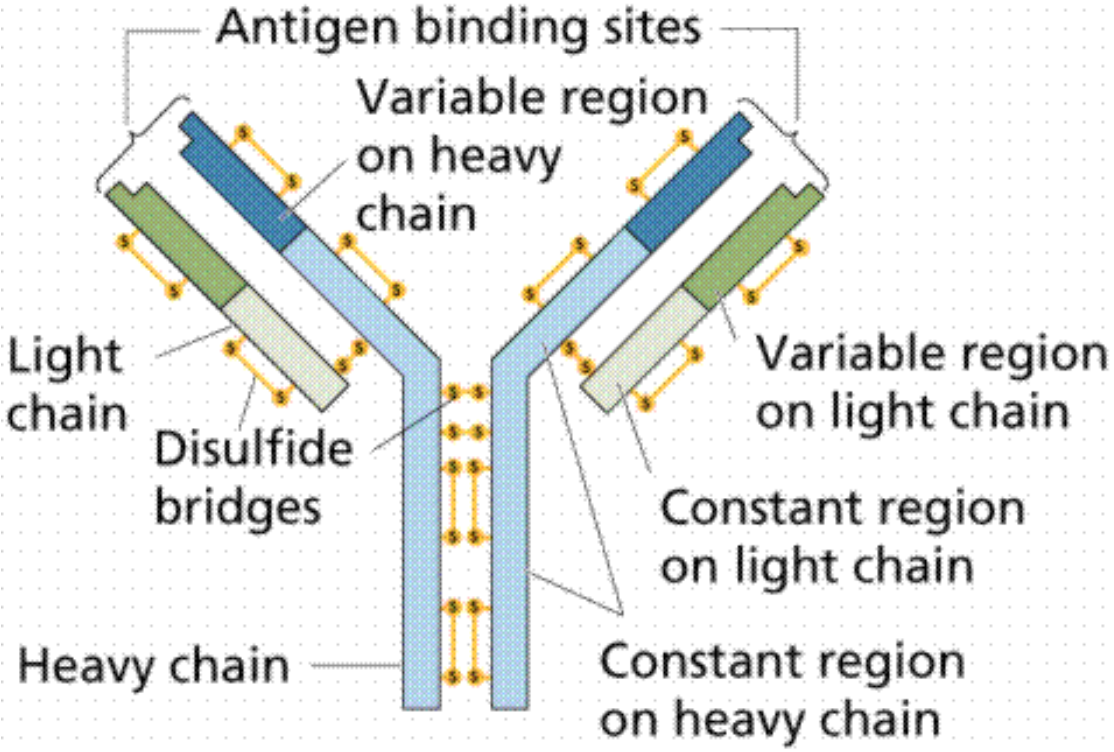

FIGURE 1.6: Sketch describing heavy and light chains of Antibody, the stabilizing disulfide bridges and the specific binding sites.[55]

1.4.1.2 Aptamers

Aptamers were first reported by Tuerk *et al.* and have found diverse applications varying from drugs to analytical applications since then.[56–58] There are two

different ways of selecting the oligonucleotides with the highest binding affinity, systematic evolution of ligands by exponential enrichment (SELEX) and a recently reported method called MonoLEX, both methods are presented in Figure 1.7. In the SELEX method the target molecule is incubated with the DNA pool, non-binding aptamers removed and binding oligonucleotides are amplified by PCR and used as the new DNA pool. This process is repeated up to 30 times until the ssDNA with the highest binding affinity has been found. MonoLEX takes an affinity column based approach, which only consists of one step, and has been used to obtain an apatamer specific for a viral protein.[59]. The advantage of using DNA for target binding lies in the different Raman signatures of DNA and protein molecules and also the novelty of investigating conformational changes by SERS.

1.4.1.3 Peptides

Peptides are short amino-acid chains up to a length of 100 AA. Peptides are used for signalling and have specific binding partners, receptors, antibodies and enzymes like proteases. They also assume regulatory functions, as in the case of the glutathione redox-pair (GSH/GSSG), which controls intracellular redox potential between -100 and -300 mV.[60] Peptides were used with the idea, that they are small molecules which fit easily into the SP range and therefore it should be possible to study small conformational changes. Although the success of this approach was unclear at the start of this part of the work, a very recent publication reported the detection of anthrax spores based on SERS investigating peptide conformational changes.[45]

1.4.2 Transducer element: Nanoparticles

For surface enhanced Raman spectroscopy - SERS, nanoscaled structures are usually either fixed onto large surfaces or free in suspension in the form of nanoparticles. These can appear in various forms, simple spherical particles, rods,[61] rice like shapes,[62] sea urchins[27] or even cages.[63] Their size can vary from 1-500 nm, which is important for their unique properties, in this case their ability to

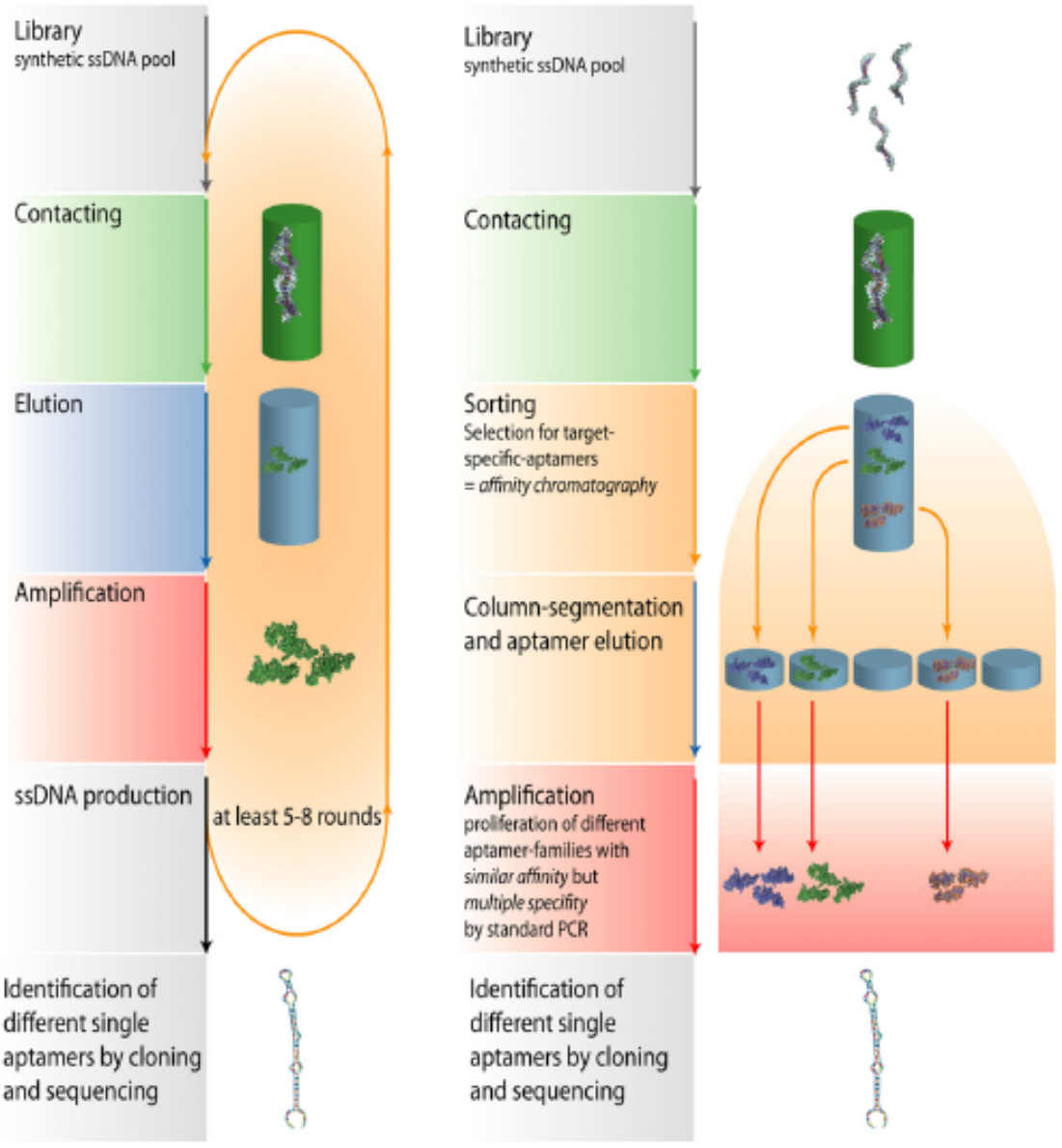

FIGURE 1.7: Graphical description of SELEX and MONOLEX apatamer selection methods.[59]

exhibit surface plasmon resonance. Nanoparticles for SERS are extremely versatile and can be used on surfaces in the form of arrays or in suspension. At high concentrations in solution they can help to detect tiny amounts of analyte and are also able to be introduced into cells for probing biological samples from mammalian cells to bacteria. Even the introduction into cells is possible and probing the intracellular environment for conditions like pH, localisation and cellular constituents, with tremendous promise for analytical applications.

Nanoshells are a certain kind of spherical nanoparticle which are designed of a dielectric core and a layer of surface plasmon providing nobel metal, whereas the core can range from solid materials like silica to hollow particles with "air" as dielectric[64, 65] and up to date Au,Ag and Cu as metal layers.[66, 67] This design allows to control the size, layer thickness, and through this the optical properties, extinction and absorbance and moreover has the advantage that in contrast to other nobel metal nanoparticles they do not need stabilizing agents, like citrate or poly-ethylene glycol, at least in the case of meso-scaled NS, core size bigger than 100nm.[68] A very important factor for the application of metal nanoshells is not only the ease in handling but also that their electronic and optical properties can be modeled on the one hand with the classic Mie-scattering theory but even more accurate with a theoretical method based on the time-dependent local density approximation (TDLDA) on the basis of the free electron cloud.[69–71] Halas *et al.* developed this kind of Au nanoshells, nowadays called Auroshell^{TM}, are commercially available, quality controlled and very reliable with a considerable enhancement factor of 10^{12}.[72] This is formed by first producing a layer of amino silane (APTES) on the surface of the silica which is then brought in contact with a solution of 1-3 nm Au gold particles, which attach to the surface. Finally the seeded gold particles are than merged together with an $HAuCl_2$ solution at reducing conditions and depending on the contact time and the reducing agents, like formaldehyde or Na_2S, layers of different thickness are formed as described.[73, 74] Figure 1.8 describes the process of the gold layer formation and the dependence layer thickness and absorbance the optical tunability.[75] Nanoshells have found a range of applications from, SPR sensing of interactions in blood,[76] over pH measurements by SERS,[77], for the enhancement of fluoresence signals[78] and also for SERS probing the interaction of ibuprofen, one of the most commonly used

pain killer drugs, with lipid bilayer membranes.[79] Very recently even the measurement of SERS signals inside NS has been reported by Zhang *et al.* (2009).[80] Another possible NS design which has been used for SERS was reported for the investigation of a naphtene-thiol with a coupled Ag-Au nanoshell.[66]

Depending on the chosen optical properties different applications for NS can be pursued. For example NS with a peak absorbance in the near infrared are advantages for work with biological samples, eg. cells or tissue, as these show very low absorbance in this region and also avoid the excitation of auto-fluorescence. A very remarkable application, the thermal ablation of cancer with antibody modified NS, exploits the increase in energy around the nanoparticles, to specifically destroy soft tissue cancers with great success.[81] Therefore as our aims is here to show the potential of Nanoshells for biological Raman spectroscopic applications the used particles are of 150 nm size, consisting of a silica core of 120 nm diameter which is covered in a ∼30nm layer of gold and exhibit a maximum absorbance at 780 nm.

1.5 Medical conditions of interest

The main motivation for the development of new biosensor and imaging techniques is the study of biological systems without much disturbance of normal mechanisms and behavior. As described above optical techniques hold huge promise to bring us to this point and therefore I describe now the three medically interesting topics on which this work was based.

1.5.1 Auto-immune diseases - Goodpasture's Syndrome

Goodpasture's Syndrome is an auto-immune disease which is characterized by glomerulonephritis in kidneys (inflammation of small blood vessels) and hemorrhaging of the lungs (leaking of blood vessels) and was described first by Dr. Ernest Goodpasture.[82, 83] Auto-immune diseases are a disfunction of the body's own immune system leading to recognition of own substances and tissues as foreign and their subsequent attack and destruction. In Goodpasture's syndrome the

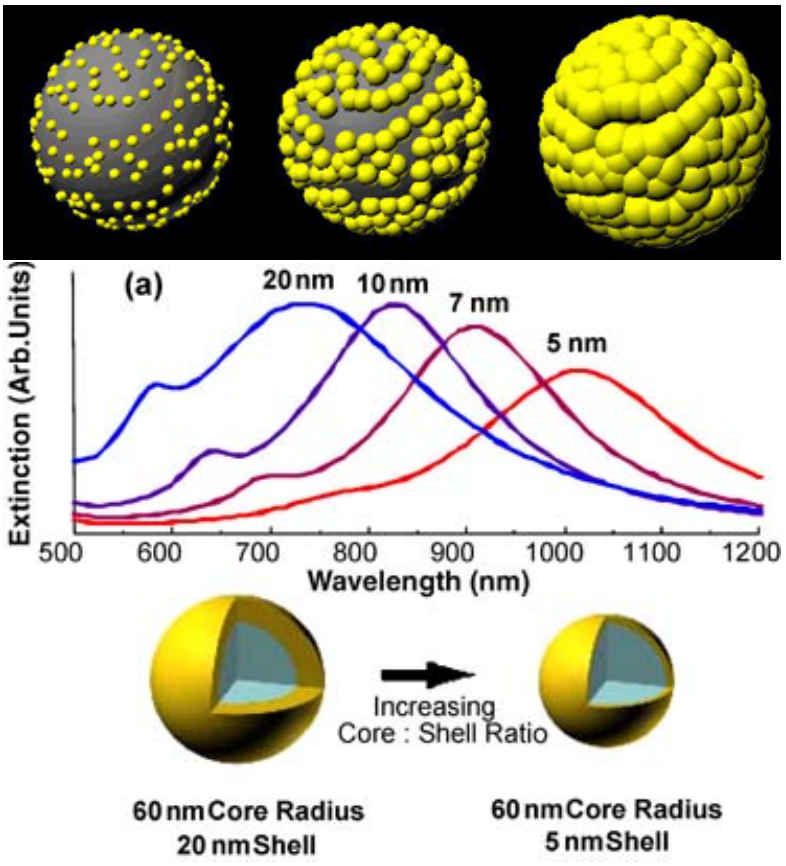

FIGURE 1.8: Nanoshells and their synthesis process. Optical tuneable Nanoshells.[72]

recognized antigen is an non-collagenous epitope of a collagen type IV protein, namely a3(IV)NC1. This peptide consists of around 20 AA, varying in length and sequence, depending on tissue and organism, and normally forms a finger-like structure stabilized by a disulfide bridge (Figure 1.9). When the peptide a3(IV)N1 is presented on the cell surface it stands as target for T-Cells which recognize cells presenting it as alien and attack them. Even healthy individuals show T-Cells which are sensitive to this antigen. In non-immuno-compromised individuals the presented α3(IV)NC1 peptide and other epitopes are rapidly diminished by self-tolerance mechanisms. In this case the aspartyl protease namely Cathepsin D cleaves the α3(IV)NC1 peptide to initiate further epitope processing to harmless fragments.[84] On the other hand certain conditions must exist for Cathepsin D to be able to engage in the cleavage of this peptide as it only can attack the peptide after it is linearized, meaning that the disulfide bridge must be reduced for it to

be able to bind and catalyse a cleavage. Therefore it would be useful information to study the conditions which lead to a change in the local redox environment. An analogue of the signaling peptide α3(IV)NC1 was used for the detection of human Cathepsin D and studies of redox-dependent conformational changes

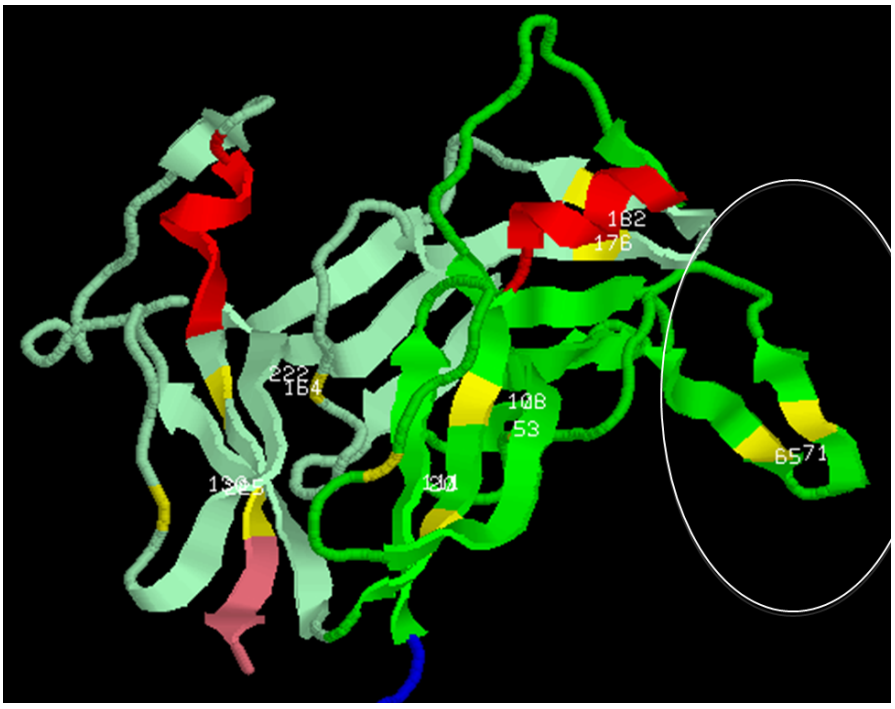

FIGURE 1.9: X-ray crystal structure of Collagen type IV protein with fingerlike structure of α3(IV)NC1 peptide highlighted by white circle with the yellow marked cystine bond between AA 65 and 71.[84]

1.5.2 Human Breast Cancer - the role of Cathepsine D and its precursors

Another disease which is interesting because of its prevalence over the population, with 176 cases of 100000 women in 2009, is breast cancer.[85] Breast cancer cells excrete Procathepsin D and to a lower extent Cathepsin D into the extracellular environment, where it is involved in tumor growth and metastasis. It was reported that although Procathepsin D has no or not much protease activity but is involved in metastatic cancer formation, the same has been shown for a proteolysis inactive Cathepsin D mutant.[86] In metastatic breast cancer cell lines the gene

for Cathepsin D is highly overexpressed, 2-50 times more than in non-cancer cell lines, leading to a high concentration of the protease in the cytosol. The activation of pro-cathepsin D is mediated by lysosomal proteases, therefore has to be transported after post-translational modification to the lysosome via mannose-6-phosphate (M6P) signalling to be activated. Through the high excess of the pro- and the activated form they are also secreted in excess and can be endocytosed by both cancer cells and by fibroblasts, via M6P-receptors and other as yet unknown receptors.[86] Unknown receptors are then responsible for the metastatic and mitogenic activity of Cathepsin D. This protease is also produced to a higher extent in (breast) cancer cells and is excreted into the extracellular environment.[87] For this reason the idea was developed to detect cancer by testing blood plasma, as cathepsin D levels are increased compared to healthy patients.[88]

In this work the MCF7, a metastatic breast cancer cell line,[89] will be used for the extra- and intracellular detection of Cathepsin D as a proof-of-principle experiment.

1.5.3 Host-pathogen interactions - Cytomegalovirus

Viruses are dependent on other organisms to replicate themselves, therefore can be seen as parasitic organisms. Their existence had great influence on the development of life. They interacted with organisms, challenged the immune system of every kind of creature, and exchanged information in the form of DNA/RNA. They also fulfill a regulatory function, holding populations in balance. Without viruses, evolution might have taken a different turn and life would look quite a bit different than we know it. These evolutionary aspects are still all speculative, but viruses need a host to maintain themselves.

Viruses can consist of two or three parts: genes in the form of DNA or RNA, a coating of protein which protect theses genes and some of them even another envelope comprising lipids and proteins which surround them in the extracellular environment. Directly after infection of a cell they start controlling the intracellular machinery to be transported to the nucleus, where they use the replicative

functions of the host to produce new copies of themselves. Followed by the re-assembly and the excretion of new copies of the virus. This whole extremely complicated process is still under intense research, especially on the side of host virus interactions to find new targets for the use in treatment and prevention of viral infections.
In this work, mouse cytomegalovirus, a β-herpesvirus, which possesses an envelope was used. The human strain of this virus is endemic and found in more than 40 to 80 % of the worlds population aged over 40 years. The latent virus can lead to severe infection in immuno-deficient individuals, e.g. the elderly or HIV positive. In prenatal infections it can lead to loss of hearing and is also connected to congenital blindness.[90] The reproduction process of this virus is nicely illustrated by the work of Mettenleiter *et al.* as described in Figure 1.10.[91]

There is still a need to find new methods which can safely acquire information about the interaction between host and pathogens, identifying the viral targets, describing the timeline of infection and getting deeper insight into the behavior of the cells and the defensive mechanisms of whole organisms. This was taken as one of the motivations for this work, to develop new, hopefully better, techniques for host-pathogen interaction research.

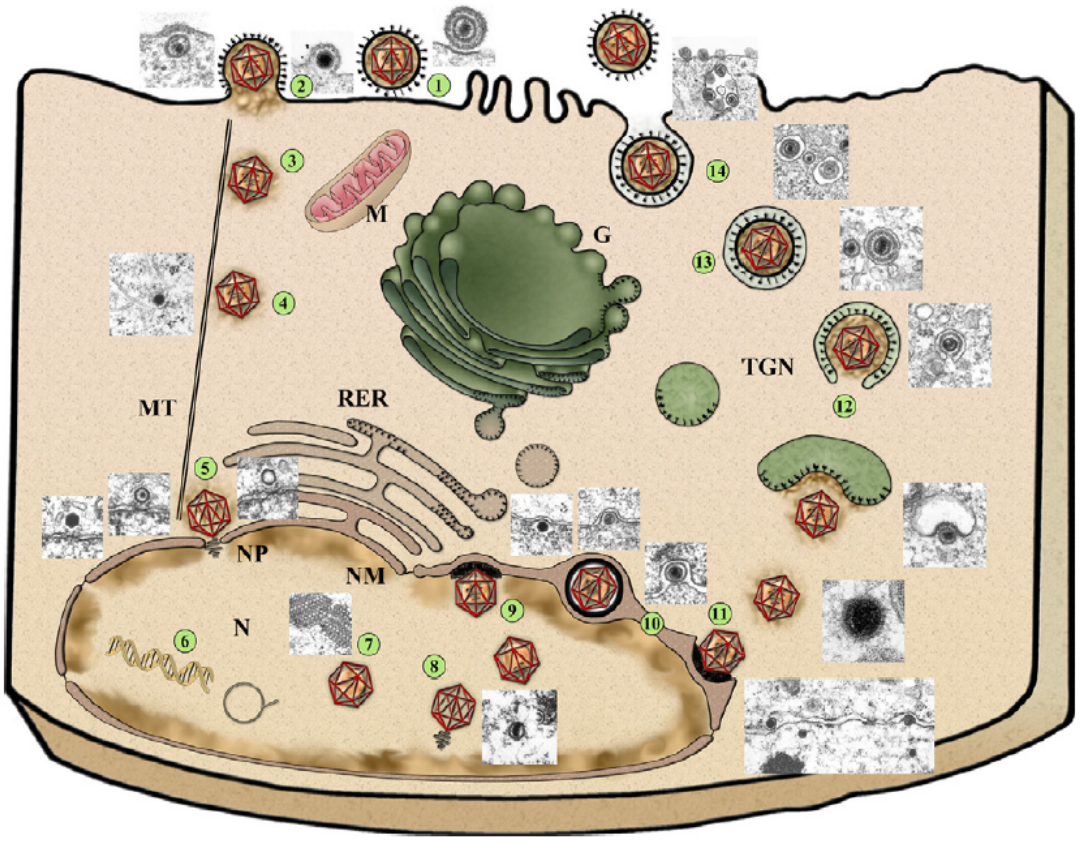

FIGURE 1.10: Replication cycle of the alphaherpesvirus pseudorabies virus (PrV). A diagram of the replication cycle is shown together with electron micrographs of the respective stages. After attachment (1) and penetration (2), capsids are transported to the nucleus (N) (3) via interaction with microtubules (MT) (4), docking at the nuclear pore (NP) (5) where the viral genome is released into the nucleus. Here, transcription of viral genes and genome replication occur (6). Concatemeric replicated viral genomes are cleaved to unit-length during encapsidation (8) into preformed capsids (7), which then leave the nucleus by budding at the INM (9) followed by fusion of the envelope of these primary virions located in the perinuclear space (10) with the outer nuclear membrane (11). Final maturation then occurs in the cytoplasm by secondary envelopment of intracytosolic capsids via budding into vesicles of the trans-Golgi network TGN (12) containing viral glycoproteins (black spikes), resulting in an enveloped virion within a cellular vesicle. After transport to the cell surface (13), vesicle and plasma membranes fuse, releasing a mature, enveloped virion from the cell (14). RER, rough endoplasmic reticulum; M, mitochondrion; G, Golgi apparatus.[92]

1.6 Project aims

The aims of this work were:

1) The investigation of the uptake of the transducer element nanoshells into NIH/3T3 fibroblasts. To study the best conditions and the mechanism for the nanoparticle uptake. Furthermore, to determine the cellular response and to investigate possible cytotoxicity and proof of the application for intracellular SERS.

2) The development of SERS sensors based on the specific binding between the thrombin binding aptamer and human α thrombin with Nanoshells as substrate *in vitro*. To investigate the specificity and the sensitivity of the sensor and origin of signals.

3) The development of SERS sensors based on the specific binding between the α3(IV)NC1 peptide and cathepsin D with nanoshells as substrate *in vitro*. For this it was necessary to investigate the redox-dependent conformational changes of the peptide and the digestion with Cathepsin D.

4) To conduct proof-of-principle experiments with the developed SERS sensors for the intracellular application in living cells.

5) Investigation of the relationship between MCMV infection of NIH/3T3 fibroblast and lipid droplet changes by CARS imaging on fixed and living cells.

Chapter 2

Materials and Methods

2.1 List of Chemicals

Chemicals were, unless otherwise stated ordered from Sigma and used without further purification. Except in the case of human α-thrombin which was purified by gel-filtration over a Sephadex column. Nucleic acid aptamers were synthesised and RP-HPLC purified by Eurogentec Ltd. (Southampton, UK).

Table 2.1

Chemical	Shortform	Company	Purity
1-Mercapto-hexan-6-ol	MCH	Sigma	>98 %
Mercapto propionicacid	MPA	Sigma	>98 %
1-Mercapto-4-benzoicacid	MBA	Sigma	>98 %
1-Ethyl-3-[3-dimethylaminopropyl] carbodiimide Hydrochloride	EDC	Fisher Scientific	
Tri carboxy ethyl phosphine	TCEP	Sigma	>98 %
TrisHCl		Sigma	
Sodium chloride		Sigma	
Potassium chloride		Sigma	
Magnesium chloride		Sigma	
Cysteamine	CyA	Sigma	
Auroshell^{TM}	NS	Nanospectra	
Penicllin/streptomycin	P/S	Sigma	
Cathepsin D	CathD	Sigma	
human α thrombin	hαT	Sigma	
Trypsin-EDTA		Gibco	
Dulbecco's Modified Eagel's Medium	DMEM	Gibco	
bovine calf serum	CS	Sigma	
L-Gluthamine	L-Glu	Sigma	
Sodium Azid	NaN_3	Sigma	
Methyl-β-cyclodextrine	βCdex	Sigma	
Glucose		Sigma	
2-(4-(2-Hydroxyethyl)-1-piperazinyl)-ethansulfonicacid	Hepes	Sigma	
Dimethylsulfonoxid for tissue culture	DMSO	Sigma	
glutaraldehyde		Sigma	¿98 %
Amino-acids + DNA bases			
L-Leucine	Leu (L)	Sigma	>98 %
L-Proline	Pro (P)	Sigma	>98 %
L-Arginine	Arg (R)	Sigma	>98 %
L-Asparagine	Asn (N)	Sigma	>98 %
L-Serine	Ser (S)	Sigma	>98 %
L-Phenylalanine	Phe (F)	Sigma	>98 %
L-Alanine	Ala (A)	Sigma	>98 %
L-Lysine	Lys (N)	Sigma	>98 %
L-Aspartic acid	Asp(D)	Sigma	>98 %
L-Cystein	Cys (C)	Sigma	>98 %
Guanosintriphosphate	GTP	Qiagen	for PCR
Thymidintriphoshpate	TTP	Qiagen	for PCR

Table 2.3

Name	DNA Sequence	Modification	Target	B
TBA	TTT TTT GGT TGG TGT GGT TGG	5'-HS-$(CH_2)_6$	α thrombin	21
csTBA	TTT TTT TTG GTT GTG TTG GTT	5'-HS-$(CH_2)_6$	nonspecific	21
IBA/GFA	TTT TTT GGT GGT GGG GGG GGT TGG TAG GGT GTC TTC	5'-HS-$(CH_2)_6$	insulin	36

Table 2.4

Name	Peptide Sequence	Modification	Spec. protease	AA
AS35	SPFLFCNVNDVCNFASRND	n/a	cathepsine D	19

2.2 List of Instruments

Table 2.5

Instrument	Supplier	Modifications
InVia Raman-AFM	Renishaw	480 nm, 512.5 nm, 633 nm, 780 nm
Nanoscope-AFM	Texas Instruments	
Centrifuge 5415D	Eppendorf	
Centrifuge 5810R	Eppendorf	
Biomate TC hood		
Incubator		
UV-Vis Biomate	Thermospectronic	Peltier thermocontroller
Mira 900	Coherent	titanium-sapphire laser
Synchro-Lock	Coherent	phase modulator lock
photomultiplier tube R3896	Hamamatsu	
Spectrophotometer ND1000	Nanodrop	
Fluoromax	Horiba Jobin Yvon	MicroMax plate reader
Polarstar	Optima	plate stacker
CM120 Biotwin	Phillips	digital camera
Ultrasonification Bath	UW	

2.3 Nanoshell as surface enhanced Raman sensing platform

2.3.1 Characterization of nanoshells

Extinction measurements can be used as a means of quality control for different batches of NS as well as for clarifying possible effects of different buffers and temperatures on the particle absorbance and therefore their aggregation behavior and SPR. Measurements were conducted with a UV-Vis spectrophotometer in a 80 μL quartz-cuvette in scanning mode between 400 and 1000 nm wavelength. Suspension with 10x 10^9 NS/ml in ddH_2O were measured for characterization and verification of supplier specifications. Investigations of the SPR temperature dependence of NS were done by connecting the cuvette holder to a peltier element and adjusting the temperature between 25 °C and 95 °C in 20 °C steps and waiting for 5 min for temperature equilibration before measurements. Data was processed in Origin. Size determination was conducted by scanning electron microscopy (SEM) measurements and taking averages of the diameters of 20 measured NS.

Table 2.6: Characterization values of Auroshell NS after delivery

NS-batch	Abs. max [nm]	Size [nm]	Abs. max [nm] datasheet	Size [nm] datasheet
May07	782	152±6	781	150
Jan08	784	152±6	782	150
Oct09	780	147±4	780	150

2.3.2 Aggregation of NS on APTES modified glassslides

NS solubilized in ddH_2O with a concentration of 40 x 10^9 particles/mL were vortexed and ultrasonified for 5 min before being placed in 3 μL spots on aminopropyl triethoxy silanized (APTES) slides and left until dry. Slides were ordered from Corning (GAP2 slides, USA, batchnumbers 12xxxx-14xxxx) or SCHOTT (Nexterion slides, GER). Excess particles, not physisorbed on the surface were washed off with copious amounts of ddH_2O. Particles formed layered aggregates, which were

investigated by atomic force microscopy, AFM. AFM measurements were done with the Nanoscope AFM (Digital Instruments, Texas) in tapping mode.

2.3.3 Modification of NS with small organic molecules

This section describes the different methods for preparing either monolayers of small molecules for sensing preparation or as anchors for further modification and steps. The following surface chemistry is solely based on the quasi-covalent gold-sulfur bond of thiol containing molecules.[93]

2.3.3.1 Mercapto benzoic acid (MBA) functionalisation for SERS pH sensor

For NS modification with MBA, a 10 % ethanolic solution with 10 mM of MBA in ddH_2O was prepared. This was then placed in a 10 μL spot on the surface aggregated spots, described above, and left at RT overnight. The next day the SAM was then washed vigorously with ddH_2O and the slides spun dry at 1000 rpm for 1 min in a table top Eppendorf centrifuge. For the functionalisation of sterile NS with 4-mercaptobenzoic acid 300 μL of a NS solution of 10 x 10^9 NS/mL was added to 10 μL MBA in (1 mM) and incubated overnight at RT. Excess MBA was washed off by careful recovery of NS out of the reaction solution by centrifugation. The sample was washed a further two times in double distilled H_2O.

2.3.3.2 Mercapto hexanol (MCH)/Mecaptopropionic acid (MPA)/ Cysteamine (CyA) functionalisation

Monolayers of the small organic molecules MPA and CyA have been used as covalent attachment anchors for the functionalisation with amino-acids and peptides via a 1-Ethyl-3-[3-dimethylaminopropyl]-carbodiimide hydrochloride (EDC) activated reaction. For this two different methods have been used. The first method consisted of the formation of a monolayer on the particles with 10 mM solutions of the above molecules in ddH_2O which were placed in 10 μL spots on the surface

immobilized NS aggregates and left for 2 h to react with the gold nanosurface. This was followed by vigorous washing with ddH_2O and dried by spinning in a tabletop Eppendorf centrifuge at 1000 rpm for 1 min.

Another method for surface functionalisation with amino-acid or peptides consisted of previous modification of the compound of interest with either MPA or CyA via an EDC activated reaction in solution before bringing in contact with the gold surface. This is described in the section "Modification with peptides and amino-acids" in detail.
Formation of mixed monolayers with MCH were used for blocking non-reacted areas to prevent the non-specific binding of amine/sulfide containing biological molecules which have affinity to the surface by either physio-sorption (NH) or covalent attachment (SH). Non-specific interactions lead to irregular orientation of the surface bound molecules and as a result lower SERS reproducibility. Therefore surfaces modified with monolayers of either small organic or biological molecules (DNA, AA, peptides) were incubated over 30 min with a solution of 1 mM MCH in ddH_2O at RT. The modified surface was then cleaned of any excess MCH by repeated washing as described above. In cases of NS in solution the same reaction was followed by 3 repeated spinning, recovery and washing cycles.

2.3.4 Modificaton with biomolecules

In this work different biomolecules were used for sensing applications. The two major groups applied here are peptides and DNA oligonucleotides (aptamers). In this context aptamers are highly specific DNA oligonucleotides with binding affinity for a protein of interest.

2.3.4.1 Modification with peptides and amino-acids

This section describes the two different methods applied for functionalisation of gold NS with amino-acid based molecules. In cases where peptides or amino-acides were used, EDC was applied for carboxy-functional crosslinking to thiol

function containing molecules. The site of reaction can be easily and also cost effectively controlled by using different kinds of thiol containing molecules (in our case CyA⇒C-terminal, MPA⇒N-terminal were used to modify the different ends). EDC reacts with a carboxyl to form an amine-reactive O-acylisourea intermediate. If this intermediate does not encounter an amine, it will hydrolyze and regenerate the carboxyl group. Figure 2.1.

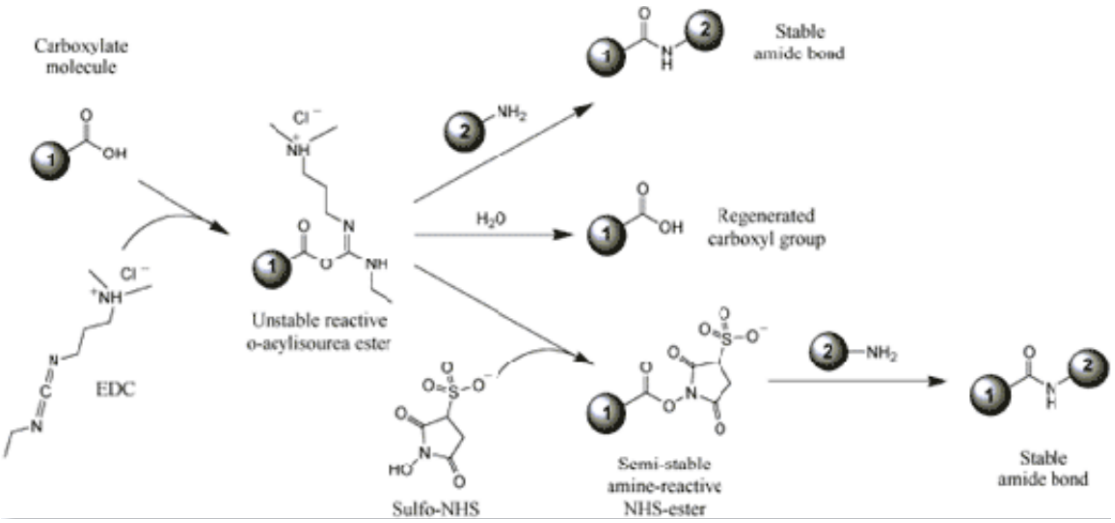

FIGURE 2.1: Different reaction paths of EDC with different substrates.[94]

As described above the first method to be used is based on pre-formed monolayers of MPA or CyA on gold nanoshells. For the modification of the MPA surface a preincubation step with EDC (50 mM) in ddH_2O for 20-30min was performed to activate the presented carboxylic groups. This was followed by reacting the N-terminal end of the peptide (250 mM) or amino-acids (400 mM) in ddH_2O overnight at RT. Obligatory washing as described above and further formation of mixed Monolayers using MCH (1 mM) over 30 min, plus washing were also performed. A similar approach was also used with CyA, although C-terminal end of peptides or amino-acids at same concentrations were first activated with EDC before reacting with the surface presented amino group of CyA.

In the second method used the peptides were first modified with CyA in situ and then conjugated to the surface. Table 2.7 describes the reaction conditions for peptide and amino-acids. Increased amounts of CyA are pushing the reaction equilibrium towards the formation of the thiol modified peptide and AA respectively

and hinder the homodimer formation. The different ratios take the molecular size of both molecule species into account. This means that a smaller molecule can be protected from other molecules of the same kind with a lower CyA ratio. Also, CyA has been observed to dissolve NS at higher concentration. Therefore only concentrations of CyA in water up to 250 mM have been used. In case of the thiol modified peptide, excess CyA was removed by two times purifying with a G-25 MicroSpin^{TM} size exclusion columns purchased from Amersham Biosciences (Buckinghamshire, UK).

Table 2.7: Reactionconditions for peptide and AA thiol modification

1:25 peptide:CyA ratio			1:5 AA:CyA ratio		
Compound	Concentration	Equvi.	Compound	Concentration	Equi.
AS35	10 mM	1	AA	40 mM	1
EDC	11 mM	1.1	EDC	44 mM	1.1
Cysteamine	250 mM	25	Cysteamine	220 mM	5
1x BB1	120 mM NaCl		1x BB1	120 mM NaCl	
	10 mM $MgCl_2$			10 mM MgCl	
	10 mM KCl			10 mM KCl	
	pH 7			pH 7	

2.3.4.2 Modification with 5' thiol modified aptamers and oligonucleotides

Possibly disulfide bound nucleotides (100 μM, 5 μL) were diluted to 100 μL in water and treated with *tris*(2-carboxyethyl)phosphine (TCEP) (1 mg) for 30 min at RT, gently agitated and purified using a G-25 MicroSpin^{TM} size exclusion column purchased from Amersham Biosciences (Buckinghamshire, UK). The aptamer was then diluted to a concentration of 10 μM in binding-buffer (BB) (Tris-HCl 50 mM, NaCl 140mM, $MgCl_2$ 10 mM, KCl 10 mM, pH 7.4), heated to 95°C for 5 min, cooled down to 72°C for 15 min for G-G hybridisation and afterwards cooled down to RT over 30 min. NS aggregate spots on the APTES glass slides were incubated with 15 μL of TBA solution in BB1 (10 μM) placed on the surface. This was left for reaction with the surface for 18 h at 30 °C and 400 rpm shaking in a Thermomixer (Fischer Scientific UK, Leicestershire), excess oligos were removed afterwards by rinsing the slide with copious amounts of binding buffer. To prevent non-specific interactions, the spots were incubated with a solution of mercapto-hexanol (MCH) (1mM, 15 μL) in binding buffer for 30 min and rinsed afterwards again with BB1.

Table 2.8: Composition of growth, infection and freeze media for TC

Reagent	Volume	[End]
Growth Media		
DMEM	500 mL	
CS	50 mL	10 %
P/S	6 mL	10'000 units.mL
L-GLu	6 mL	200 mM
Infection media		
DMEM	500 mL	
CS	15 mL	3 %
P/S	6 mL	10'000 units.mL
L-GLu	6 mL	200 mM
Freeze media		
DMEM	25 mL	50 %
CS	20 mL	40 %
DMSO	5 mL	10 %

2.3.5 Tissue culture techniques

2.3.5.1 Generall TC techniques

For handling cells for passage the culture medium was removed and the cells rinsed twice with pre-warmed sterile PBS. 2-5 mL Trypsin/EDTA (0.5 %)(depending on flask size) was added to the flask and the flask gently rocked for 1 min, or until all the cells have detached from the base of the flask. 5 mL of fresh culture medium was added to the cells in order to inactivate trypsin and transferred to a 15 mL Falcon tube. The cells were separated from the medium by spinning in an Eppendorf centrifuge at 1000 rpm for 5 min. The supernatant was poured of and the cells resuspended in 1 mL fresh media. One aliquot of the cells was added to a fresh flask (the volume added depends on the seeding density required), along with the required amount of culture medium to cover the flask surface and then returned to the incubator.

For freezing cells for long term storage, 1 mL aliquots of the re-suspended cells were put into 1.8 mL labeled cryovials, transferred to a Nalgene Cryo 1 °C freezing container and placed overnight at -80 °C. The following day aliquots were transferred into long term storage in liquid N_2.

For thawing cells from liquid nitrogen storage, cryovials were removed from the

liquid N_2 and the cells thawed slowly in a warm water bath (37 °C). The outside of the cryovial was disinfected with 70 % ethanol, and the contents of the cryovial transferred to a clean 15 mL plastic centrifuge tube along with 10 mL of fresh culture medium. The cells were centrifuge at 1,000 rpm for 5 minutes and the supernatant discarded. The pellet was then resuspended in 10 mL of fresh culture medium and transferred to a new 25 cm^2 flask. The cells were incubated at the appropriate temperature in 5 % CO_2 and the following morning the culture medium was changed to remove any remaining traces of dimethylsulfonoxid (DMSO).

To count cells they had to be stained with Trypan Blue stain 0.4 %. First making a 10 : 1 dilution of dye : cell-solution in a 96 well plate, taking 90 μl Trypan Blue stain and 10 μl of cell suspension. Cells were mixed by thorough pipetting up and down and the stained cells were then applied to a BrightLight Hemacytometer by carefully adding 10 μl under the sample plate and onto the grid. The cells inside the square and on the border of the center square on the hemacytometer were taken into account. Once for the upper sample and once for the lower sample, the numbers averaged and the cell amount calculated by following equation (2.1):

$$C_N = N(cell)_{avg} * 10^4 * dil_f \tag{2.1}$$

C_n	calculated cell amount in 1 mL
$N(cell)_{avg}$	avg of 2 to 4 cell counts with the hemacytometer
dil_f	Trypan-Blue stain/ cell dilution factor

2.3.5.2 Viral plaque assays

Twenty four hours before staring the procedure 1 - 1.5 x 10^5 NIH/3T3s were seeded into each well of a 24 well plate. The plate was gently agitated both vertically and horizontally every 30 min, for 1 hour to evenly distribute the cells.For preparing viral dilutions one 15 mL sterile plastic centrifuge tube was prepared containing 12 mL DMEM + 3 % CS per 24 well plate and pre-warmed to 37 °C in a water bath. A Sterile 96 well plate was used to prepare the dilutions of the viral culture. Each well in a single row of a 96 well plate contained 270 μl DMEM + 3 % CS per viral culture (6 wells). In order to titrate the viral culture dilutions 10^{-1} to 10^{-6} were prepared across the 6 wells. The medium off the prepared NIH/3T3 cell

culture in a 24 well plate was poured off into a bowl containing 1 % Virkon, then 250 μl of the viral culture dilutions were transferred into the respective wells (x 6). Incubation of the plate in an incubator at 37 °C for 30 min followed, gently agitating the plates every 10 min. The virus containing media was poured into a bowl containing 1 % Virkon and the cells washed twice with 1 mL sterile PBS (37 °C), leaving the second PBS wash on the cells. Meanwhile agarose solution was melted and 2 mL quickly transferred into one of the 15 mL plastic centrifuge tubes containing the 12 mL DMEM + 3 % CS and inverted to mix. PBS wash was taken off and carefully 1 mL of the media agarose mixture added to each well. Once the plate was completed it was placed in the incubator and the assay was allowed to incubate for 4-5 days.

For counting the plaques after 4-5 days of incubation, the plate was inverted and gridlines drawn with a fine microtip permanent marker pen. The number of visible plaques per well was counted using the gridlines as a guide. The number of plaques per well were multiplied by a factor of 4 in order to obtain a count per mL of viral culture (250 μL of viral culture added per well) and each count was multiplied by the respective dilution factor for that well, i.e. 1 x 10^{-1}, 1 x 10^{-6}. In order to obtain a final viral titre in plaque forming units/mL (PFU/mL), and the average count for all of the wells determined.

2.3.5.3 NS uptake amount in fibroblast and their location

For investigations of cellular uptake mechanism, cells were grown at standard conditions on resin beads. Beads (5g) were incubated overnight in PBS and autoclaved for sterilization. The beads were transferred into a T175 flask and an appropriate amount of cells added. After incubation and regular agitation over 2-4 days the beads were sufficiently covered with cells. The cells on resin beads were separated in five T25 flasks and incubated with 10, 150, 300 fM of NS over 3 h before removal of media, PBS washing and fixation in glutaraldehyde for 1 h. For TEM measurements, the samples were dehydrated in acetone and stained with osmium tetroxide. Processed cells on resin beads were transferred into resin for sectioning. Sections of 120 nm thickness were taken and put on a TEM grid for measurement. Each section contained between 50 and 100 cells. Acquisitions were made with a

CM120 Biotwin (Philips) transmission electron microscope connected to a digital camera. Sections were analysed by counting cells with internalized NS and estimating the maximum amount of NS per cell. For this the ell size was estimted t be $\sim 10\mu$m therefore $\sim$ 100 cell sections would account for 1 cell. Multiple TEM sections were investigated.

2.3.5.4 Investigations of nanoparticle uptake mechanism

For investigations of cellular uptake mechanism, cells were grown at standard conditions on resin beads and then pre-incubated for 1h with PBS buffer containing NaN_3 (10 mM) and glucose (50 mM) for ATP depletion. A second buffer with methyl-β-cyclodextrin (10 mM) and a potassium free buffer made up of HEPES (50 mM), NaCl (100 mM) and $MgCl_2$ (1vmM) were used for cholesterol and potassium depletion respectively. Buffers were sterile filtered and cells were incubated in separate flasks for 1 h. Subsequently the cells were washed with PBS and incubated with NS in media at a concentration of 10 fM. After 5 h of incubation the media was taken of, the cells washed% with PBS and fixed in 1 % Glutaraldehyde in PBS. For TEM measurements, the samples were dehydrated in acetone and stained with osmium tetroxide. Processed cells on resin beads were transferred into resin for sectioning. Sections of 120 nm thickness were taken and put on a TEM grid for measurement. Each section contained between 50 and 100 cells. Acquistions were made with a CM120 Biotwin (Philips) transmission electron microscope connected to a digital camera.

2.3.5.5 Investigation of NS uptake and cytotoxicity in NIH/3T3 fibroblasts

In the following fluorescence assays the signal was normalized to the background signal of cells grown over the same length of time covered in growth media. Errors were estimated by taking the standard deviation of 5 replicates. Assays were conducted following provided protocol. For the cell viability test the CellTiter-Blue (CTB) assay (Promega, UK) was used in a 96 well format. Cells were incubated with above stated growth media supplemented with NS (auto-claved after delivery

to ensure sterility) at concentrations from 0 - 300 fM (approximately 0 - 1800 NS/-cell). The CTB assay was conducted after 3, 6, 24, 48, 72 and 96 hours according to protocol. Apo-ONE Homogeneous Caspase-3/7 Assay and CytoTox-ONE Homogeneous Membrane Integrity Assay (Promega, UK) were used to detect possible apoptosis and necrosis signals after incubation for 3, 6, 9, 12, 24 h and 6, 24 h , respectively, with 10 and 300 fM NS in standard growth media. Positive controls for apoptosis were incubated for 3h with 1 μM of Staurosporine in growth media and for the necrosis assay the cells were lysed with provided buffer. Fluorescence Measurements on assays were run in NUNC 96 well plates, measured with a POLARstar OPTIMA (BMG Labtech GmbH, GER) microplate reader and signals were normalized to the intensity of untreated cells. The appropriate filter and light source setups recommended in the protocols were used.

2.3.6 Intracellular surface-enhanced Raman spectroscopy

SERS measurements were done with cells grown on quartz coverslips (0.2 mm, UQG Ltd., England) and incubated with media containing 300 fM of either bare or functionalized NS incubated in serum free media for 5 h. Spectra were acquired by manual search for characteristic particle scattering in adherent cells on quartz coverslips. Once particles were found a laser power of 3.5 mW was used to acquire 25 spectra each with 5 sec acquisition time. Spectra were then averaged. For further description, please refer to intracellular Raman studies (2.4.1.4).

2.4 Raman systems and spectra acquisition

2.4.1 Optical tweezing and single cell Raman spectroscopy with 783.2 nm He-Ne laser

2.4.1.1 Raman Microscope setup

An inverted Raman system built around a self constructed microscope was used to evaluate the cellular samples. Briefly, a temperature-stabilized diode laser operating at 783.2 nm (a circularized laser Diode, Sanyo DL-7140-201s up to 80 mW power) is expanded and introduced via a holographic notch filter (HNF, Tydex notch-4) into an inverted microscope and passed to the sample via a 50x NA 0.9 oil immersion objective. The backscattered Raman light was collected by the same objective and passed through the HNF. The Raman signal was then reflected by the dichroic mirror and imaged onto a 200-lm confocal aperture. Finally the beam was imaged onto the spectrograph (Triax 550 Jobin Yvon). This spectrograph employed a 300 lines/mm grating and was equipped with a CCD camera (Symphony OE STE Jobin Yvon) for detection of the Raman spectrum. The transmitted signal was imaged onto the CCD by making use of a lens placed at a distance equal to its focal length (f = 80 mm) from the slit of the spectrograph.

2.4.1.2 Live cell spectra acquisition

At first Raman spectra of detached healthy 3T3 cells were taken. Trypsinized cells were placed between quartz cover slip and slide (10 μL) separated by a 10 μL holding spacer. For bulk Raman studies on detached single cells laser power was 50 mW and acquisition time was 180 seconds. During the measurements the temperature of the stage was kept at 37 °C Spectra of 50 cells were averaged and water background corrected. To provide statistical data spectra of 50 different cells were taken and averaged. For every cell spectrum a spectra next to the cell was taken as background/ blind probe and then subtracted from each spectrum. This was done to correct for the substrate auto-fluorescence signal.

2.4.1.3 MCMV infected NIH/3T3s for single cell Raman

For the investigation of infected single cells a T25 flask was prepared for infection with 50 % confluent cells and left overnight. Cells were then infected with an MOI of 1 in infection media (3 % CS) and left for 48 h. The infected cells were then recovered from the flask by the standard trypsination and the resuspended cells then applied at high concentration to a quartz cover slip with spacer (10 μL) for spectroscopy. Laser power used during the measurements for bulk Raman studies on detached single cells was 50 mW and 180 seconds acquisition time. During the measurements the temperature of the stage was kept at 37 °C Spectra of 50 cells were averaged and waterbackground corrected. To provide statistical data spectra of 50 different cells were taken and averaged. For every cell spectrum a spectra next to the cell was taken as background/ blind probe and then subtracted from each spectrum. This was done to correct for the substrate auto-fluorescence signal.

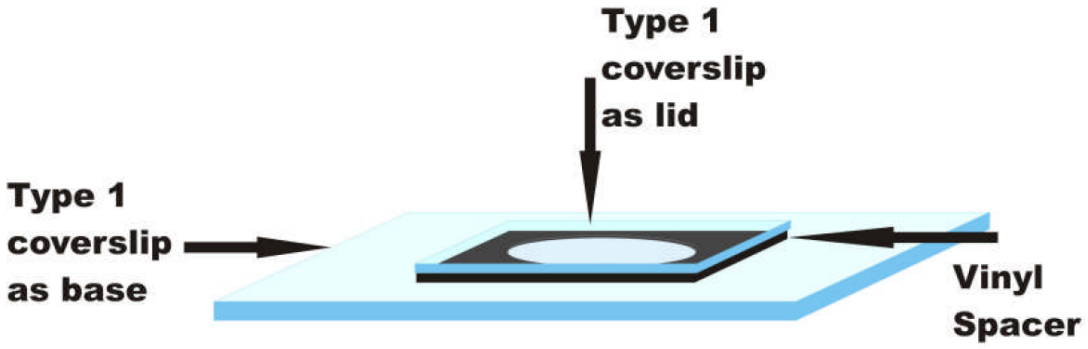

FIGURE 2.2: Coverslip-spacer arrangement with a volume of 10 μL for live cell native Raman spectroscopy

2.4.1.4 NS enhanced intracellular Raman spectroscopy

Bare and MBA functionalized NS inside cells were detected by searching for bright scattering events whilst moving the laser beam through cells and NS based SERS measurements were obtained with 3.5 mW laser power at the sample and 5 sec acquisition time. 10 acquisitions were averaged for the presented spectra.

$$P_{ij} = \frac{\sum_{k=1}^{W}(I_i(k) - \overline{I_i})(I_j(k) - \overline{I_j})}{\sigma_i \sigma_j} \tag{2.2}$$

P_{ij}	correlation coefficients
I	spectral intensity
ij	non identical spectra
k	wavenumber index
σ_i	standard deviation of the ith spectrum
σ_j	standard deviation of the jth spectrum

2.4.2 Commercial Renishaw Invia system with 785 nm diode laser

2.4.2.1 Raman Microscope setup

For this work the InVia Confocal Raman Micrscope AFM system (Renishaw, UK) was used with a 785 nm diode laser with up to 7 mW of laserpower in a Class 1 laser safety environment. The provided software Wire 2.0 (Renishaw, UK) allows easy control of automated stage, acquistions and mapping experiments. For biosensing experiments a 50x Leica water immersion objective with an NA of 0.8 was used.

Correlation coefficients between all nonidentical spectral pairs (i * j) in the same data set were determined from the data where i, j is the index of the spectra in the data matrix, k is the wavenumber index of the individual spectra, I is the spectral intensity, W is the spectral range, and σ_i is the standard deviation of the i^{th} spectrum 2.2. Once the correlation coefficients P_{ij} are calculated, Γ, the average of the off-diagonal correlation coefficients, can then be determined with equation 2.3 Γ thus defined is an easily determined and very useful parameter for quantitative assessment of spectral reproducibility. Γ varies between 0 and 1, where 1 is the case of identical spectra and 0 the case of completely uncorrelated spectra. This was used to evaluate the reproducibility of multiple measurements.

$$\Gamma = \frac{2\sum_{i=1}^{N}\sum_{j=1}^{N} P_{ij}}{N(N-1)} \tag{2.3}$$

Γ	off diagonal cross correlation coefficient
i,j	non identical spectra
P_{ij}	correlation coefficients
N	wavenumber index

2.4.2.2 Peptide and DNA based SERS for protein detection on NS aggregates

Oligonucleotide approach:
SERS on NS bound oligonucleotides was performed on APTES glass slide immobilized particle aggregates functionalized with the aptamer/DNA strand of interest. Experiments were usually led with the following conditions for the acquisitions. The laserpower was adjusted by using a pinhole and filters to 1 percent of the maximum power at the sample, which has been measured to result in 30±5 μW. For biosensing experiments the acquisition time per aggregate was 10 sec in scanning mode in the range of the fingerprint region of biomolecules between 800-1800 cm^{-1} with 25 consecutive measurements which were averaged to obtain the final Raman scattering spectrum. During the experiments the objective was immersed into the solutions

Protein sensing experiments on TBA modified NS were done by incubation with non-specific and specific compounds in binding buffer (as described above). Between measurements the compounds were removed completely by vigorous washing. For every measurement a new spot on the modified NS aggregates was used. Cycles of target or control protein incubations always consisted of a washing step with PBS, BB and protein solution incubation in BB with a contact time of 30 min before measurements. Measurements were done as described above. Successive washing steps with urea 8 M, for protein denaturation, and G-quadruplex disrupting buffer (GDB) ($CaCl_2$ 200 mM, EDTA 10 mM, Tris-HCl at pH 8.0) and salt removal with ddH_2O and a final washing step with BB, were performed in order to recover the original spectrum.

The study of the melting behavior of the GFA (stacked G-quadruplex forming aptamer) was done with a home built heatable stage connected to a water bath in which the APTES glass slide with the functionalized NS aggregates (NS-GFA) was embedded. The temperature was adjusted between 30 °C and 70 °C in 10 °C and manually cooled down to RT temperature. One spot was used during this experiment and the conditions for spectral acquisition were the same as for previous experiment.

Peptide/AA approach:
The second approach for direct protein detection was to detect Cathepsin D which binds specifically to the AS35 peptide. SERS experiments have been done on the same kind of immobilized aggregates as used for the aptamer based detection method. Initial experiments were done to find the best way to achieve reproducible and strongly enhanced signal. For the initial Raman measurement the sensing surface under the objective was immersed in PBS 50 μL. The acquisitions itself was prefaced by a step with ∼150-200 μW and up to ten 10 sec acquisitions until the spectra showed nice strong signal, to excite the surface plasmons, before taking 25 measurement at the normally used 30±5 μW. Spectra were taken in the spectral range of 400-1800 cm^{-1} to include the C-S stretches around 500-700 cm^{-1} into the measurements. Sets of measurements were averaged and the Pearson cross correlation factor calculated as a means of quality estimate.

To investigate the redox-potential dependent behavior of the peptide spectra, the approach was based on using the GSH/GSSG redox couple at different ratios to produce between -100mV and -300 mV, for 10 min. This was then followed by digestion with the mentioned Cathepsin D also presented with the appropriate GSH/GSSG ratio and incubated for 1 h before measurements. Measurements were conducted as described in section 2.4.2.2.

2.5 Coherent anti-Stokes Raman live cell imaging with synchro-locked 592.8 nm laser

2.5.1 CARS system description

A home-built laser-scanning inverted microscope is used to record images. A diagram of the setup is shown in Figure 2.3. The pump and Stokes frequencies, p and s, are provided by a pair of titanium-sapphire lasers (Mira 900, Coherent). The frequency difference $p - s$ is tuned to match the CH_2 vibrational mode in lipids. The two beams were combined collinearly and focused into the sample with a water immersion microscope objective lens (plan apo 60x 1.20 NA, Nikon). The CARS signal, which had a frequency $as = 2p - s$, was detected with a photomultiplier tube (R3896, Hamamatsu) in the forward (F-CARS) or backward (E-CARS) directions [95]. A long wave pass dichroic mirror (683dcxr, Chroma), and two band pass filters (HQ590/45, Chroma) were used to separate the (blue-shifted) CARS signal from the excitation wavelengths. The beams were scanned in the sample plane with a pair of mirror galvanometers (Cambridge Technology). The two lasers, designated master (Stokes) and slave (pump), were synchronized with a phase-locked loop system (Synchro-Lock, Coherent). Both lasers were mode locked, emitting pulses with a full width half maximum (FWHM) duration of 2 ps and a repetition rate of around 80 MHz. The two repetition rates were precisely synchronized by actively adjusting the length of the slave laser cavity to match the free-running master [96]. A frequency error signal was generated by picking off a portion of each beam and was minimized through a phase-locked loop. Timing jitter in the synchronization causes visible noise in images. However this noise could be eliminated by switching over to a separate phase-locked loop on a higher harmonic of the error signal [49]. By using the ninth harmonic the timing jitter was maintained at less than 215 fs. Synchronisation was monitored with a photodiode. Half of the combined beam was focused into a GaAsP photodiode (G1116, Hamamatsu). The band gap of the semiconductor was greater than either the pump or Stokes photon energies; the laser wavelengths both lay outside of the spectral response range. However a photocurrent was generated through two-photon absorption in the material giving a signal proportional to the square of

the total beam intensity [97]. When the master and slave lasers are synchronized and in phase an additional signal due to sum-frequency generation is detected [98]. This signal was used to optimize the phase shift of the higher harmonic loop so that the pulse trains overlap precisely. Two-photon imaging was achieved on the same platform. The master laser was used for excitation and the backward signal was recorded with a GFP filter in place (Brightline 514/30, Semrock).

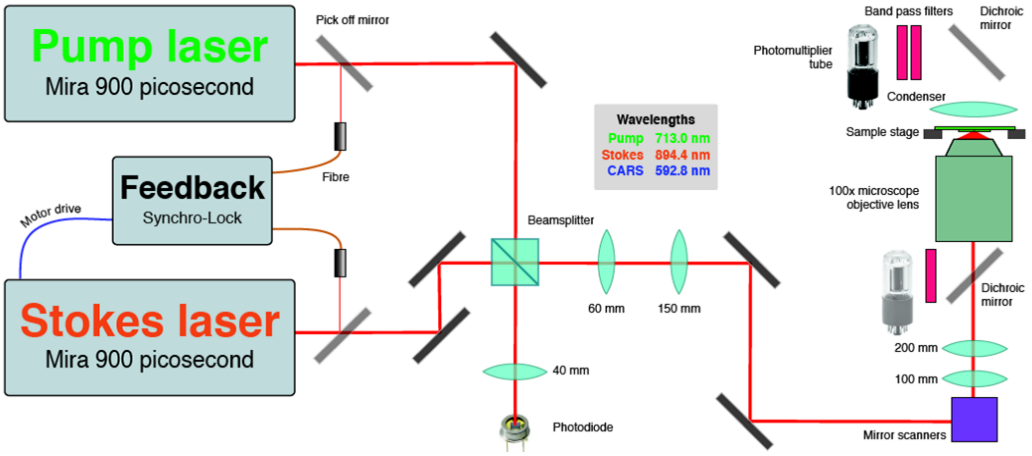

FIGURE 2.3: CARS system schematic showing the pump- and stokes laser synchronisation via SynchroLock

2.5.2 Live cell imaging

2.5.2.1 CARS imaging on MCMV infected NIH/3T3s

NIH/3T3 fibroblast cells with a passage number of 11-20 were grown in Dulbecco's modified Eagle's Medium (DMEM) complemented with L-gluthamine (200 mM), penicillin/streptomycin (10 000 units/ml) and 10% calf serum and incubated in standard growth conditions at 37 °C in a 5% CO_2 atmosphere. For imaging the cells were seeded on 50x22x0.12 mm glass coverslips at 50% confluence and left for 12 hours at standard growth conditions to settle. Cells were then fixed with 1% formaldehyde in phosphate buffered saline (PBS) for 15 minutes at room temperature, washed three times with PBS and stored dry at 4 °C. PBS was used to wet

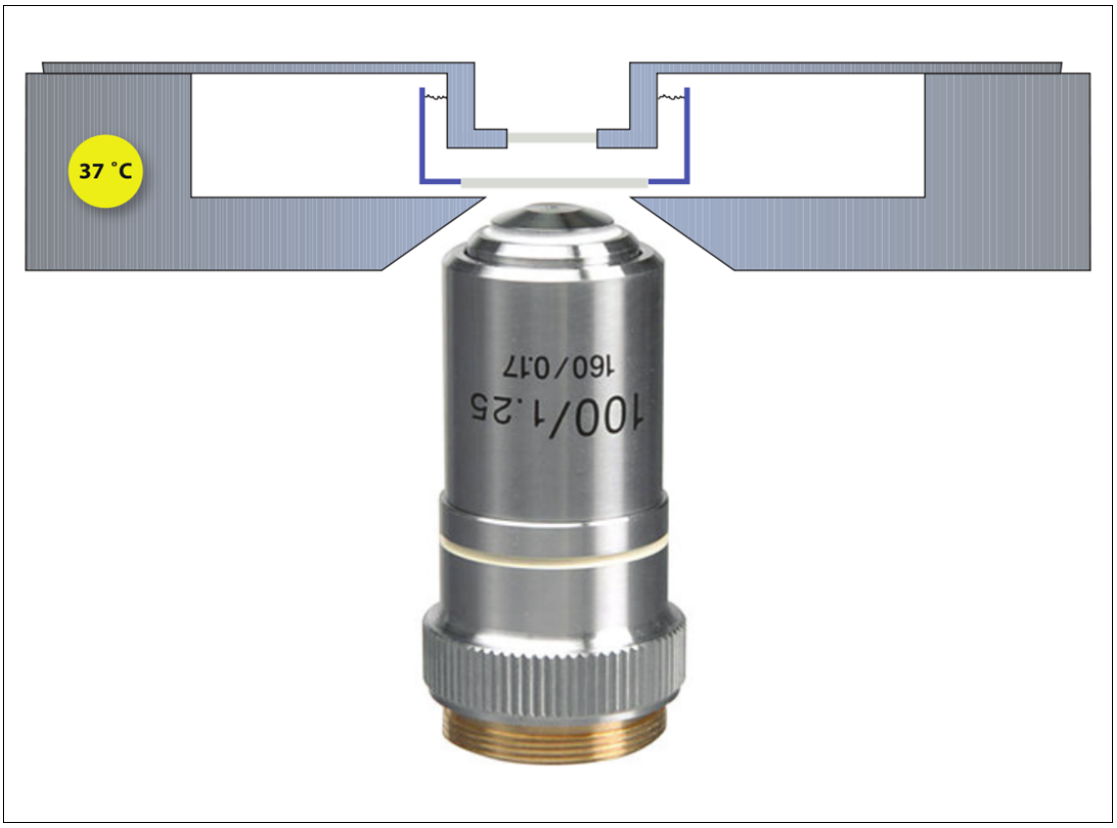

FIGURE 2.4: Setup of the heat controlled and sealed cell incubation chamber

the samples for imaging. Infection with mouse cytomegalovirus (MCMV) wild-type mutant C3X or a genetically-modified version of the Smith strain expressing the green fluorescent protein (GFP) [99, 100] were conducted at a multiplicity of infection (MOI) of 1, resulting in one viral particle per seeded cell, with media containing 3% calf serum to reduce cell growth. Seeding was followed by a synchronisation step keeping cells for 1 h at 4 °C before incubation for 48 h at 37 °C. Cells were then washed twice with PBS, fixed, and stored, in the dark for fluorescent samples, as described above.

Images were acquired in scanning mode, 1 sec per image and 5 images were averaged. Laser power at the sample ranged between 30-120 mW.

2.5.2.2 Live MCMV infected NIH/3T3 for CARS imaging

Live cell imaging was conducted in a specially designed, atmosphere sealed and [101] heat controlled incubation chamber. This gives the opportunity to investigate the process of infection on a single cell or a population of cells in same conditions. Figure 2.4 shows a sketch of this incubation chamber. CARS imaging with this setup allows signal detection in forwards and backward direction and therefore gives the opportunity for parallel imaging of Raman and TFP signal. To minimize diffraction losses the top window was designed to reach into the media. Cells were seeded for imaging in glass bottom petridishes at a confluence of 50 % in all cases. Live cell infections were done at an MOI of 1 and instantly installed on the CARS system for imaging from the start of infection up to 4 days of infection. Live cell images were also acquired in scanning mode and 5 images averaged.

Chapter 3

The investigation into uptake of NS into NIH/3T3 fibroblast and feasability as SERS sensors

3.1 Uptake of NS in vitro and investigation: pathway,cytotoxicity and cell response

3.1.1 Introduction

Nanoparticles have found various applications in biomedical research.[102–106] They are used, for example, in drug delivery,[104, 107] intracellular sensing[108, 109] and diagnosis and treatment of cancer.[108–113] In addition, the ubiquitous use of nanomaterials in everyday applications such as waterproofing formulations, sun creams, and detergents means that a thorough knowledge about their possible toxic effects is crucial.[114] For example studies on long carbon nanotubes show that the hazardous potential on inhalation is comparable to asbestos; [115, 116] a fibrous silicate material which was banned due to its toxicity over a decade ago. However shorter (100 nm), conjugated carbon nanotubes have been shown to have no serious cytotoxicity in mammalian cells.[117]

Since the ultimate goal of the work in this thesis is to perform surface-enhanced Raman spectroscopic (SERS) studies to understand cellular behavior, initially the effects of nano-particle exposure on our biological model system has been investigated. Most studies on intracellular SERS have focused on collecting spectra and have stopped short of a thorough examination of the cellular response to the nanomaterial.[118–120] Furthermore, very few publications have taken the next step and examined the actual mechanism of particle uptake,[105, 121–123] although the impact on the disturbance caused inside the cells and therefore the applicability of the method is dependent on where, and in which state, we find the particles after internalization.

In this chapter results are presented on the cellular uptake of Nanoshells (NS) and the influence on cells.[124, 125] These NS, core shell particles consisting of a silica core of around 120 nm in diameter encapsulated in a thin and stable layer of gold, exhibit absorbance which can be tuned to a necessary optical wavelength by the core-shell diameter ratio.[30] They also exhibit surface plasmon resonance (SPR) which can be excited by illumination with light of a suitable wavelength as described in the introduction.[78, 125–130] The SPR of NS enhances the inherently weak Raman signal of molecules in the near vicinity of the particle surface [60, 131] and enhances the Raman signal by a factor of 10^{12}.[77] Investigating the cell viability of murine 3T3/NIH fibroblasts in culture after NS incubation shows that the cells are viable, an observation which is supported by measuring markers of apoptosis and necrosis. Furthermore examinations of the fate of the NS inside the cells using transmission electron microscopy (TEM) was conducted,[132] allowing the location and study of the immediate surroundings of the particles. Finally this chapter shows the difference in Raman measurements taken of whole cells and the SER spectra with NS probing different locations in the cytosol and demonstrate the use of functionalized NS [77] for intracellular pH measurement.

3.1.2 Investigation of intracellular location and pathway

Before bringing in contact with cells, the particles were sterilized by autoclaving and the absorbance was checked and compared to non-sterilized NS. Autoclaving caused no changes to the absorbance of the NS solution as shown in Figure 3.1a, confirming that the particles are still intact and their plasmon resonance remains unaltered. The sterile particles with a concentration of 6.9 pM were diluted to a concentration of 10 fM in DMEM growth media supplemented with 10 % calf serum (standard growth conditions) directly before incubation with NIH/3T3 fibroblast cells for 5 h. Firstly, the uptake of NS in 3T3s in standard growth conditions were confirmed by TEM microscopy, as widely used in analytical tissue culture, [132, 133] (Fig. 3.1b) showing the inclusion of single NS into the cytosol in the vicinity of the nuclear membrane. [133] This proves that NS are taken up voluntarily inside the cells without the use of transfecting agents.

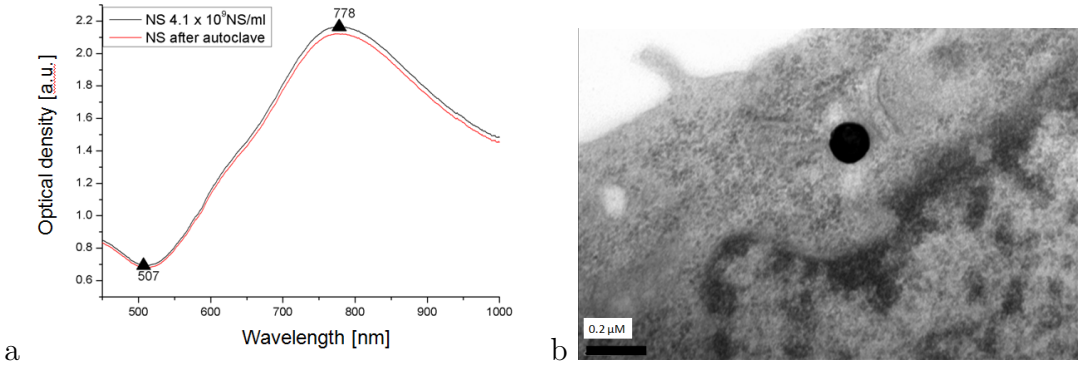

a b

FIGURE 3.1: a) Absorbance spectrum of NS with Absorbance maximum in the NIR at 778 nm. b) TEM images of NS inside NIH/3T3, image on the left showing a NS pair in the cytoplasm near the nuclear membrane (scalebar 0.2 μm).

Further, it was examined whether NS are taken up via an active/passive endocytotic uptake mechanism as has been reported by Rejman *et al.* [2008]. They found that 50 - 200 nm fluorescent latex beads were taken up by a clathrin-mediated process or by an unknown alternative mechanism. [134] Therefore we pre-incubated the cells with different buffers leading to the inhibition of different endocytotic pathways and incubated the cells with NS at a concentration of 10 fM in standard growth conditions with media containing 10% CS. The 3 pre-incubations cause cells to be either ATP, cholesterol or potassium depleted. Prior depletion of the

intracellular ATP levels leads to a stop of all ATP dependent cell mechanisms and thus also the inhibition of every active uptake mechanism like e.g. glucose, calcium transporters as well as vesicle invagination promoting proteins. The exposure to methyl-β-cyclodextrine chelates cholesterol presented in the outer membrane of the cells. Cholesterol increases the membrane rigidity and has an influence of lipid raft formation. In the rafts diffusion is slower and membrane proteins (for example receptors)accumulate; this is important for receptor mediated endocytosis. Less cholesterol thus means higher membrane fluidity and also lower contact time between receptors and extracellular molecules or particles. The third preincubation in a potassium free buffer leads to a decrease of potassium inside the cell via osmosis. K^+ is needed for the activity of clathrin, a protein that promotes the the formation of of "coated pits" which are dents in the membrane leading to invagination. Low potassium levels prevent clathrin mediated endocytosis pathways.[135, 136] The NS incubations were conducted for 5 h, (since we previously found this to be sufficient for introduction of small numbers of NS), before fixation and preparation for TEM sectioning and measurement. To obtain information about the differences of particle uptake 100 sectioned cells were checked and particles counted. The thickness of the cell sections was 120 nm and therefore it was estimated that around 100 cell sections would statistically account for one NIH/3T3 cell of an average diameter of around 10 μm 20 %. The NS amount per cell was then determined in accordance with these assumptions. We expected to find a decrease in particle uptake in one or more cases where fibroblast cells were deficient in compounds crucial for endocytotic uptake,[122] compared to the control experiment without separate treatment. The uptake of NS did not decrease at all (Fig. 3.2) and rather seems to be slightly increased for the cases where cells were depleted of ATP, cholesterol and potassium. These findings indicate that the established endocytosis mechanisms, active/receptor/clathrin mediated, are not solely responsible for NS internalization. Also, pinocytosis (also known as cell drinking) can be excluded, as was suggested before,[137] because this would be also a clathrin dependent process. Previous reports have implicated serum protein adsorption in nano particle uptake.[102] A further experiment where NS were incubated in serum free media over the same duration actually shows a large increase of NS uptake (Fig. 3.2), in the range of up to 3-fold. This observation rules out an endocytosis mechanism mediated by adsorption of serum proteins and

suggests that the absence of serum proteins makes NS uptake even more efficient. This may suggest a link between "malnourishment" and NS uptake.

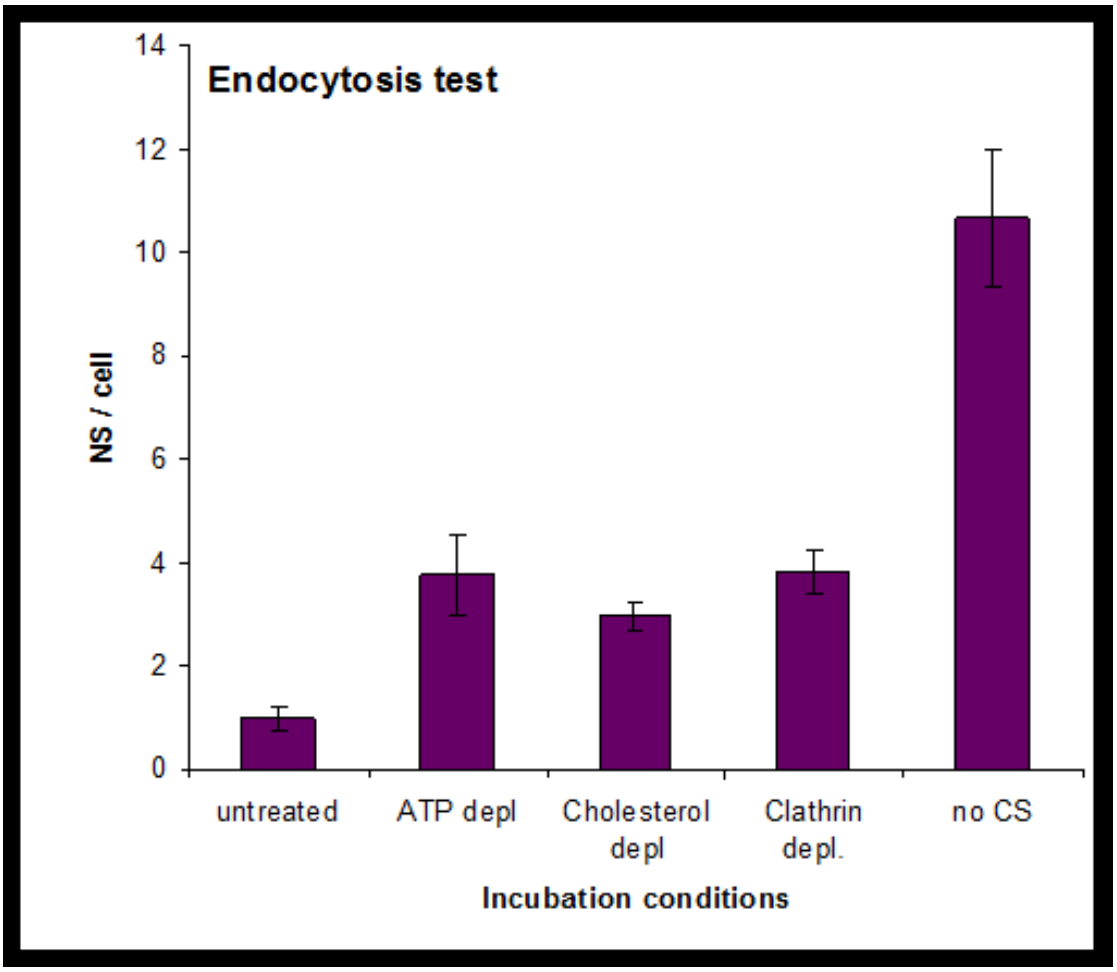

FIGURE 3.2: Estimated amount of NS per cell according to particles found in 100 TEM sections. NS incubations for this test were conducted for 5h with 10 fM NS in 10% CS containing media, except the condition with no CS on the right. The bars show the amount of NS (monomers, dimers) found in 100 cell sections. Errobars depict the systematic percentage error

In order to try and understand the NS uptake in more detail and finding an answer to the above raised questions, this work further exploits TEM to gain information about the uptake, fate and localization of NS inside the cells. A magnification up to 33000x allows the observation of the close surrounding of the particles inside the cells. Of 67 sections containing NS we analysed, NS were always localized in the cytosol and observed that while the particles can be found near the

nuclear membrane, they are never present in the nucleus. This localisation may suggest that NS are actively transported towards the nucleus, but was not further investigated in this work. In Figure 3.3 a,b and c particles are shown which were incorporated in the presence of serum in the media. On the other hand, Figure 3.3d is a representative image of a particle taken up in the absence of serum in the media. Figure 3.3a shows NS which were found free (not incorporated in a vesicle) in the cytosol - about 50 % of the particles taken up in conditions with serum in the media can be found free, non-coated, inside the cells. NS can be also found in vesicles, probably lysosomes (Figure 3.3b) or coated by a layer (Figure 3.3c), 5-10 nm thick and of high density, similar to surrounding cytosolic proteins.

It was suspected that this might be a layer of serum proteins adsorbed to the particle, but when we examined NS which were suspended solely in growth media with calf serum over a stretch 12 hours a similar coating could not be found in with TEM imaging (Figure)3.4. On the basis of this evidence, it appears that the coating forms during or after entry to the cell, perhaps as a reaction to the foreign particle. A possible response could be the formation of a lipid monolayer around the particle surface. Another imaginable mechanism is the recruitment of proteases towards the gold surface bound serum proteins not visible in TEM images. In the case where NS were taken up by cells in serum-free media, TEM images show non-coated NS without vesicles of the type seen in Figure 3.3d. This information is crucial for selecting the best condition for intracellular sensor development, where a free particle surface is desirable and biosensors are presented freely, to the intracellular environment. It appears that this passive mechanism allows the particles to merge with the membrane and pass through it without encapsulation. This explanation can be backed up by the findings of Roiter *et al.*, who reported that the curvature of lipid bilayers dropped onto smooth nanoparticles between 22 and 200 nm diameter does not promote membrane brakes.[138] As particles of sizes up to 100 nm are known to be taken up by active endocytosis[121, 139] a mechanism in which the particles merge with and pass through the membrane at areas of high membrane fluidity seems likely, as the cell membrane consists of domains of differen fluidity.[140] This would also explain the increased uptake in the cases of cholesterol depletion, since cholesterol increases membrane rigidity, and also the increased uptake in serum free media, where the particles display no

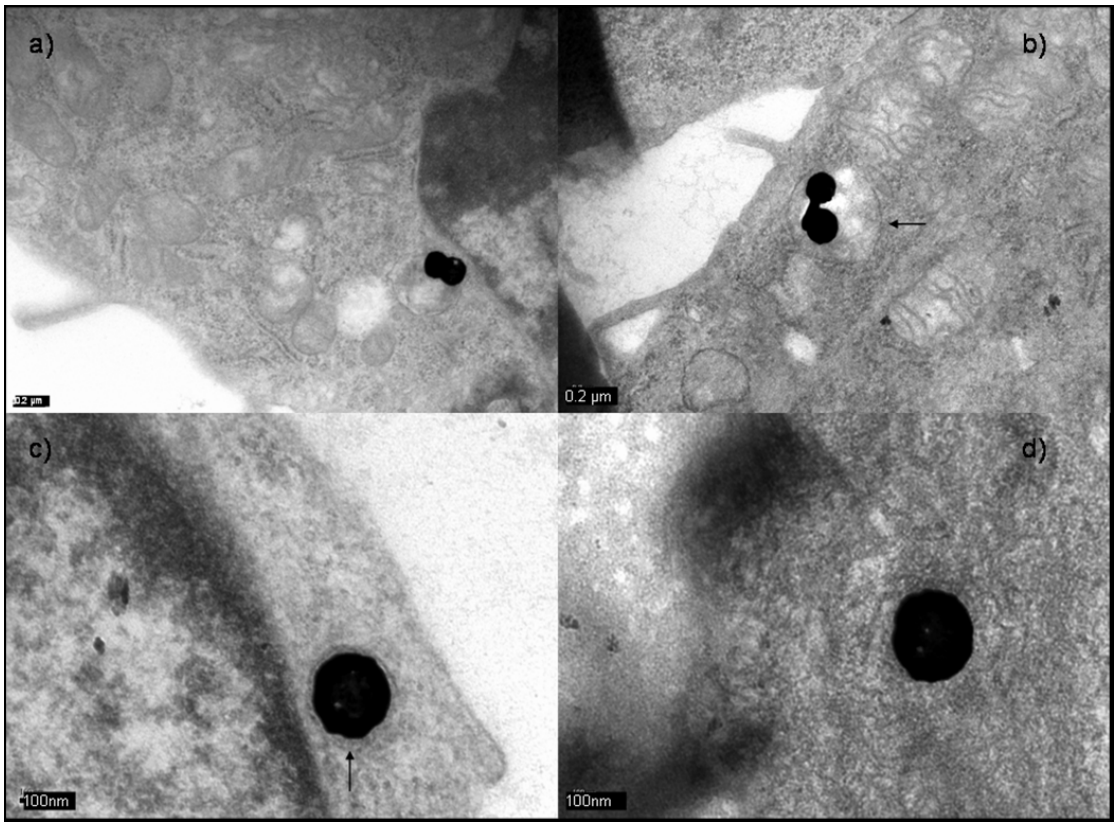

FIGURE 3.3: Set of TEM images of NS inside cells. Images a, b, c are all of NS which were incubated in media containing 10 % CS and can be found either a) free suspended in the cytosol (scalebar 0.2 μm),or b) taken up in oversized vesicles or as in c) surrounded by what might possibly be a dense coating of protein. d) shows a representative NS which has been taken up during incubation without any CS in the growth media. None of the NS found in these conditions were surrounded by any kind of coating or vesicles inside the cells.

adsorbed serum proteins and are therefore not led to protein receptors found in rigid lipid rafts.[135]

Furthermore the amount of particles taken up into cells at standard growth conditions (DMEM media + 10 % CS) was studied by direct TEM analysis as shown above. Figure 3.5 shows the uptake behavior of NS into cells in the concentration range observed in this work (10, 150, 300 fM). For these concentrations we see a linear behavior in the particle uptake, ranging from 3-30 particles. This linear uptake may not be universal over an increased NS concentration range since

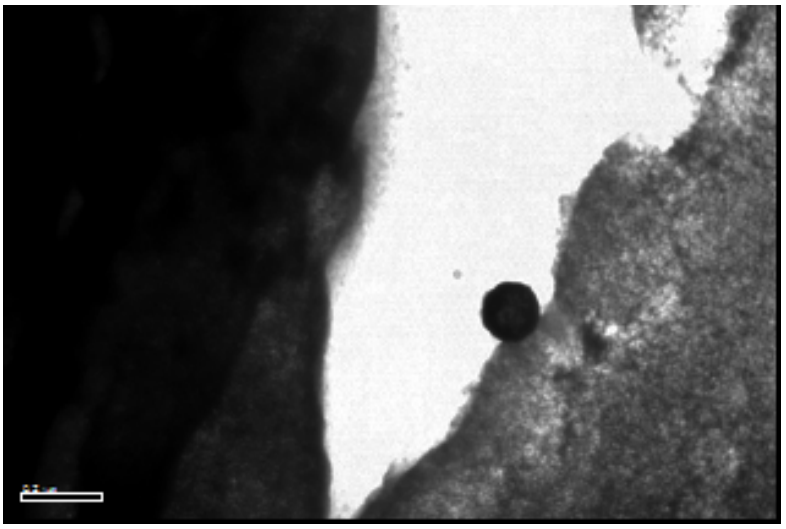

FIGURE 3.4: Exemplary TEM image of NS incubated in pure CS over 24h and then transferred to a TEM grid

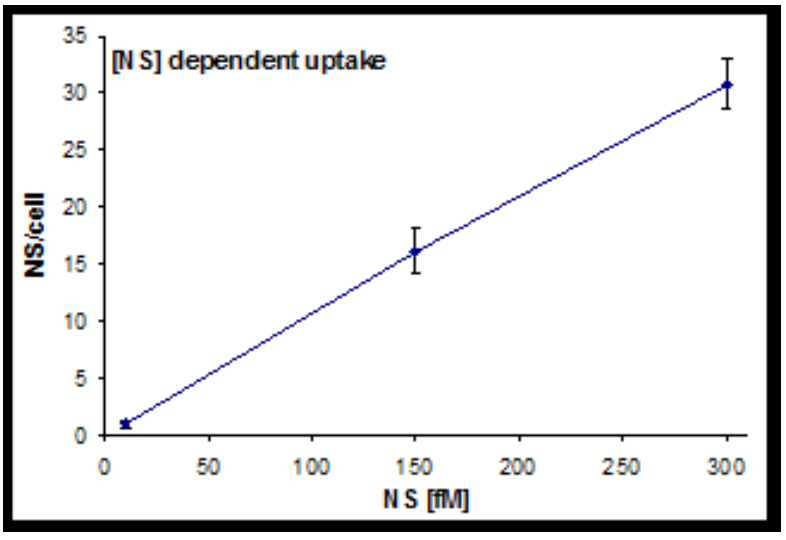

FIGURE 3.5: Graph shows the amount of NS taken up into NIH/3T3 fibroblasts at standard growth conditions with 10, 150, 300 fM of NS added to 10 % CS containing growth media.

increased particle numbers will probably lead to saturation. Also as described before, the actual incubation conditions are crucial for the coverage of the particles inside the cells as well as the number taken up.

3.1.3 Study of cellular response and cytotoxicity

After carrying out this essential work investigating if and how cells internalize NS we have to examine the long term effects during the cells growth cycle. To illuminate this, studies were conducted firstly observing the cell viability and secondly measuring markers for apoptosis and necrosis with appropriate assays.

To test the cell-viability a range of 11 NS dilutions between 0 and 300 fM of particles were prepared in growth media with serum. The NS were added to cells in 96 well plates seeded at 50 % confluence the previous day and washed with PBS prior to NS treatment. The CellTiter-Blue fluorescence assay was used according to protocol at different time points up to 96h after incubation. This time frame was chosen to be able to observe a whole growth cycle of a cell culture, from the slow initial phase over exponential growth towards the static phase after 48h. The results of the cell viability test in Figure 3.6 show that there is no difference between growth of NIH/3T3 cells at standard conditions without NS or incubated with different NS concentrations of up to 300 fM correlating to 1800 NS/cell. Figure 3.6 shows that fibroblast cells exhibit the same growth behavior, reaching the static phase after two to three days regardless of the presence of NS in the media or not. Even the errorbars, which depict a single standard deviation of 5 replicates of every individual measurement, are very similar and show very good consistency of the conducted experiment. Hence, we assumed that there are no detrimental effects on cell growth when cells are incubated with NS at the described conditions.

In order to further ensure that there are no detrimental effects of NS incubation we also assayed for molecular markers of cell death. Apoptosis is a control mechanism in cell growth which leads to cell death in situations such as stress induced by infection detrimental mutations or intrusion of foreign particles. Former reports on the uptake of all sorts of particles into the intracellular environment have normally

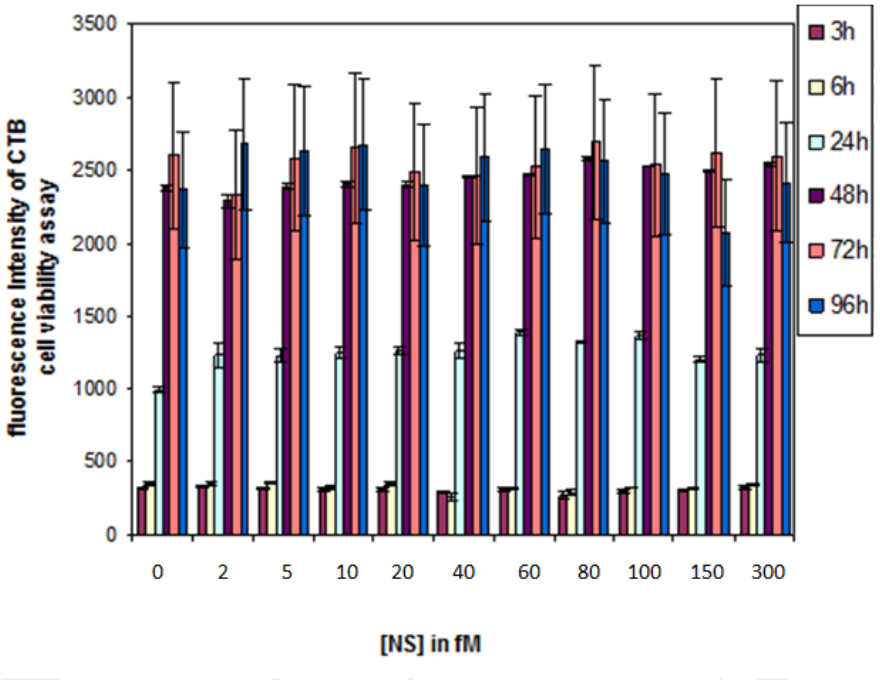

FIGURE 3.6: CellTiter-Blue Cell viability test showing fluorescence signal strengths of cells incubated with varying NS concentrations of 0-300 fM at different time points up to 96 h. The intensity is normalized to the control and proportional to the cell population per well. Error bars depict single standard deviations of 5 replicates.

stopped after microscopical investigation of cell cultures, determining morphological changes, or the lack of. By measuring markers of apoptosis and necrosis at the lowest and highest NS concentrations, as detailed above, possible lethal cell responses were investigated. For the apoptosis test an assay for caspases 3 and 7 was chosen as these proteases are among the first signals in the apoptosis cascade leading to imminent death of the cell. Figure 3.7 shows the results of this assay at 10 fM and 300 fM NS as well as the signal obtained in positive and negative controls. The tests were conducted at intervals of 3, 6, 9, 12 and 24 hours after the start of incubations and in addition a positive control was run incubating cells for 3 hours with Staurosporine (2 mM) which is known to be cytotoxic and leads to immediate apoptosis. It can be seen in the graph that all the incubations with NS did not indicate apoptosis at any time up to 24h compared to the negative control of untreated NIH/3T3 fibroblasts. Slight fluctuations are normal for these kind of assays, methodological errors, and stay in the error margin. We can therefore

assume that cells which have taken up NS do not show apoptosis on the measured timescale, which is the relevant period in which sensors should be applied.

In order to investigate the possibility of NS induced necrosis (potentially due to membrane disruption during particle entry), an assay was used to probe for free lactase in the extracellular environment which would appear as a result of the release of intracellular components. Further, this assay gives the possibility to check for temporary membrane raptures during NS intrusion into cells. For this assay, cells were incubated with the same two NS concentrations (10 and 300 mM) as above and tested at 6 and 24 hours after the start of incubation. In this case the positive control was a sample of cells treated for 30 min with lysis buffer which leads to disintegration of the cells. Incubation with NS concentrations after 6 h and 24 h did not show any increase in signal compared to the negative control with untreated cells (Fig. 3.7). This demonstrates that gold Nanoshells have no cytotoxic effect on fibroblast cells. Our observation is also supported by recent findings using gold nanorods, which also show no detrimental effects after uptake into cells. [141]

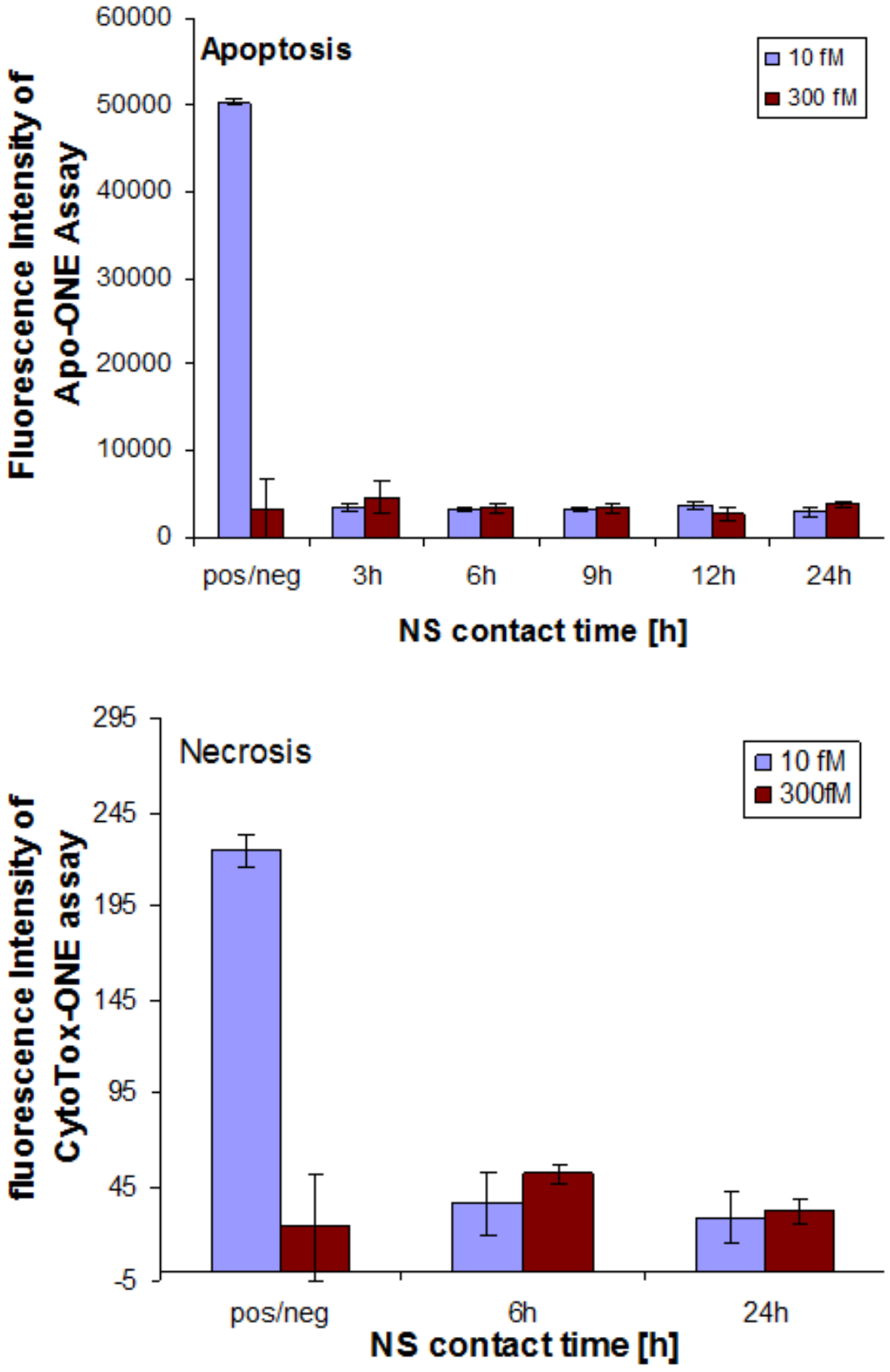

FIGURE 3.7: Apoptosis:Results of ApoONE homogenous Caspases 3/7 test for 10 fM (low) and 300 fM (high) NS concentrations incubated for up to 24h. Positive control was incubated with 2 mM Staurosporine for 24h, negative controls were untreated cells. Necrosis: Fluorescence results for CytoTox-ONE kit, positive control was obtained by lysing cells with provided buffer solution, negative controls were untreated cells. Error bars in above measurements were standard deviations of 5 replicates.

3.1.4 SER microspectroscopy with NS as Raman transducers

The NS used in this work are designed to be excited with lasers in the NIR region, which have excellent transmittance through tissue. To date these NS have been added to cells as a potential cancer therapy.[78, 142] However, they also have potential use as transducer elements for surface-enhanced Raman spectroscopy, like pH sensing or screening for biomolecular interactions .[77, 143] This section therefore demonstrates the use of NS to acquire spectra from the intracellular environment of living and viable NIH/3T3 cells, which can enhance the Raman signal even as single particles. [144] First the differences between non-enhanced Raman measurements collected using detached living NIH/3T3 cells and SERS spectra enhanced by intracellular NS of NIH/3T3 cells grown on quartz coverslips (UQG Ltd., Cambridge) were compared. In order to obtain a detectable bulk Raman spectrum 50 surface detached single cells were measured using 50 mW laser power with a 783 nm laser for a 180 sec acquisition time on each cell. SERS spectra were collected on cells incubated for 3 h with 300 fM of NS. After locating the gold nanoparticle light scattering pattern as shown in Figure 3.8, characteristic light scattering, and spectra were acquired for 5 seconds with 3 mW laser power at the sample on surface adhered cells. The SERS spectra were taken in several single living cells at different locations (Fig. 3.9). Comparing the two different kinds of Raman measurements some features are clearly visible in the bulk Raman as in the SERS spectra, such as the peak at around 1005 cm^{-1} for phenylalanine or the Amide-III: beta sheet band at 1215 cm^{-1}.[38] However, we see no DNA related peaks in the SERS spectra; this is expected if, as shown before, NS are only found in the cytosol. Other peak assignments can be found in Table 5.1 and are taken from the literature.[145] Literature values for Raman shifts are commonly used, but not completely reliable, as every acquisition and every experimental set-up is giving slightly different values. For that reason, only in this part an estimate was used to show what kind of information could be deduced from Raman spectra of a mixture of compounds. Chapter 4.2 later on introduces a novel way of Raman spectra analysis. Equation 3.1 shows which assumptions have been made to estimate the intracellular surface enhancement. The standard way for the calculation would

include taking into account how many molecules can be found in the region of the surface plasmons and the Raman cross-section of the molecules. Inside a cell these factors can be neither controlled or assessed. Therefore the different factors of a bulk Raman cell measurement and the SERS measurement of NS were compared directly. This basically consists of four parts. The first is comparing the volume which is investigated with both techniques. In the case SERS the probing volume only involves the close surrounding of the NS, approximately a shell of 10nm height. The second part is the time t_{bulk} vs t_{SERS} used for each acquisition, and third, the laser power in both cases, I_{bulk} and I_{SERS}. Last but not least, the signal to noise ratios of the spectra were compared by SN_{SERS} devided by SN_{bulk} of spectra. The calculated estimate for the enhancement of the Raman signal of cytosolic compounds with NS has been determined to be 10^{10} compared to the single cell Raman measurements. This number lies surprisingly very close to the reported enhancement factor of 10^{12} for NS. [144]

$$E_{fest} = \frac{V_{bulk}}{V_{SERS}} * \frac{t_{bulk}}{t_{SERS}} * \frac{I_{bulk}}{I_{SERS}} * \frac{SN_{SERS}}{SN_{bulk}} \tag{3.1}$$

E_{fest}	enhancement factor estimate
V_{bulk}	total cellular volume probed using bulk native Raman
V_{SERS}	cytoplasmic volume probed by SERS where V_{SERS} = NSEA$_{maxvol}$ NS$_{vol}$ where NSEA$_{maxvol}$ represents the volume of a sphere with radius 10nm greater than the NS wherein SERS enhancement is expected and NS$_{vol}$ represents the volume of a nanoshell
t_{bulk}	acquisition time for unenhanced Raman measurements of cells
t_{SERS}	acquisition time used for SERS of cells with NS
I_{bulk}	laser power used for unenhanced Raman measurements
I_{SERS}	laser power used for SERS measurements
SN_{bulk}	signal to noise ratio for unenhanced Raman spectra
SN_{SERS}	signal to noise ratio for SERS spectra

Although we gain a very sensitive and gentle way for intracellular Raman investigations, the actual information which can be acquired is rather unspecific. For a useful intracellular sensor high specificity to either certain cellular conditions, like pH or redox potential, or for the detection of marker molecules for different cellular processes is desirable.

In order to measure pH, we used of 4-MBA functionalized Au particles, intracellular pH determination has been shown by Kneipp *et al.* where the particles were

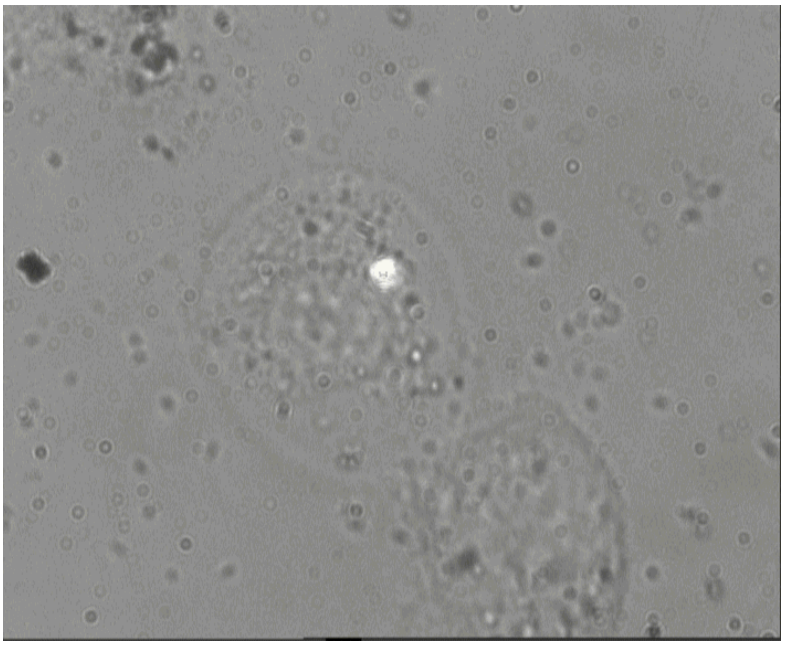

FIGURE 3.8: Image of characteristic circular scattering of NS in NIH/3T3 cell. Cells were treated the same as cells for bulk Raman measurements, detached from surface by trypsinisation, except that these cells were incubated with 300 fM NS for 3 h beforehand

"probably located in lyzosomes".[139] The NS-pH sensors have been made as a test platform. For the use of a nano sensor it is of high importance, that surface functionalities remain intact whilst inside the cell and the spectra are not disturbed by signals originating from foreign molecules adhering to the sensor surface. We use 4-MBA functionalized NS for this simple test as 4-MBA is known to easily form self assembled monolayers on Au surfaces.[77, 143] The spectra (Fig. 3.10) of 4-MBA-NS inside cells and free in media do not show any obvious differences. The dominant features in the spectra are the aromatic ring breathing modes at 1081 and 1590 cm^{-1}. Other less intense features describe the S-C stretching mode of the thiol function at 527 cm^{-1} , different carboxyl modes at 860 cm^{-1} (d(COO-)), 1150 cm^{-1} (C-COOH), 1430 cm^{-1} (-COO^{-}) and at 1700 cm^{-1} the protonated carboxylic acid group (-COOH),[77, 143] which are all dependent on the pH of the surrounding solution. In the above shown spectra the pH can be determined to be pH 7.4 for the particles in the growth media and pH 6.5 for the NS-4MBA inside the cell (pH calibration data in appendix) calculated from the peak ratios between

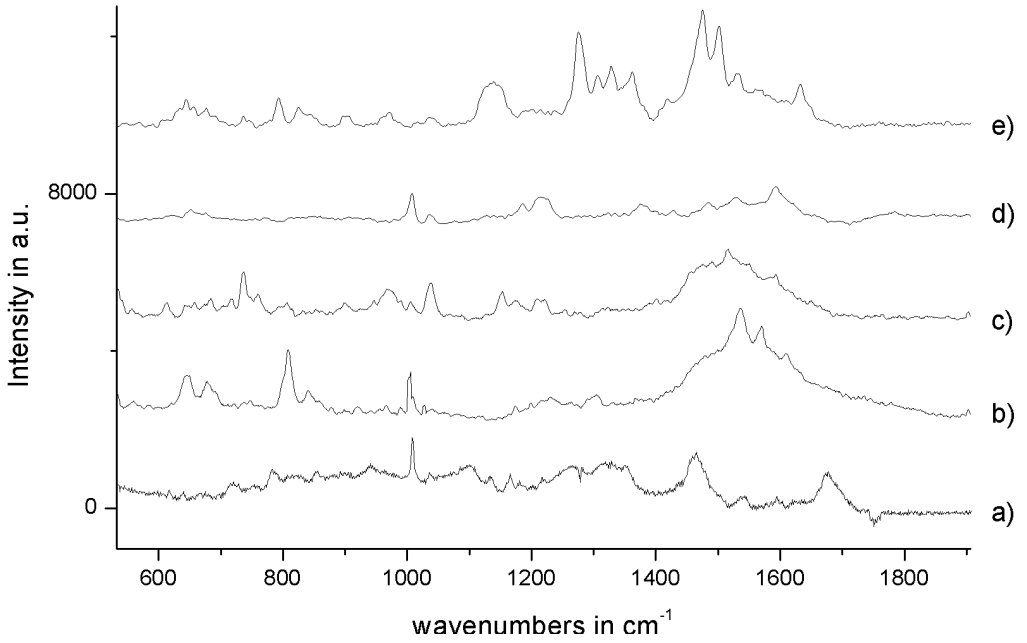

FIGURE 3.9: a) Averaged Raman spectrum of 50 different NIH/3T3 fibroblast cells measured at a 785.32 nm excitation wavelength, 50 mW laser power at the sample for 180 sec. b-e) SER spectra taken by excitation of NS in different cells at the same wavelength with 5 sec acquisition time and 3 mW laser power at the sample.

the peak intensities at 1430 cm^{-1} and 1700 cm^{-1}. By retracing the intensity ratios of both spectra in the pH calibration curve, the pH can be determined.

3.2 Conclusion NS in cells

The bulk of this work examines Surface-enhanced Raman Spectroscopy (SERS) for sensing application outside and inside cells, with the ultimate goal of intracellular SERS for protein detection. In this chapter it was shown that the 150 nm nanoparticles, aka Nanoshells (NS), were taken up into cells and the possible uptake mechanism investigated. It was found that NS are voluntarily taken up into NIH/3T3 fibroblasts. The amount of particles can be controlled by either

TABLE 3.1: Comparison of Ramanshifts in Single cell and intracellular SERS measurements.[37, 38]

Single cell	Assignment for Raman features NS in different cells.				
a)		b)	c)	d)	e)
640	C-C twist in Tyrosine	646		642	644
675	C-S stretch in Cysteine	678	684		
720	C-N stretch in lipid/adenine		736		737
783	DNA: O-P-O backbone stretch in T/C				
825	Out of plane ring breath in tyrosine				825
856	In plane ring breathing mode tyrosine	848			850
893	C-C skeletal stretch in protein		900	905	896
941	C-C skeletal stretch in protein		967		972
1008	Sym. ring breathing mode phenylalanine	1005	1005	1007	
1036	C-H in plane bending mode phenylalanine	1037	1038	1036	
1100	DNA: O-P-O backbone stretching				
1109	DNA: O-P-O backbone stretching				
	C-N stretch in polypeptide chains		1133	1138	1139
1166	C-C stretching in proteins	1174	1174		
1217	Amide III: beta-sheet	1216	1209	1214	1214
1266	Amide III: beta-sheet/adenine/cytosine				1275
1329	Guanine			1323	1329
1354	Polynucleotide chain (DNA bases)				
	Possible porphyrin stretches			1375	1366
1465	(v (C = C) + v (C- C) + v (C = O .-. H))			1485	1475
	Aromatic ring stretches		1516		1511
1543	Lipid stretches	1535		1528	1534
	Tyrosine stretch	1570		1593	1570
1595	Ring mode (Adenine/guanine)				
1619	C=C bending in phenylalanine and tyrosine	1616			
1677	Amide I: alpha-helix				

using different particle concentrations with which the cells are incubated and or by changing growth media conditions in which the particles are suspended during the incubation with cells. Regarding the later aspect it was observed that NS are more easily taken up into the cells when the media did not contain calf serum, which is normally provided for cell maintenance. The technique we used to investigate the uptake was TEM, this allowed the location of the NS and also provided high magnification information on the local environment of the NS inside the cells. Here the difference between the uptake conditions with and without CS

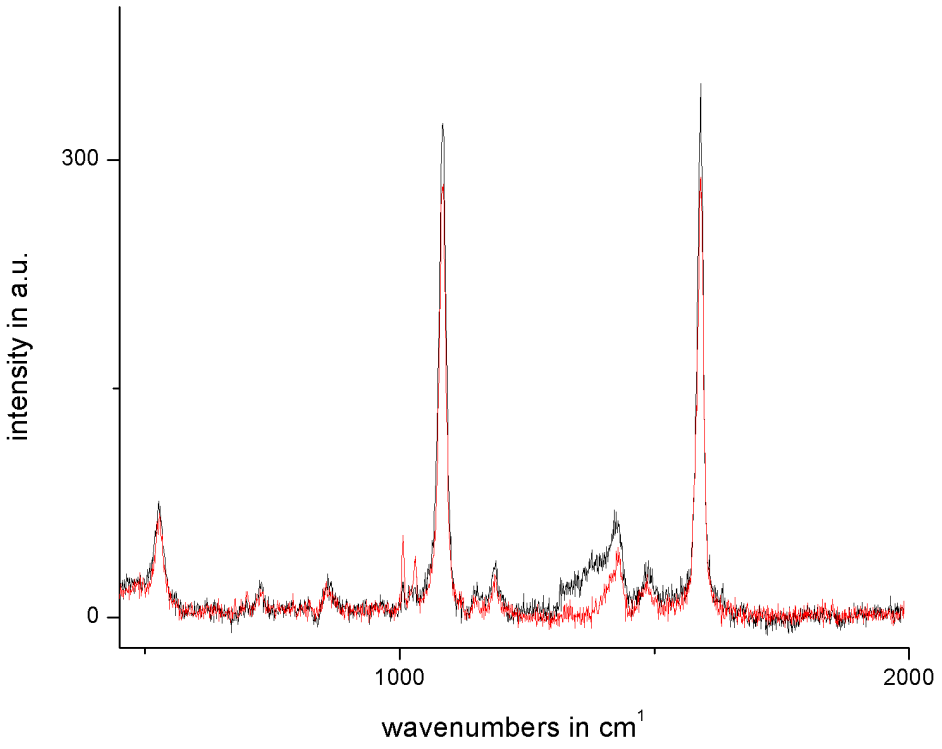

FIGURE 3.10: SER spectra of 4 mercaptobenzoic-acid functionalized NS in NIH/3T3 fibroblast. Overlying spectra depict NS-4MBA in solution (black) and inside NIH/3T3 cells determining the pH to be 7.4 and 6.5, respectively.

also showed distinguishable observations, but have one thing in common, particle uptake can be observed into the cytosol, not into the nucleus. In the case of incubation with CS in media NS were internalized in lysosomes or surrounded by either a dense coating of proteins or a lipid bilayer. Similar results were reported before for small nanoparticles, and were used to suggest an endocytosis mediated uptake mechanism which is dependent on serum proteins on the particle surface. In the second case described the TEM images showed the particles freely suspended in the cytosol without coating. This finding negates the dependence of serum proteins for NS internalization and furthermore opens a way for the non-coated internalization of particles into the cytosol - this is crucial for applications in cytosolic intracellular (protein) sensing.

We then investigated this interesting result further with studies into the uptake mechanism. Here we found that the particle uptake is not dependent on a particular endocytosis mediated uptake mechanism since our attempts to rule out the four best known possible pathways didn't show any change in uptake. In fact, it is only in the case of the depletion of cholesterol that an increase in the uptake rather than the anticipated decrease could be observed. This, in connection with an increased uptake in serum free media, suggests a possible passive uptake mechanism which depends only on membrane fluidity.

Having investigated the uptake, it was important to investigate that NS don't harm the cells or invoke adverse cellular responses. To this end, cell viability tests were conducted by bringing and leaving cells in contact with NS containing solutions of different concentrations over 4 days and comparing these with the growth behavior of the same sort of cells at standard conditions. The results obviously showed that cells incubated with NS at concentrations between 10 and 300 fM (which coincides with 1-30 NS taken up into one cell) show perfectly normal growth and seem to be non-toxic. To further, prove that NS are non-toxic, we showed that cells are do not enter apoptosis, by testing for the presence of early apoptosis markers like caspases 3 and 7. Furthermore, we also tested for necrosis end eliminated this possibility by assaying for the breaking/lysis of membranes during the particle incubation which could lead to elevated levels of extracellular lactase. Since these three tests indicate that NS are non-toxic, we can therefore assume that they constitute a useful class of SERS transducer for intracellular investigations in fibroblasts, and most probably for various cell types.

First intracellular SERS studies gained an enhancement factor of 10^{10} and therefore is a very attractive approach for cellular imaging. The only drawback at this stage with bare nanoparticles is an unspecific signal, showing random molecules surrounding them. This will be tackled in the next section of this work, and a reliable protein detection system based on NS transduced SERS measurements developed. What also has been proven in this chapter is that the well known pH-nano-sensor with MBA as reporter molecule, can be used intracellular with NS, and therefore promises to provide good results with further sensing applications. [118]

Chapter 4

NS based SERS for protein sensing

4.1 DNA aptamer based approach for Protein sensing

4.1.1 Introduction

The ability to measure molecular binding events in real time, without labeling, is critically important in aiding our understanding of biological processes.[143, 146] This work demonstrates that the binding between an aptamer and unlabeled protein can be detected by measuring changes in the surface-enhanced Raman spectroscopy (SERS) signal of the aptamer caused by conformational changes which arise from formation of an aptamer/protein complex. While Raman spectroscopy has huge potential for probing such biomolecular systems,[147] it has historically suffered from low signal intensities. High laser power can often compensate for low intrinsic signal, but can also lead to photo-damage of the sample. SERS is an alternative Raman technique which uses the plasmon resonance of noble metal particles or nanoscale surface structures to increase the Raman signal of analytes near the surface and therefore requires lower laser power, shorter acquisition times, and is increasingly valuable for measuring Raman spectra from dilute or photosensitive

samples. SERS can be used to measure spectra from sensitive biological samples and has been already applied in investigations of the live cell intracellular environment, with various approaches, for example for the investigation of pH conditions inside cells.[148] Novel SERS substrates which exhibit high enhancement factors can be designed for specific purposes, e.g. core shell particles, resonant at near IR wavelengths are suitable for biomedical applications.[81] As shown in chapter 3, NS can be easily introduced into mouse fibroblast cells in a controllable non-toxic way for the measurement of SERS spectra without harming the cell or inducing a cellular immune response.[118] Biomolecular detection has been demonstrated using several approaches which facilitate SERS on nanoscale roughened noble metal surfaces or by using nanoparticles in a "sandwich" format, like in the work Lin *et al.* presented in which the Raman reporter labeled nanoparticles bind via antibodies to the target protein.[149] A few approaches for SERS detection of proteins have used aptamers, which are highly specific oligonucleotide probes that bind target molecules in a similar fashion as antibodies with high specificity.[150] In these cases, Raman active dyes are generally attached to one end of the aptamer and are drawn closer to the surface of the SERS substrate during binding of the target protein and conformational change of the aptamer, leading to a large enhancement of the dye spectrum.[151, 152] Perhaps the best characterized aptamer of this kind is the thrombin binding aptamer (TBA)[153] which can be used as an inhibitor of blood coagulation. The ability to form a stacked G-quadruplex structure is important for binding and its disruption has been shown to destabilize the aptamer/protein complex.[154] The wealth of characterization data available for this aptamer makes it an ideal candidate to use as a model-system for the development of new detection methods. Having these features in mind it was suspected that a change in the characteristic SER spectrum of the TBA aptamer can be observed, which might reveal itself as a shift in the Raman modes for the aptamer or the appearance of features characteristic for the target protein or completely new peaks describing the aptamer target interaction (Figure 4.1).

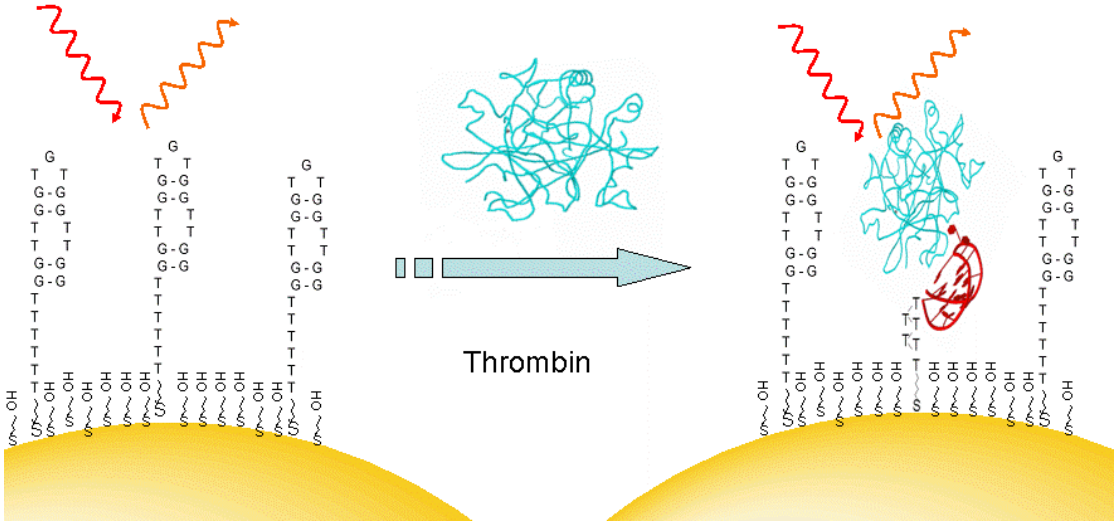

FIGURE 4.1: Sketch describing the TBA aptamer modfied sensor surface before and after incubation with thrombin.

4.1.2 NS modification with oligonucleotides

As described in the Methods and Materials section commercially available amino-propyltriethoxy-silane (APTES) modified glassslides and Auroshell^{TM} NS were used. Using commercially available materials, should increase the reproducibility of the sensing platform. The NS form small aggregates with a size of ca. 0.5-5 μm diameter on the surface and also form a pattering that is referred to in the literature as "coffee" stain (a circular ring of aggregated nanoparticles).[155] The particles assume a structure of layered and seemingly regularly distributed NS as can be seen in the AFM image taken of one of the NS aggregate sensor spots modified with oligonucleotide, later used as one of the sensor spots, in Figure 4.2a. In the profile of a representative cross-section in (Figure 4.2b) it appears that the particles have a trend to form gaps of a width between 0-25 nm. This gives us easy access to SERS platform for *in situ* measurements and proof-of-principle experiments.

For best results in the development of an aptamer based sensor the favourabloe conditions for the modification of the NS and NS-aggregate surface with thiol-modified TBA oligonucleotide was determined by X-ray photonelectron spectroscopy (XPS) measurements and different modification conditions. XPS is a surface chemical analysis technique that can be used to analyze the molecular composition of

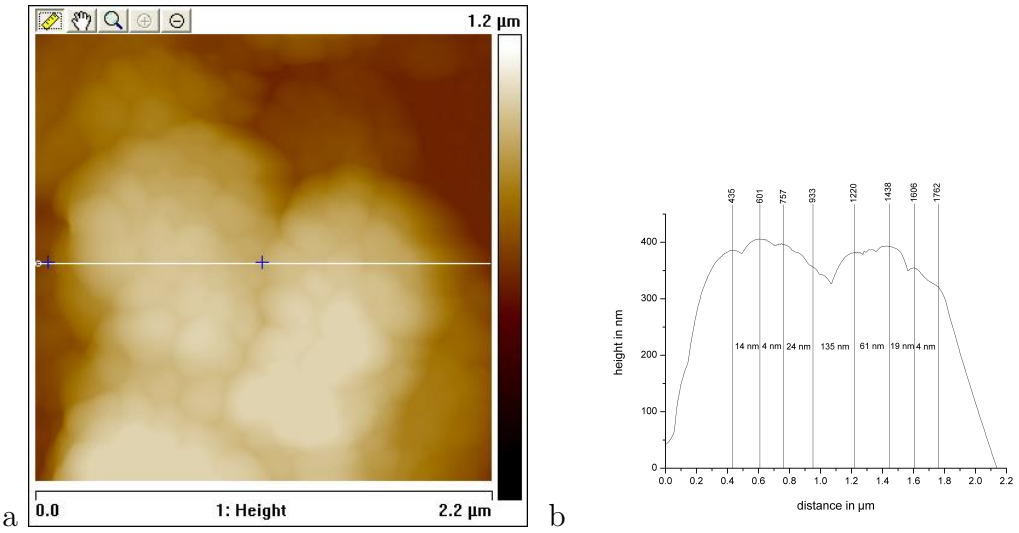

FIGURE 4.2: a) Representative AFM image of TBA functionalized NS aggregates selfassembled on Amino-silanized glass slides. b) Profile of cross-section of the same NS aggregate showing the different distances between NS estimated by using the highest point of a NS curvature as the center of the particle.

the surface of a material. By investigating the way that the surface interacts with a beam of X-rays, the chemical elements and their oxidation states can be determined by looking at the binding energy of functional groups. In the case of DNA, for example the phosphate groups can be observed. Other possible functional groups of the used oligonucleotide have been nitrogen, oxygen, sulfur or carbon. We chose to integrate the phosphate peak because other peaks suffered from high background signal. Figure 4.3 shows that depending on the buffer conditions the oligonucleotide amount on the surface varies. For this the amount of phosphate via the P_{2p} binding energy was measured, integrated and normalized to the signal obtained of gold the surface (Au_{4f}) of the NS. We see that there are distinct differences between reaction/buffer conditions. Table 4.1 gives details of the buffer conditions in Figure 4.3.[156, 157] The errorbars describe one normalized standard deviation of three independent measurements (∼10 %). Therefore we can distinguish between reaction conditions (BB1/BB2/water) as well as reaction times, with an already measurable amount of DNA after 2 h for BB1 which increases after SAM formation up to 36 h. On the other hand the data shows that there is no influence of temperature ($4°C \leftrightarrow 25°C$) on this reaction. For all further experiments BB1 was used. Furthermore since the G-quadruplex, is an important feature of the aptamer/protein complex of the TBA oligonucleotide

and human α thrombin and is stabilized by cations like K^+ or Mg^{2+}. The buffer used in this study consisted therefore of 10 mM of KCl and $MgCl_2$ and 120 mM of NaCl at a pH of 7.4. During interaction with the target, the aptamer adopts a stacked G-quadruplex structure forming a "rocking chair" like shape, as shown in the structure determination by Padmanabhan *et al.*[153]

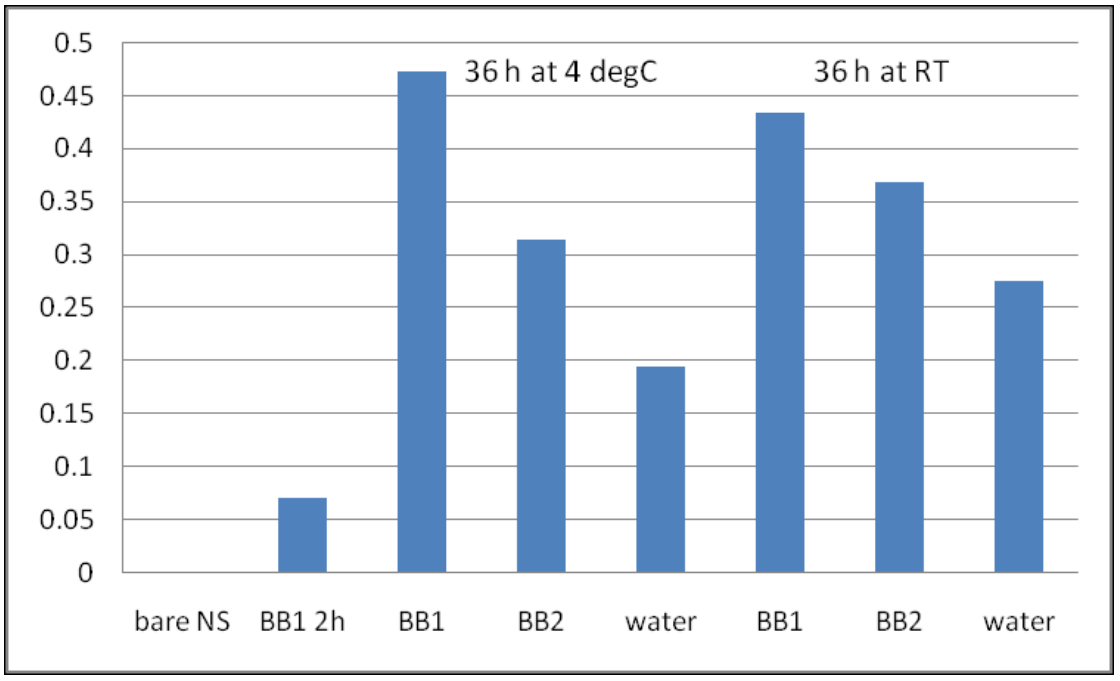

FIGURE 4.3: Measured amount of phosphate containing DNA found on aggregate surface with different buffer conditions, contact times and temperatures.

TABLE 4.1: Reaction conditions for thiol modified thrombin binding aptamer (TBA) surface modification.

Chemicals	BB1	BB2	H_2O
Tris-HCl	50 mM	50 mM	n/a
NaCl	120 mM	50 mM	n/a
$MgCl_2$	10 mM	1 mM	n/a
KCl	10 mM	0 mM	n/a
pH	7.4	7.0	7.0

4.1.3 Initial Raman investigations of NS-TBA

The oligonucleotides which were studied were conjugated covalently onto the gold surface by a 5'-C_6-thiol linker. Between the actual DNA aptamer and thiol on

the 5' end a 6x thymine linker, which is empirically determined the most favorable length for Thrombin binding, was inserted in the sequence allowing the aptamer to reach out further from the gold surface (TTT TTT GGT TGG TGT GGT TGG).[152, 156] This improves aptamer-target interaction and secondary structure folding properties. The Non-specific binding of DNA or proteins to the gold surface was reduced by blocking the NS modified oligonucleotdies with a self-assembled monolayer of mercapto-hexanol (MCH) which was applied as described in chapter 2 and is preferable to other investigated agents, like completely hydrophobic molecules.[157] This also has an important influence on the Raman spectra of the surface bound oligonucleotide as has been observed taking SERS measurements of the sensing platform before and after mixed monolayer formation with MCH as shown in Figure 4.4. The first spectrum shows that a very strong signal in the NS aromatic ring shift region at around 1450-1600 cm^{-1}. Spectra of this kind of surface modification did not change when incubated with the target protein (data not shown). The second spectrum after MCH incubation for 30 min and washing in BB1 shows only comparably weak signal for example the ubiquitous DNA phosphate stretch at $\sim$1080 cm^{-1} which will be referred to later as an internal standard. The decrease in signal can be explained by blocking DNA gold interactions, which pull the DNA close to the surface. All further experiments were then conducted with mixed monolayers of biomolecule (aptamer) and MCH.

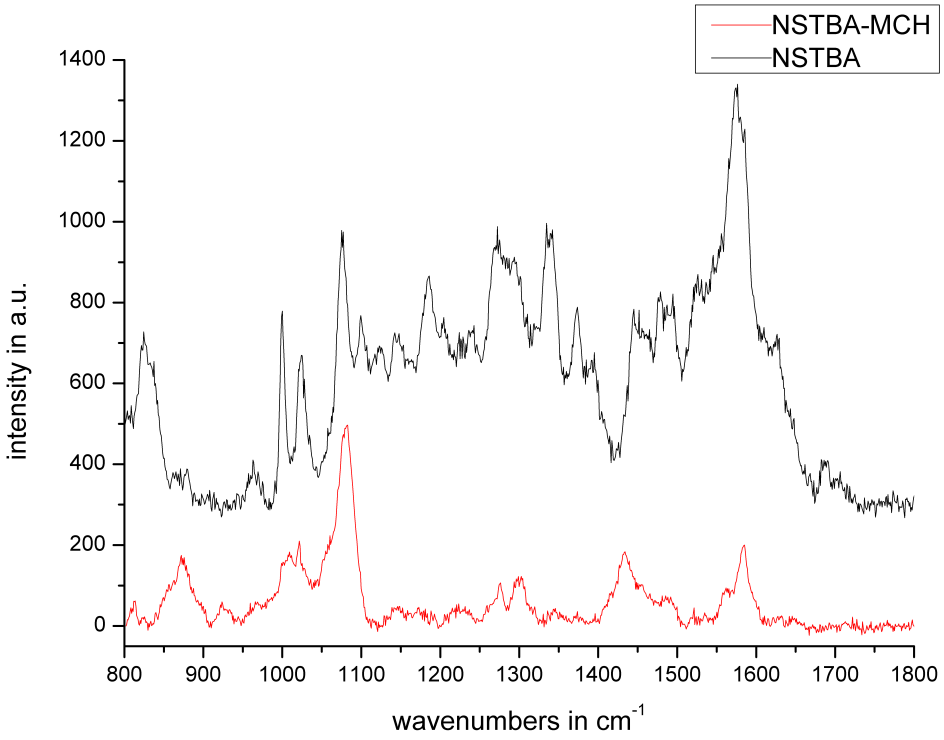

FIGURE 4.4: Graph shows the Raman spectra acquired for NS-TBA before formation of a mixed monolayer of MCH on the NS surface.

4.1.4 NS-TBA for the detection of thrombin

With the knowledge that NS solely modified with TBA does not show any spectral changes during target protein interaction, the following describes the results obtained during incubation of TBA-MCH mixed monolayer covered NS with the target protein human α thrombin (h αT) in a mixture with human serum. As shown above the SERS signal of the functionalized NS has only few features with the already mentioned phosphate backbone stretch at ∼1090 cm^{-1}. Weaker signals can be found at a Raman shift of 850-900 cm^{-1}, aliphatic vibrations, ∼1000 cm^{-1}, probably stemming from aromatic vibrations, between 1200 cm^{-1} and 1300 cm^{-1} as well as between 1550 cm^{-1} and 1600 cm^{-1} of hetero-aromatic rings of the oligonucleotide.[37]

To test the behavior of the sensor, the TBA modified NS aggregates were incubated with 10 nM of human α thrombin in BB1 for 30 min at RT. Figure 4.5a

shows a comparison of the signal obtained after incubation with 10 mM of human α thrombin with a list of different control experiments. We experience an extraordinary increase of features as well as a rise in signal intensity for distinct Raman shifts as well as for broader features. A first comparison between spectra taken of NS-TBA as well as control experiments, incubating NS-TBA with different non specific proteins like, bovine serum albumin (BSA), insulin and human serum (HS) still shows the prominent O-P-O-stretch with very similar intensity as before.[38]

Due to its stability and reproducibility this peak was used for normalization purposes. Furthermore the obtained features can be split into two categories. Sharp peaks like at 822, 1140, 1203, 1480 and around 1550 cm^{-1} and broad and weak features like between 900-1000 cm^{-1}, 1250-1330 cm^{-1} and a very broad feature covering the region around 1400 cm^{-1}. The sharpness of Raman features gives information about how well a molecule and a group of the same molecule is ordered in relation to the surface plasmons as well as the environment the vibrational mode can be found in. In this case this would mean that we have on part of the setup after thrombin incubation well ordered and only in one configuration and another part which is presenting many overlapping but similar vibrational modes. An easy experiment, which is giving information about the origin of the observed Raman signals, (Figure 4.5b) allows the general correlation of the 3 components (TTP, GTP and hαT) available in the system to the obtained signals after target incubation. The SERS spectra here were obtained after incubation of bare NS aggregates with thrombin (1 mM), GTP (10 mM) and TTP (10 mM) overnight and spectral acquisition with the same conditions as for the sensing experiment. We observe here that TTP and GTP have strong and well resolved features whereas the spectrum for thrombin only shows broad peaks. This makes a classification of the signal possible. The sharp features in Figure 4.5a can be found in the SERS spectra of GTP adsorbed on NS and to a lower extent and intensity in the spectra of TTP. The broad and weak features seem to be caused by the target protein thrombin, as the spectrum of hαT is very similar, but not completely identical. These differences are caused by the different forms of representation of the protein towards the enhancing surface. The pure protein adsorbs randomly on the gold surface and therefore shows an average of the Raman modes. During the sensing

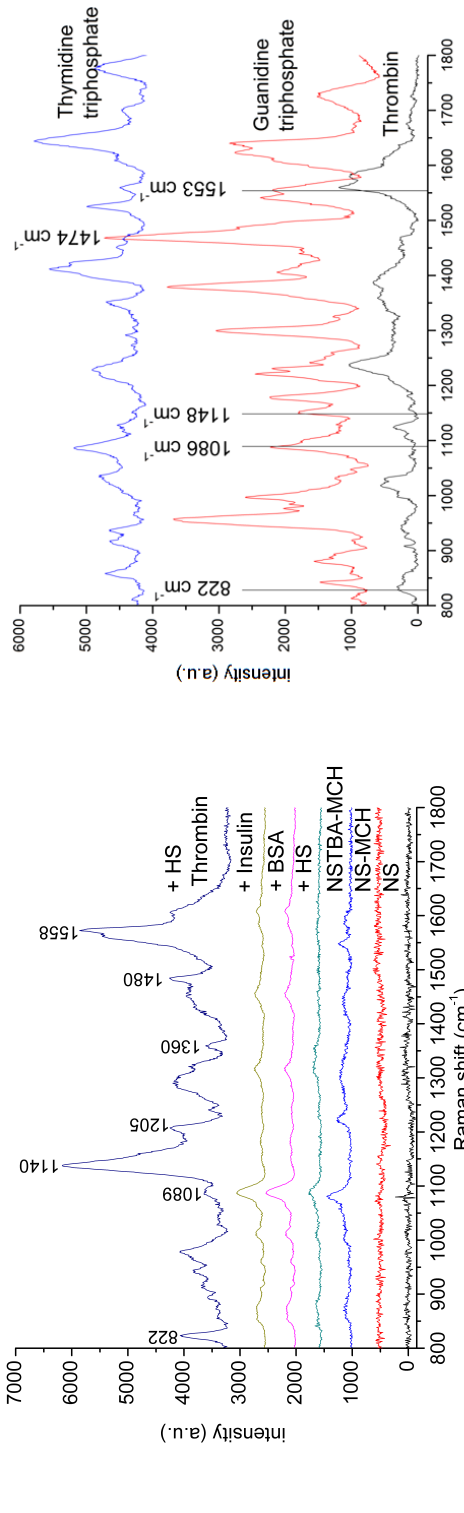

FIGURE 4.5: a)Spectral changes caused by human α thrombin (10nM) binding to NS-TBA sensor. The dominant peaks can be assigned to DNA vibrational modes with a lesser contribution from protein vib.-modes. Controls with BSA (10 mg/ml), insulin 600 nM and 1% human serum show no non-specific protein binding. Lower three spectra show spectra of NS, NS plus blocking agent (mercapto-hexanol) and the fully assembled NS-TBA sensor. Spectra are averages of 10 acquisitions.b) Spectra of thymidine triphosphate, Guanidine triphosphate and human α thrombin adsorbed on bare NS aggregates overnight. Spectra were acquired the same way as for the sensor.

the target protein only the area of the heparin binding site can interact with the surface plasmons of the nanoparticles leading to less features but better better resolved features.
Representative Raman spectra of NS, NS covered with MCH, NS-TBA in binding buffer; after 30 min incubation with different control samples (BSA 10 μM, human serum 1% and insulin 0.6 μM) and after incubation with target protein thrombin in binding buffer are also shown in Figure 4.5. In the case of NS and NS-MCH, the spectra show no detectable signal. The spectra of the completed NS-TBA-MCH sensor show only weak signals with a prominent and stable feature at 1089 cm^{-1} assignable to the DNA O-P-O backbone stretch. Spectra of the sensor incubated with non-target proteins show weak signals similar to the background spectrum of the sensing platform.

Only incubation of the cognate target protein leads to a clearly visible change in the spectrum of the NS-TBA sensor. The sharp Raman features which appear after incubation with 10 nM thrombin at 822 cm^{-1}, 1140 cm^{-1} and 1558 cm^{-1} can be assigned to the combined C2'-endo and C3'-endo modes of the 2'-deoxyribose sugars, the C-O-C stretch at 1140 cm^{-1} and guanine ring modes at 1558 cm^{-1}. At 1480 cm^{-1} we observe another feature with lower intensity which can also be assigned to a guanine ring mode.[158, 159] Further signal increases can be assigned to vibrational modes of protein, such as the amide III backbone vibration at 1220 cm^{-1}, CH_2 stretching mode at 1440-1460 cm^{-1} or tyrosine aromatic ring vibrations at 1610 cm^{-1}.[160] A control experiment using a random oligonucleotide didn't show any changes on thrombin incubation (Figure A.2). We believe that the strong spectral changes are due to the formation of the G-quadruplex conformation of the aptamer on protein binding. This suggests that formation of a G-quadruplex structure positions key nucleotides closer to the gold surface and in a better position to interact with surface plasmons. In previous SERS studies by Halas *et al.*[161] it was shown that the hybridization of oligonucleotides leads to changes in Raman shifts. The same authors have also described the correlation between dsDNA orientation and SERS signal intensity and found signal increases depending on the angle between the molecule and the surface.[161]

To study the reproducibility and the re-usability of the sensor successive washing steps were performed with solutions of first 8 M Urea and secondly 0.2 M

Ca^{2+}-EDTA-containing buffers and re-incubation with 10 nM thrombin in BB1 was performed. Urea was chosen to destabilize the protein aptamer complex. The second washing step with Ca^{2+} and EDTA disrupts the Mg^{2+} and K^{+} stabilized stacked G-quadruplex. Spectra acquired after the washing lead back to the low intensity starting signal and signal increases repeatedly after 10 nM human α thrombin incubation and decreases in a reversible fashion (Figure 4.6). This figure also compares the characteristic binding signals of the protein-aptamer complex with those from control measurements. The characteristic signals are highly reproducible. Furthermore, we observe the same spectral changes when incubating the sensor with thrombin doped into human serum (Figure 4.6 last row) confirming that we can observe this specific biomolecular interaction even in a complex biological matrix and obtain the same signal. A 2D column plot inclusive errorbars can be found in the appendix in Figure A.3.

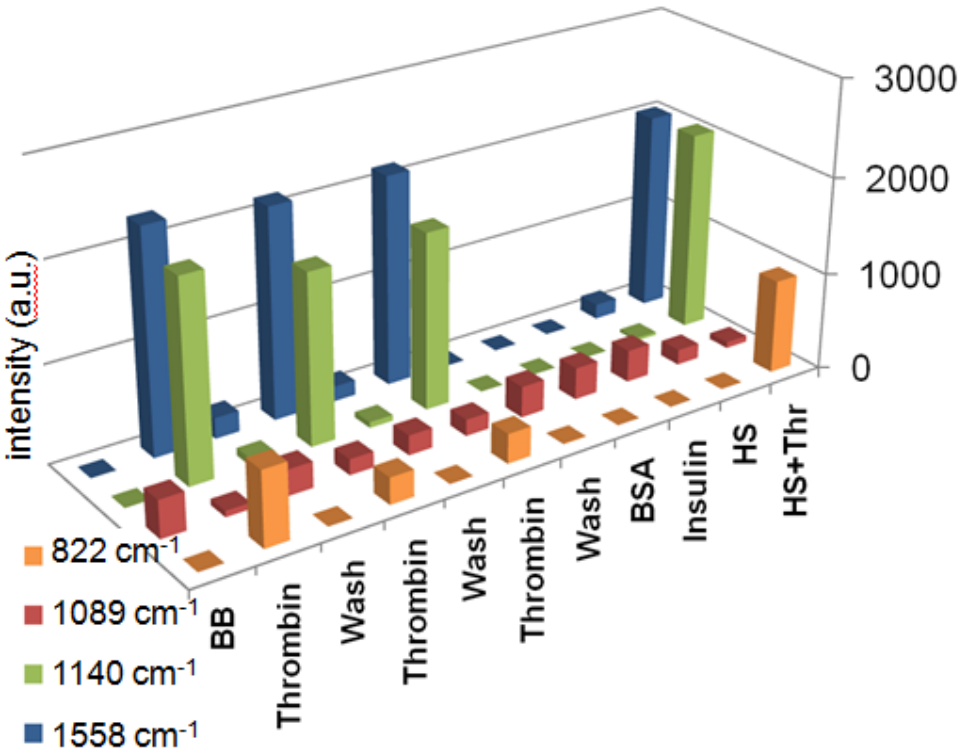

FIGURE 4.6: Washing and target incubation cycles of NS-TBA with 10 nM thrombin. Graph shows intensities of dominant peaks. Peak intensities are highly reproducibly at every incubation cycle. A further incubation in which 10 nM thrombin was dissolved in a 1 % solution of human serum produced similar peak intensities. Control experiments incubating only with bovine serum albumin, insulin and human serum do not show any increased signals compared to the washed sensor.

To determine the limit of detection (LOD) for thrombin detection a freshly prepared NS-TBA spot was incubated with different concentrations of human α thrombin in the binding buffer 1. The concentrations of target protein in solution ranged from 0 - 50 μM increasing in steps of 1 order of magnitude in concentrations beginning with 500 yM. The blank measurement was also taken to determine the detection limit, which is defined as 3 times the standard deviation of the measurements for the blank. Different protein concentrations were applied beginning with the lowest concentration, incubated with NS-TBA for 30 min and spectra taken as described before, raising the protein concentration continuously (Figure 4.7). Between every further incubation a washing step with BB was included to remove not bound thrombin from the sensor. The first concentration reaching the limit of detection can be found to be at 500 zM, with the actual number of molecules

in the probing volume of 50 μL being calculated to be 15. The first significant data point above the limit of detection lies at 50 aM (∼150) molecules in probing volume) and therefore, regarding a possible error of 2σ, this approach can reliably detect thrombin down to 0.1 fM.

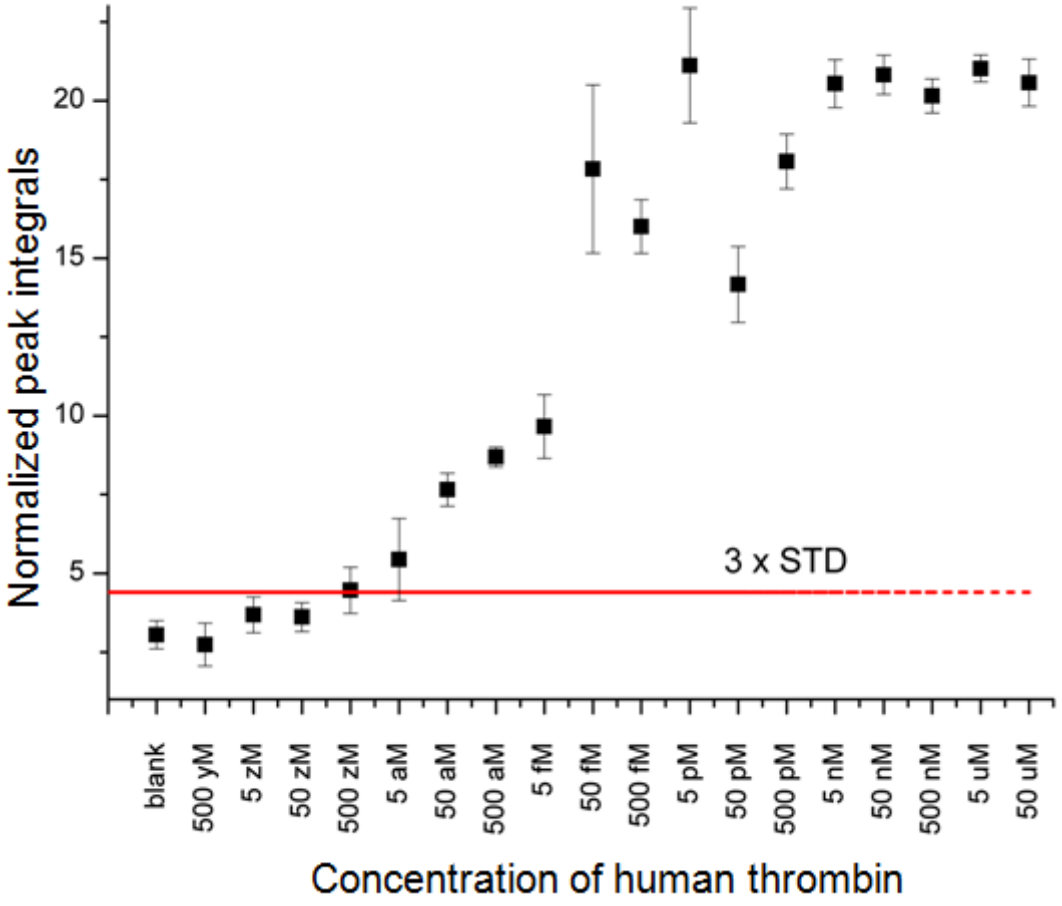

FIGURE 4.7: Result of the limit of detection (LOD) determination for NS-TBA in binding buffer for the cognate target protein human α thrombin. The sensor was incubated with protein concentrations between 500 yM and 50 μM. The red bar shows LOD (3x standard deviation) of the blank experiment.

4.1.5 NS-GFA (G-quadruplex forming aptamer) for investigation of heat dependent spectral changes

To prove the hypothesis that actually G-quadruplex formation has been observe and the universal validity of this approach for other G-quadruplex forming an aptamer was chosen selected by Yoshida *et al.* (2009)[162] for insulin binding. G-quadruplex forming aptamer modified nanoshells (NS-GFA) were prepared the same way as NS-TBA and the gold surface also protected with MCH before starting experiments.

On the investigation of the SERS signal of the NS aggregates modified with the 5' thiol modified oligonucleotide TTT TTT GGT GGT GGG GGG GGT TGG TAG GGT GTC TTC we first observed the similar background signal as for NS-TBA with the phosphate backbone stretch being the most prominent feature around 1080 cm^{-1} as can be seen in Figure 4.8. In this experiment a change of signal was noticed after 20 min of incubation in the same BB as used for the TBA which was assumed to promote the G-quadruplex formation due to cation stabilization. As can be seen in the SERS spectrum of this aptamer, secondary structure seems to form on its own and signal appears at the same Raman shifts at 820 cm^{-1} and 1132 cm^{-1} 1480 cm^{-1} and 1560 cm^{-1}. These peaks can be similar assigned as the prominent peaks of investigated TBA after target incubation with the features at 1480 cm^{-1} and 1560 cm^{-1} exhibiting reverse intensity ratio (Figure 4.8). The change in intensity ration of these two peaks was attributed to a slight difference in orientation of the G-quadruplex towards the surface plasmons, increasing the signal of the mode at 1480 cm^{-1} more than the other. These findings confirm that we actually observe the G-quadruplex formation as a result of thrombin binding on TBA.

As further proof SERS features in 4.8 are attributed to secondary structure temperature controlled disruption of the probable oligonucleotide secondary structure and simultaneous SER spectroscopy was performed. To investigate the temperature dependent behavior of this control oligonucleotide to illuminate the coherence between Raman signal and oligonucleotide secondary structure a melting experiment shown in Figure 4.9 was conducted by gradually heating the sensor from 30

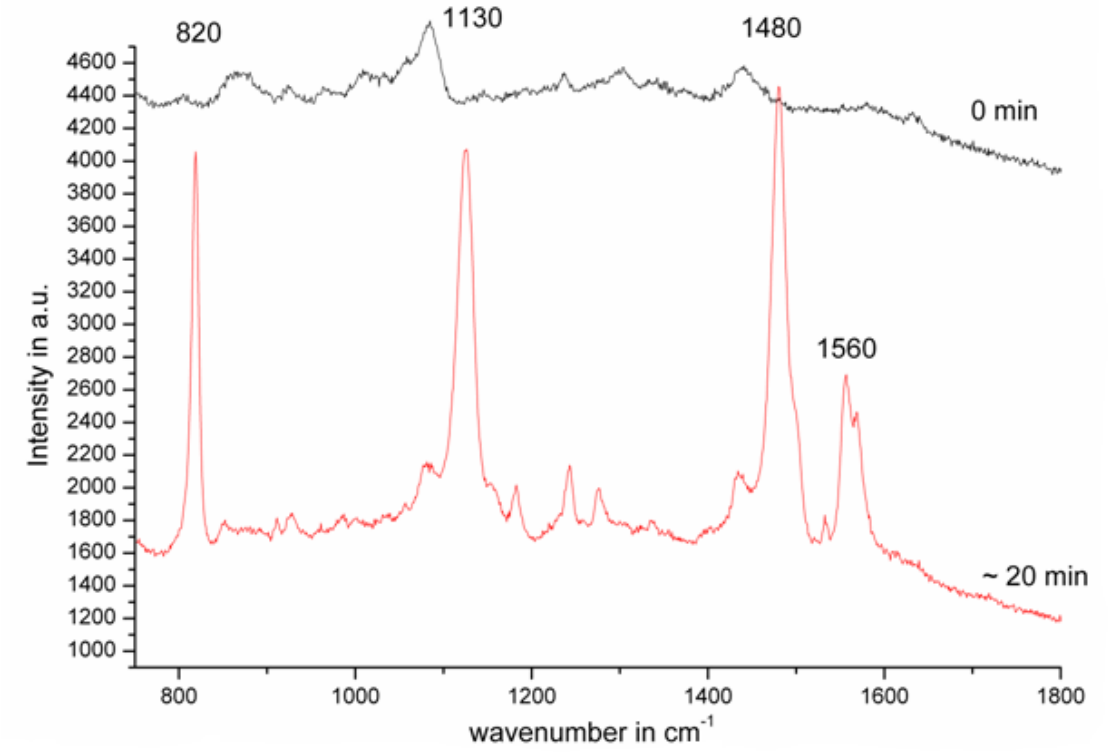

FIGURE 4.8: The graphs show the change in the spectrum of NS-GFA at the start of incubation in BB and after 20 min of immersion in buffer. The spectrum shows strong Raman bands at 820, 1130, 1480 and 1560 cm^{-1}. This suggests a target independent self-folding of the insulin binding aptamer.

°C to 70 °C with adjacent slow cooling to RT again to allow secondary structure formation. On temperature increase the signal decreases suggesting the gradual disintegration of the G-quadruplex structure, first slowly up to 40 °C, nearly no characteristic signal at 50-60 °C and only background signal at 70 °C. This temperature should perform melting of the secondary structure. Careful cooling back to RT of leads to the same characteristic Raman shifts and intensities and shows that the formation of the G-quadruplex formation, and folding of the GFA is a completely reversible process. Furthermore, this experiment also shows that suspected laser induced heating of the particle surrounding does not exceed 30 °C during the acquisition as this would automatically lead to signal loss. Although this experiment seems to give convincing proof of the disruption of the aptamer secondary structure this experiment has to be backed up by investigating possible heat dependent absorbance changes, which would cause apparent signal loss due to a decrease in absorbance. It is also important to back up the stated non existing

local heating by direct measurement of the anti-Stokes/Stokes (AS/S) scattering ratio at the employed laser power used during the experiments.

To measure the heat dependent absorbance of NS, a UV-Vis spectrophotometer was rigged with a temperature controllable peltier element with a possible temperature variation from 0-110 °C. NS suspended in water in a sealed quartz cuvette were then heated from 25 °C (RT) in 20 °C steps up to 95 °C. Figure 4.9 shows the results of this measurement and shows that the absorbance didn't decrease significantly up to a temperature of 65 °C. But further heating then led to a strong decrease in absorbance. This simple experiment therefore confirms that increasing the temperature during the above described and melting experiment should not have had an influence on the particle absorbance, therefore the SPR. As a result, the changes in SERS signal can be safely attributed to changes in molecular conformation.

a

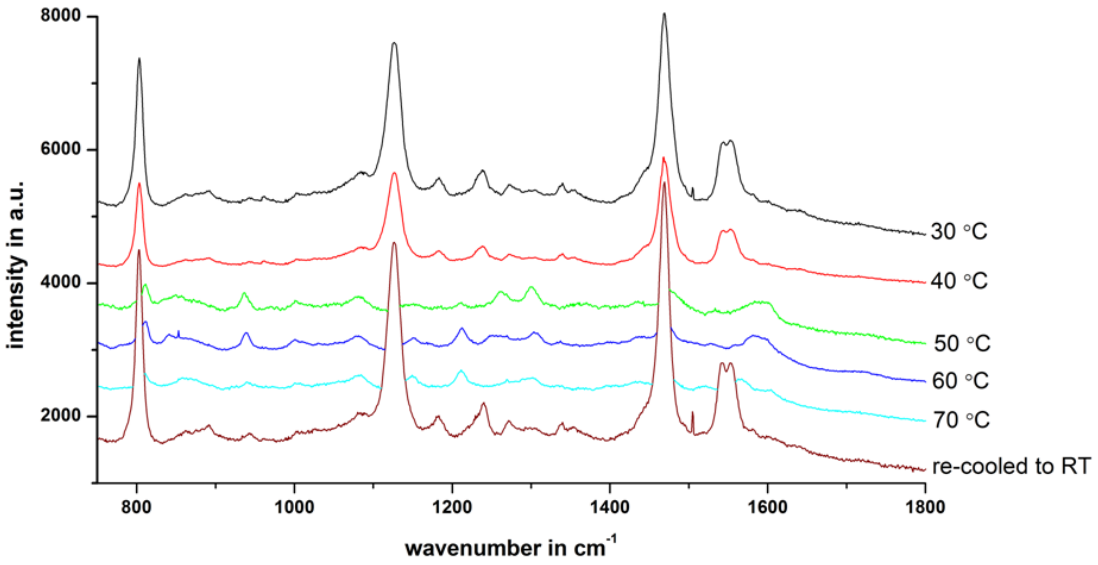

b

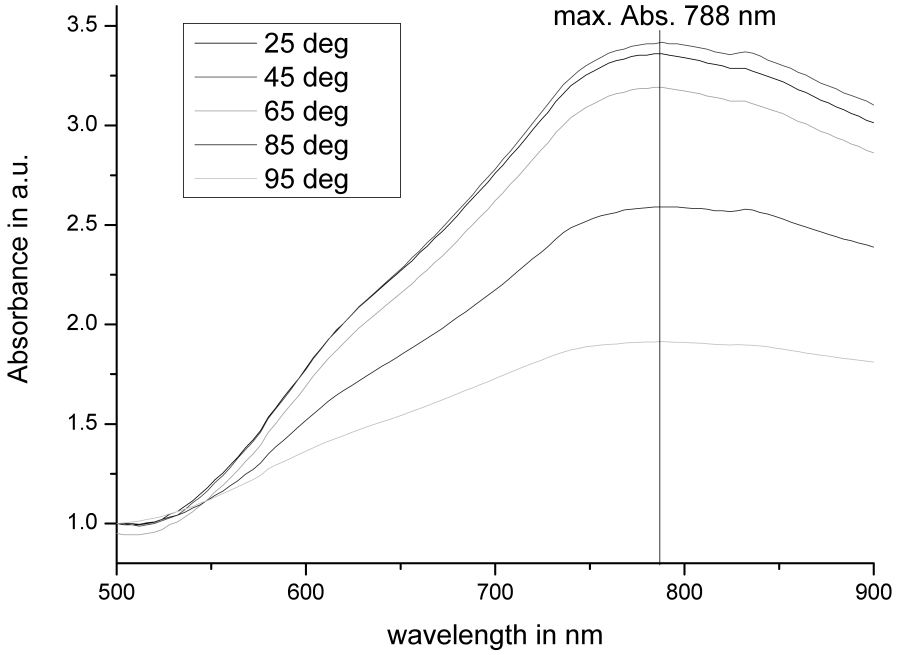

FIGURE 4.9: a)To show the relation between the oligonucleotide secondary structure and the signal of the self folding GFA we increased the temperature and observed the change in Raman spectrum. Spectra show averages of 20 spectra with acquisition times of 10 sec. Temperatures were increased in 10 °C steps from 30 °C up to 70 °C and the intensity of the marker bands decreased in intensity. Cooling back to RT after the 70 °C measurement gave spectra with the original high intensity signals and we therefore suggest that the oligonucleotide refolds to its original structure at low temperature. b)Influence of heat on absorbance of NS at temperature range observed in IBA melting experiment is negligible and not cause of signal reduction.

$$\rho = \frac{I_{AS}}{I_S} = A_\omega \frac{\sigma_{AS}}{\sigma_S} \sum_{j=1}^{N} \frac{A^j_{AS}}{A^j_S} exp(-\hbar\omega_v / k_B T_m ol) \tag{4.1}$$

ρ	AS/S ratio
I_{AS}	spectral intensity of Anti-Stokes mode
I_S	spectral intensity of Stokes mode
$A\omega$	equals $(\omega_L + \omega_v)^4/(\omega_L - \omega_v)^4$ accounting for the standard wavelength dependence of Raman processes
N	number of active molecules
$A^j_{AS(S)}$	the SERS enhancement factor at anti-Stokes (Stokes) frequency

The negligible heating of NS during measurements has been also confirmed by observing the anti-Stokes/Stokes ratios during a 1.5 h long experiment with continuous laser exposure with the above used laser power of $\sim$ 30 μW at RT. Observing the change in the peak ratios at -568 cm^{-1} and 570 cm^{-1} which are assigned to the CS-stretch and should be uniformly enhanced and abundant in signal in both inelastic Raman scattering modes.[37] A slight shift in the peaks is attributed to vibrational pumping during surface enhancement as suggested by Etchegoin *et al.* after investigating the change of AS/S ratios of pyridin during SERS experiments.[163] Figure 4.10 shows the spectrum at time point zero minutes. One spectrum is the average of 10 spectra acquired at the previously used Raman conditions every 10 min. The AS/S ratio ρ is related to temperature over the dependence of vibrational populations for AS Raman scattering and follows the relation described in 4.1. The AS/S ratios at each time point are varying slightly around ρ=0.09 but can be considered as the same when looking at the single standard deviations in each measurement (Figure 4.10). This confirms that when using a laser power of 30 μW no local heating of the particle/aggregate environment occurs.

4.1.6 Intracellular SERS on NS-GFA: proving the ability of spectral acquisition

Intracellular measurements were conducted to proof if it is possible to detect the folded aptamer in an intracellular environment. For this NS were functionalised in solution with the stacked G-quadruplex forming aptamer and MCH as described in

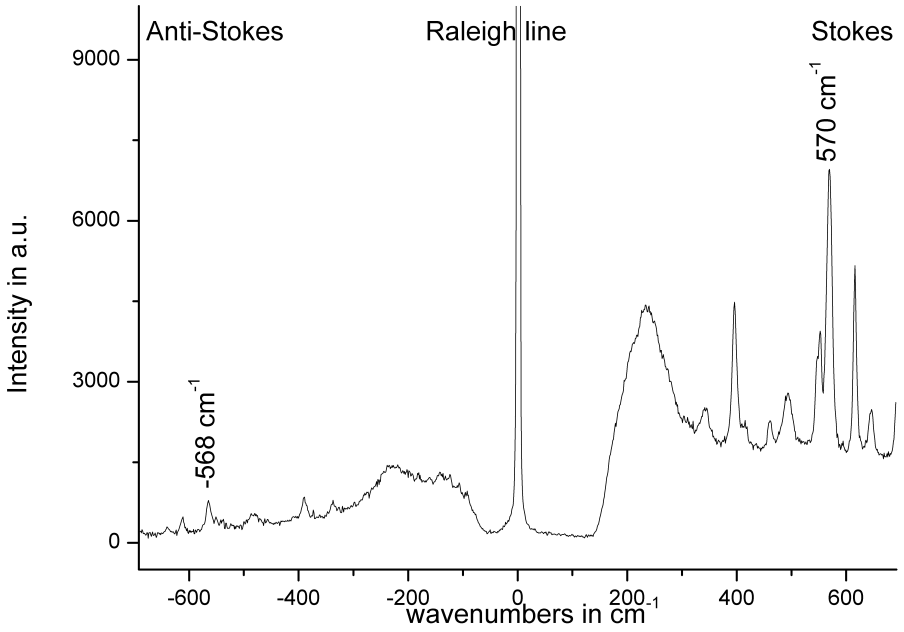

a

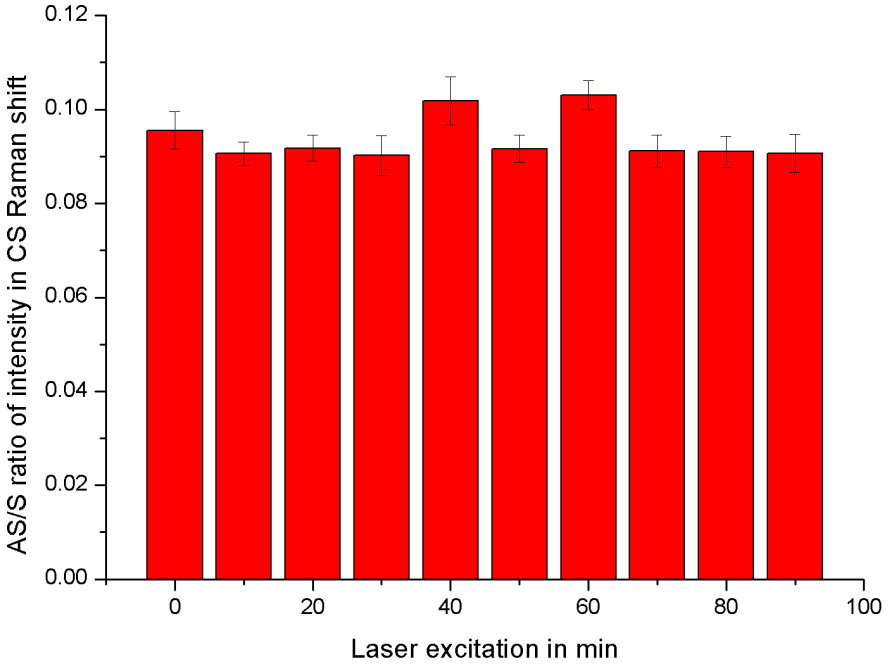

b

FIGURE 4.10: a) Representative spectrum from Anti-stokes / Stokes scattering experiment for the investigation of particle heating. b) Comparison of the calculated AS/S ratio for the integrals of the peaks at -568 cm^{-1} and 570 cm^{-1} respectively.Errorbars show one single standard deviation of the integrals of 10 spectra

section 2.3 and NIH/3T3 fibroblasts were incubated and prepared for spectroscopy as described. In Figure 4.11 the spectrum shows a representative spectrum of this experiment which is very similar to the folded GFA on the NS-aggregate platform on glasslides. The overall Raman feature profile appears to be the same. The only observed differences between intracellular NS-GFA as shown and the glass slide fixated NS-GFA in Figure 4.8 is the increase of intensity of the two peaks at 1200 cm^{-1} and 1256 cm^{-1} as well as the combination of the stretches at 1480 cm^{-1} and 1560 cm^{-1} to one feature at 1515 cm^{-1}. These kind of changes could be explained by environmental differences inside the cell as for example pH and redox potential leading to different protonation or redox states. Furthermore, no indication of unspecific interaction between intracellular compounds or organelles in the spectrum can be found in the spectrum which would probably present themselves in the appearance of novel Raman features. Therefore we can assume that we are still able to detect the characteristic signal for the folded stacked G-quadruplex even in the complex intracellular environment.

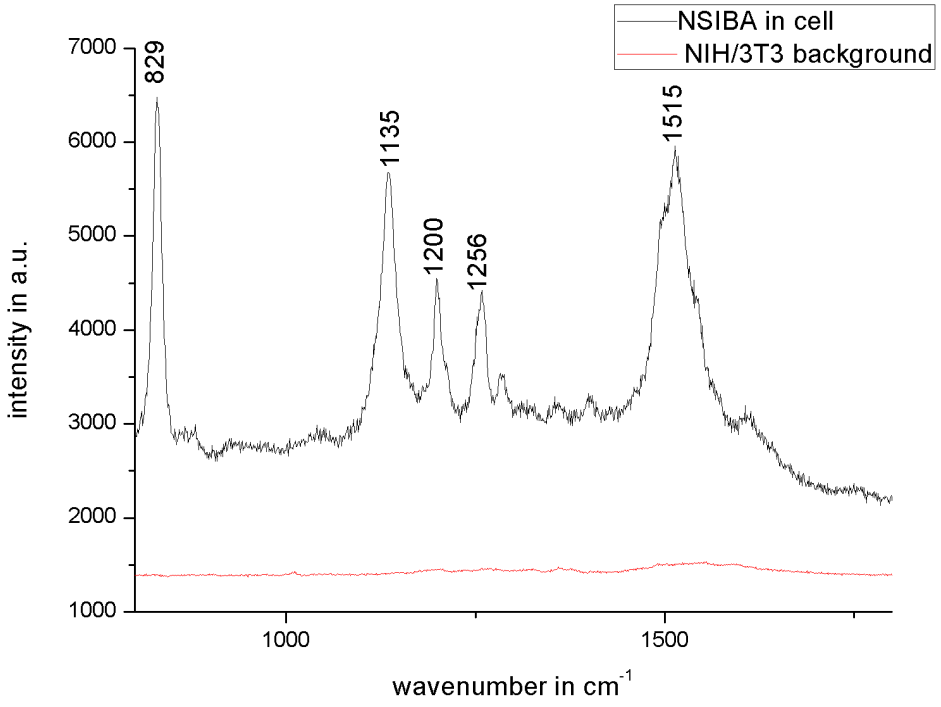

FIGURE 4.11: Graph shows the spectrum of NS-GFA inside a NIH/3T3 fibroblast cell after 3h incubation in serum free media. The acclaimed G-quadruplex characteristic signal is still visible and no sign for unspecific interaction with intracellular compounds can be found in the spectra.

4.2 Peptide based approach for protease sensing

4.2.1 Introduction

While aptamers prove useful for detecting proteins in well characterized *in vitro* environments their sensitivity to cation concentrations may impose mutations *in vivo*. Another possible approach is to use peptides which are specific for one particular protease which is active during a certain cellular response. Proteins, antibodies and peptides already have been investigated for their SERS signal clarifying its application for structure determination, conformation changes during binding and characteristic signal, respectively.[164–166] Here we demonstrate the use of a signal peptide of collagen (α3(IV)NC1) which is the cause of the autoimmune response of T-Cells in Goodpasture's syndrome and quickly digested during inflammatory processes by the protease cathepsin D. The normal secondary structure of the peptide (α3(IV)NC1) possesses a disulfide bridge which stabilizes the peptide in a finger like conformation. Only after reduction of the disulfide bridge cathepsin D is able to bind to and digest this peptide efficiently to render it harmless as an auto-antigen. Using this information the following describes the development of a sensor for the detection of redox potential changes and the detection of the specific protease Cathepsin D.

4.2.2 Nanoshells functionalized with AS35 - synthetic analog of α3(IV)NC1

4.2.2.1 Different approaches for gold surface functionalization

As with the oligonucleotides, we first had to find the best way of NS surface functionalization. In the case of oligonucleotides a first assessment of the modification "quality" was possible by XPS. In the case of peptides this is not possible as no characteristic binding energies can be observed (e.g. of Phosphate), with good enough contrast to the background. Thus, a direct characterization by Raman spectroscopical means had to be pursued. The different methods of functionalization are described in the Methods and Materials sections and an overview shown

in Table 4.2. Figure 4.12a shows the comparison of the diagonal crosscorrelation coefficient of these reactions, which is calculated by the Pearson equation 2.2 and gives a means of estimating the reproducibility[165] of a set of spectra by correlating the variances between every point in all the spectra of one data set and taking the mean as the final value. To do this kind of assessment is need for SER spectroscopy as it suffers from spectral blinking and great variability when the nanoparticle surface is not covered with the probe molecules homogenously. As can be seen the approach in which the AS35 peptide is first modified in a 1:25 ratio with cysteamine (CyA) to obtain a thiol function with following binding to the NS aggregates and incubation with MCH (D1) gives the highest spectral reproducibility. The reactions with a crosscorrelation range between 0.45 and 0.7 (Fig. 4.12a) were not considered as useful for further experiments, as such a low reproducibility does not lead to spectra which can be analyzed. It was assumed that the method D1, consisting of 4 steps, to be the best method of functionalization and is from here on used in the all further experiments. Spectra of NS-CyAAS35-MCH taken of NS aggregates on APTES glass slides are shown in Figure 4.12b. The spectra have a Γ factor of 0.92.

TABLE 4.2: Different reactions for the thiol modification of AS35 and functionalization of NS with resulting molecules and surface protections with 10 mM MCH

	Step1	Step2	Step3	Step4
A1	NS + CyA	+ EDC + AS35		
A2	NS + MPA	+ EDC + AS35		
B1	NS + CyA	+ EDC + AS35	+ MCH	
C1	CyA + AS35 (1:25) + EDC	+ NS	+ MCH	
D1	CyA + AS35 (1:25) + EDC	purification	+ NS	+ MCH

4.2.3 Redox potential dependent spectral changes

Intracellular redox conditions are controlled by the different ubiquitous redox pairs, like glutathione, thioredoxin and hydrogen peroxide covering a redox potential range between 0 and -400mV intracellular and is adjusted by ratios between these

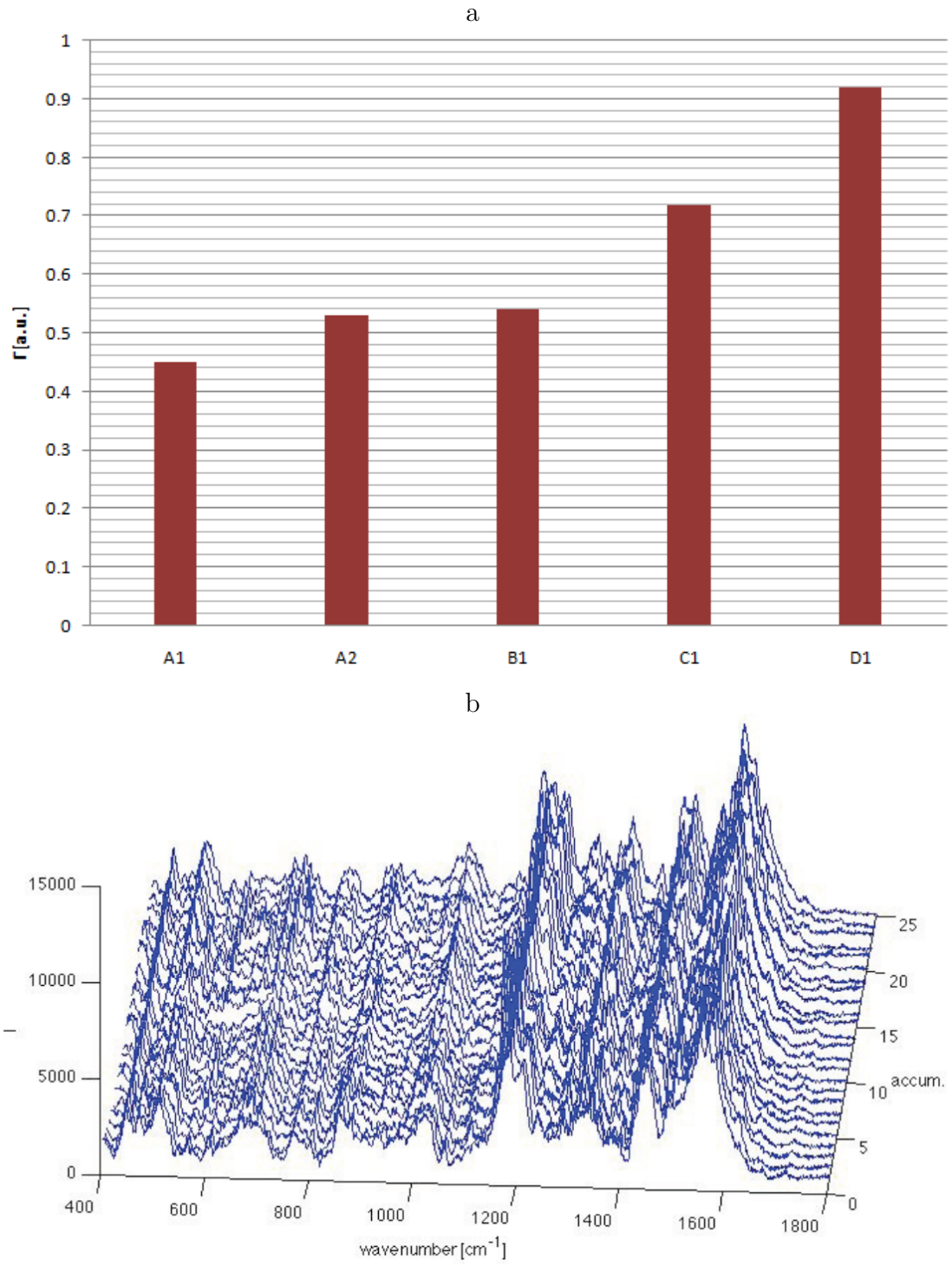

FIGURE 4.12: a) Diagonal crosscorrelation coefficients for the different NS modification approaches as described in Table 4.2. b) Set of 25 spectra showing the high reproducibility of the SERS spectra after resulting in a Γ factor of 0.92 by using modification approach D1

redox couples.[167] The Nernst equation (4.2) supplies a convenient way of calculating these ratio considering the environmental influences like, temperature and surrounding pH. Herein the standard potential ΔE° covers the changes in pH and the term $\frac{RT}{F}$ deviations from the standard temperature. The logarithm to the base of ten of the oxidized to the the reduced form of the redox-pair results in the determining factor at certain conditions. Glutathione is distributed over the cell in concentrations between 1-11 mM and effects the reduction of SH/SS bonds.

As mentioned in the introduction the Goodpasture's syndrome "activating" peptide (α3(IV)NC1) contains in its oxidized form a disulfide bond folding/stabilizing it into a hairpin or finger like conformation which makes it inaccessible for the endo-protease cathepsin D. Reduction of this disulfide bond leads to the opening and linearisation of the peptide and makes it digestible. To investigate the behavior of the peptide at different potentials with SERS a screen between -100 mV and -300 mV(which is the most significant redox potential range for the GSH/GSSG couple) was conducted. This should elucidate the potential necessary for conformational changes of the peptide and help the prediction of unfolding/linearisation. From the Nernst equation the GSH/GSSG ratios for -100, -160, -180, -200, -220, -240, -260, -300 mV were calculated taking into account a pH of 3.2 (optimum for cathepsin D activity) and 25 °C (Table 4.3). In this and all the following experiments the GSH concentration was kept constant at 10 mM, which is on the upper margin of the intracellular possible concentration. The freshly prepared solutions in pH 3.2 buffer were placed on the sensing spots and left 10 min for equilibration before taking 25 spectra as described in the Material and Methods section. The data was than background corrected and averaged. Figure 4.13 shows the averages of 25 spectra acquired of one spot over a range of potentials. No real trend, eg. the continuous change in a set of features transforming into an other shift could be found. This suggested that we do not observe a change between rigid discreet states of the peptide but rather between states of different flexibility/orientation. Furthermore it can be suspected that the redox potential has direct influence on the conformations of the molecules of interest and therefore position on the nanostructured surface which can be deduced from the findings of Podstawka *et al.* [2010], who showed that the orientation and adsorption of aromatic molecules is dependent on the applied potential.[168] In the case of a

$$\Delta E = \Delta E^{\circ} - \frac{RT}{nF} ln(\frac{[RED]}{[OXI]}) \tag{4.2}$$

ΔE	Redox potential
ΔE°	Standard potential
R	Ideal gas constant
T	Temperature in Kelvin
F	Faraday constant
n	Number of electrons

change in flexibility, we might expect to see spectral changes at the "breaking potential" of the internal disulfide bond. This would lead to an increase in molecular freedom and therefore in a decrease in spectral reproducibility. Similarly to the experiment leading to finding the best method of functionalization, a means of depicting differences between different potentials is the pearson cross-correlation factor Γ. Γ describes the variability between spectra and therefore allows us to study flexibility changes at different potentials. Figure 4.14 shows the result of the calculation of Γ at different potentials ranging from 0 mV to -300mV. The most distinct change in the Γ can be observed as Γ drops from 0.89 at -180 mV to Γ=0.58 at -200 mV. After this point a steady increase in Γ can be found leading to a high congruence between spectra with a factor of 0.97. This suggests that we observe with the drop in spectral reproducibility the first partly reversible opening of the peptide secondary structure at around -200mV. This depicts the equilibrium between the open/closed conformation. A further increase in potential shifts the equilibrium towards the reduced sulfides expressed in a steady increase in spectral reproducibility up to an apparent endpoint at -300 mV, where the set of observed peptides are most probably uniformly ordered in their open form. As described above, the linearized form of the peptide is necessary for the aspartyl protease cathepsin D to bind to and to cut the restriction sites. Therefore follows in the next section the experiments investigating the digestion of the peptide by cathepsin D at different potentials.

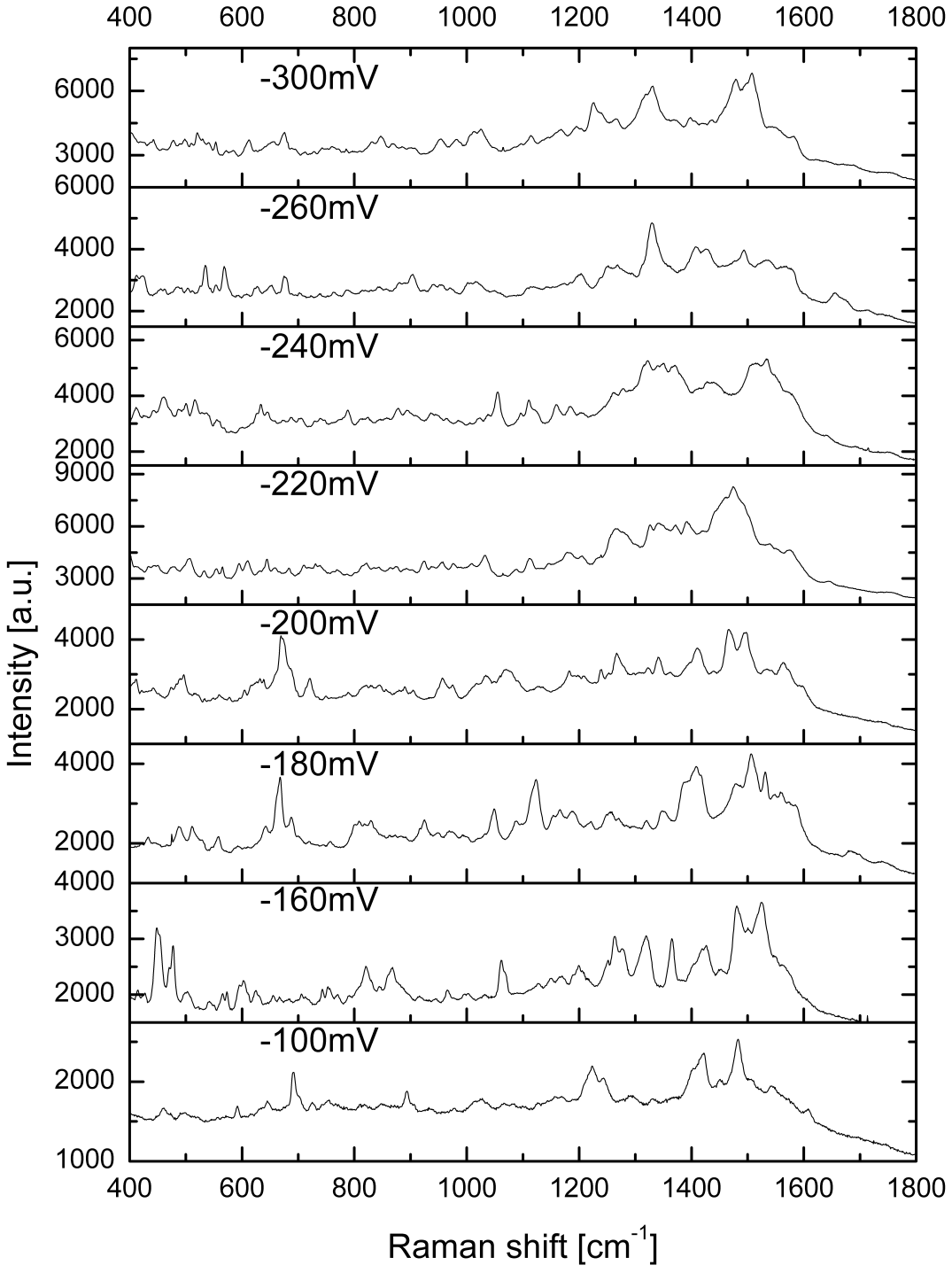

FIGURE 4.13: Averages of 25 Raman spectra obtained at different GSH/GSSG ratio adjusted redox potentials from -100 to -300 mV bottom to top in pH 3.2 buffer at RT.

TABLE 4.3: Ratios between GSH at 10 mM and GSSG

ΔE in mV	Ratio	[GSSG] in M
-100	7.28E+04	1.37E-07
-160	7.81E+06	1.28E-09
-180	3.71E+07	2.69E-10
-200	1.76E+08	5.67E-11
-220	8.38E+08	1.19E-11
-240	3.98E+09	2.51E-12
-260	1.89E+10	5.29E-13
-300	4.27E+11	2.34E-14

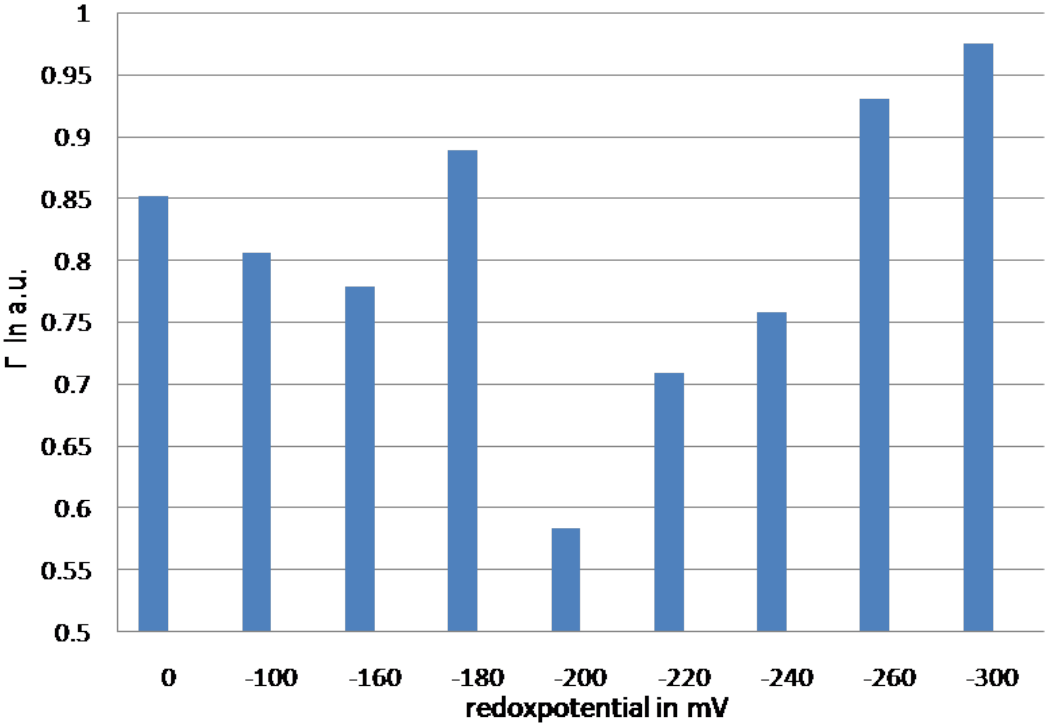

FIGURE 4.14: Diagonal Cross correlation factor calculated with Pearson function correlating the 25 spectra for the above shown potentials from -100 to -300 mV.

4.2.4 Raman spectroscopic evidence of α3(IV)NC1 digestion with cathepsin D

The above investigation of the spectral behavior of the NS-AS35 peptide SERS setup regarding its redox potential changes suggests that the conformation of the

nanoparticle surface bound peptide is changes at redox potentials higher than -180mV to -200 mV. Confirmation of this finding can be carried out by digestion with the protease cathepsin D which is only able to digest the reduced form. Therefore the following section reports an experiment examining a digestion of the reduced peptide, the protease activity at different redox potentials and the prediction of the leftover peptide fragment on the particle surface by SERS.

4.2.4.1 Spectral depiction with the help of an AA library

Raman spectra are not easily comparable even on a daily basis working on one setup, as calibration and slight alignment differences lead to changes in Raman shift and intensity. This is even more true in the case of SERS which is influenced, by the nanostructured substrates, their material and in the case of particles their aggregation behavior. This makes it hard to compare spectra from the literature with acquired results to produce meaningful assignments. In this work it was thus decided to employ a Raman library of the single amino-acids (AA) found in the α3(IV)NC1 peptide analog AS35 with the sequence. Therefore the employed nanoparticles, Auroshell^{TM} nanoparticles, aggregated on APTES glass slide, as described above, were modified with C-terminal thiol modified homopeptides of each AA. The homopeptides (length ~3-5 AA) were synthesized and modified as described in the Materials and Methods section out of the mono-amino-acids (Sigma). The rationale for the use of homopeptides was to simulate the freedom of the target peptide and to acquire the Raman modes for every possible vibration in the molecule as a higher degree of freedom allows the molecule to orientate in different ways towards the surface plasmons evanescent wave as was described by Wei *et al.*.[165] For spectral acquisition the exact same conditions as for the Raman experiments on the NS-AS35 setup were employed (50 μW, 10 s at pH 3.2). The collection of averaged and baseline corrected AA spectra can be found in Figure 4.15. All the spectra show distinct differences as expected with mostly strong signal in the fingerprint region between 1000 cm^{-1} and 1800 cm^{-1}. To strengthen the argument that a library like this is necessary we should have a look at the spectrum of the aromatic AA phenylalanine. The ring-stretching vibrations

at 1000 cm^{-1} and 1039 cm^{-1} of Phenylalanine possess very high Raman cross-sections and are normally obtained as the strongest and sharpest features in bulk Raman spectra of Phe and even in spectra acquired of whole organisms. But in the obtained spectra in Figure 4.15 these features are relatively weak. This is likely to be caused by the orientation of the molecule towards the enhancing surface as also reported by Ozaki *et al.* [2005], who investigated Phe and other AA adsorbed on gold and silver nanoparticles and obtained similar weak intensities of these stretches.[169] For a SERS experiment this means that it is crucial to acquire spectral data for every element of the sensing platform as the used nanostructures and the molecules itself have influence on the obtainable Raman shifts. In the following part of this work the AA spectra will be used for analysis of experimental data by taking the derivatives of the spectra and constructing the peptide Raman spectrum for the peptide of interest *in silico*.

4.2.4.2 Analysis of spectral data

To compare data of the acquired spectra in all further experiments with the AA library and the constructed peptides the first derivative of the spectra were calculated after averaging and background substraction and correlated with the Spearman correlation coefficient function in Equation 4.3 with the model Raman spectra. Spearman rank correlation is used in this case as the Pearson correlations lead to no congruence in the data. This correlation is preferably used for curved data with quickly changing data points and has a level of significance of the two tailed test of 0.01.[170] The calculated values give than information about how well the measured data of the following experiments corresponds to the model spectra constructed out of the AA library.

$$\rho = 1 - \frac{6 \sum d_i^2}{n(n^2 - 1)} \tag{4.3}$$

ρ Spearman Rank correlation
d_i difference between the ranks of corresponding values y_i and x_i
n number of values in each data set

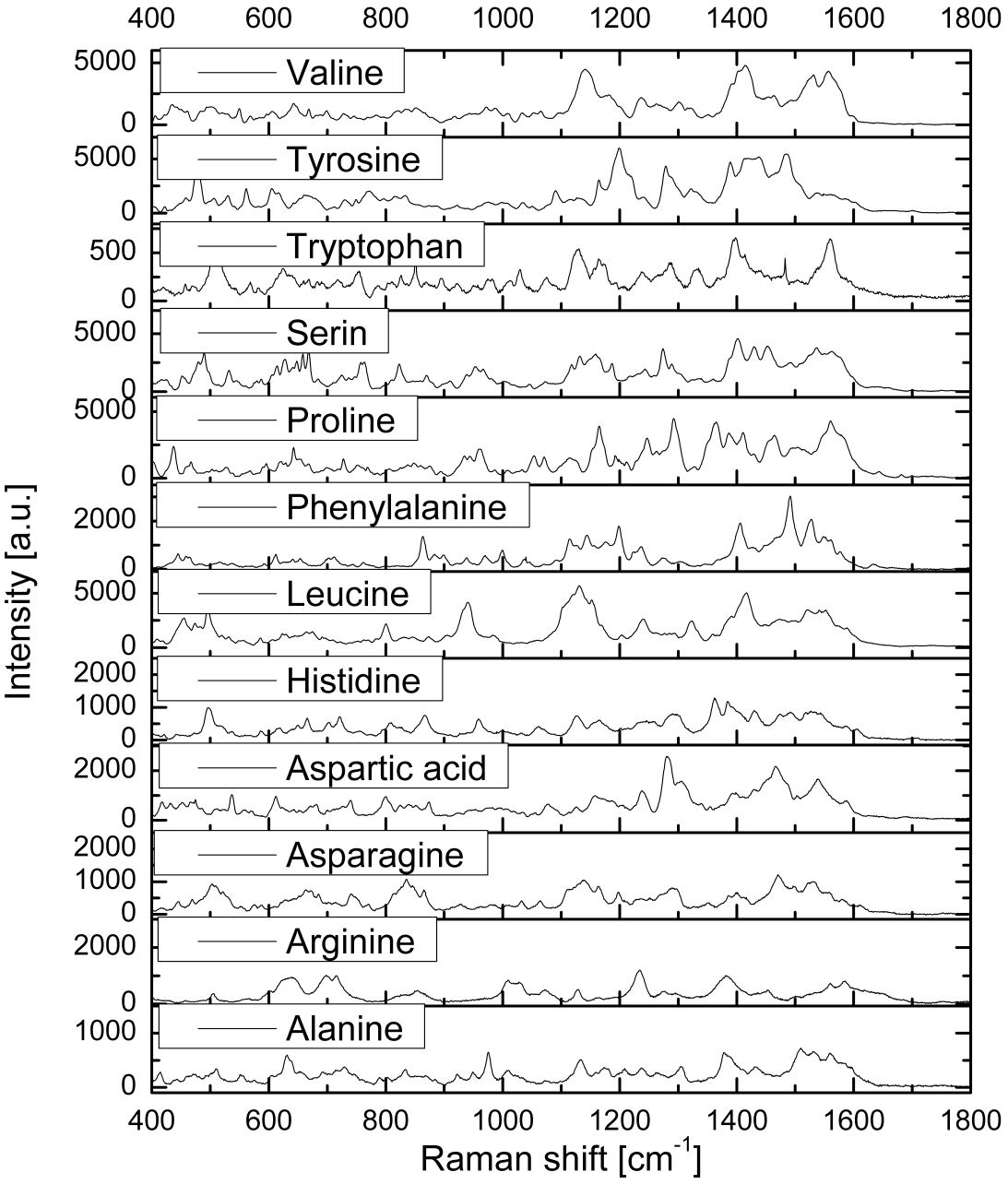

FIGURE 4.15: Spectra of the amino-acids Alanine, Arginine, Asparagine, Aspartic acid, Histidine, Leucine, Phenylalanine, Proline, Serine, Tryptophan, Tyrosine and Valine obtained as reference Raman library for analysis of peptide Raman spectra.

4.2.4.3 Digestion of Nanoshell bound peptide with cathepsin D

For initial digestion experiments a redox-potential of -250 mV was chosen, which is well above the empirically limit for promoting conformational changes of the AS35 peptide. To allow for the highest activity of the protease the temperature was adjusted to 37 °C with a homemade heatable stage connected to a waterbath for warming the slide during measurements at a pH of 3.2 in a 50 mM sodium acetic acid containing buffer. AS35 functionalized NS aggregates were first incubated for ten minutes with buffer at a redox potential of -250 mV and spectra acquired before and after incubation with 1 U of cathepsin D from human liver at same buffer conditions over one hour. After one hour the sensor aggregates were washed with 1 M acetic acid for protease denaturation and copious amount of buffer at pH 3.2 before another Raman acquisition was conducted. In Figure 4.16 the acquired data for this experiment shows an evident difference between the measurement before and after the incubation with the protease, expressed best with the integral under the curves. A 70 % decrease in overall signal is observed suggesting a very efficient digestion of AS35 on the NS surface. Therefore we can safely assume that at -250 mV we are observing the open form of the peptide. Further studies to elucidate the influence of different redox potentials will give information if we are actually observing the opening of the peptide or if the digestion is unspecific to different potentials. In the same graph the data for the average spectrum of the sensor after 1 h incubation with cathepsin D and before denaturation and wash is shown. Very distinct features at 540 cm^{-1}, 1249 cm^{-1} and 1500 cm^{-1} appear as well as an overall increase in signal intensities of features already visible in the spectra of the peptide at -250 mV. The appearance of these new features will be discussed further in the next section.

4.2.4.4 Dependence of redox potential on the digest with cathepsin D

To conclude the question of whether an actual change in the peptide conformation with cleavage of the internal S-S bond in AS35 is observed a similar digestion experiment as above was performed at two different potentials at opposite ends of the used redox potential range. Two spots with AS35 modified NS aggregates

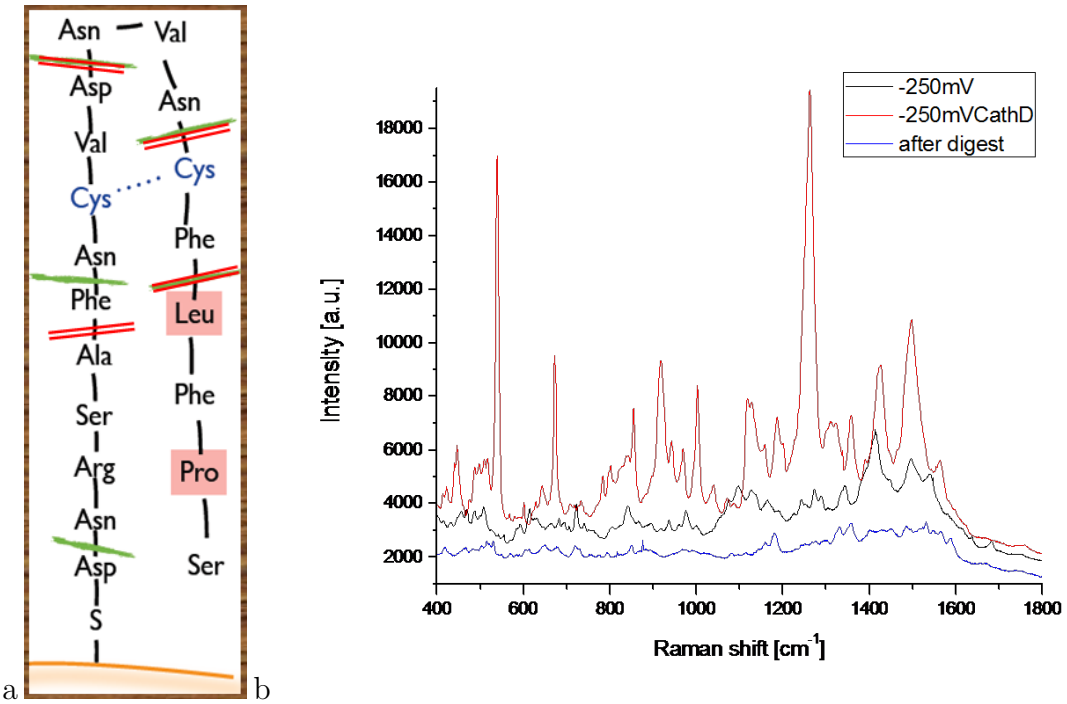

FIGURE 4.16: a) Sketch showing the closed form of the peptide bound the NS surface with main restriction sites in red and minor ones in green. b) Average of 25 spectra of digestion experiment with cathepsin D at -250 mV. Shown spectra are after preincubation with buffer at -250 mV, after the incubation with cathepsin D and after incubation, denaturation and wash of the sensor.

were pre-incubated for this with buffer at a GSH/GSSG controlled potential of -100 mV and -300 mV before a digest was conducted at the same potentials over 30 mins on freshly prepared and separate sensing spots. The spectra taken at -100 mV are very similar, although showing slight differences in Raman shifts, but still have the same overall intensity (Figure 4.17a). In the comparison of spectra before (black) and after (red) in Figure 4.17b only the measurements at a redox potential of -300 mV display a distinct decrease in signal after the incubation with a reduction of the integral under the curve to ∼30% of its initial value. Thereby we can confirm that the opening of the disulfide bond is and the unfolding of the α3(IV)NC1 peptide analog AS35 is redox dependent and necessary to allow digestion by the aspartyl protease cathepsin D.

a

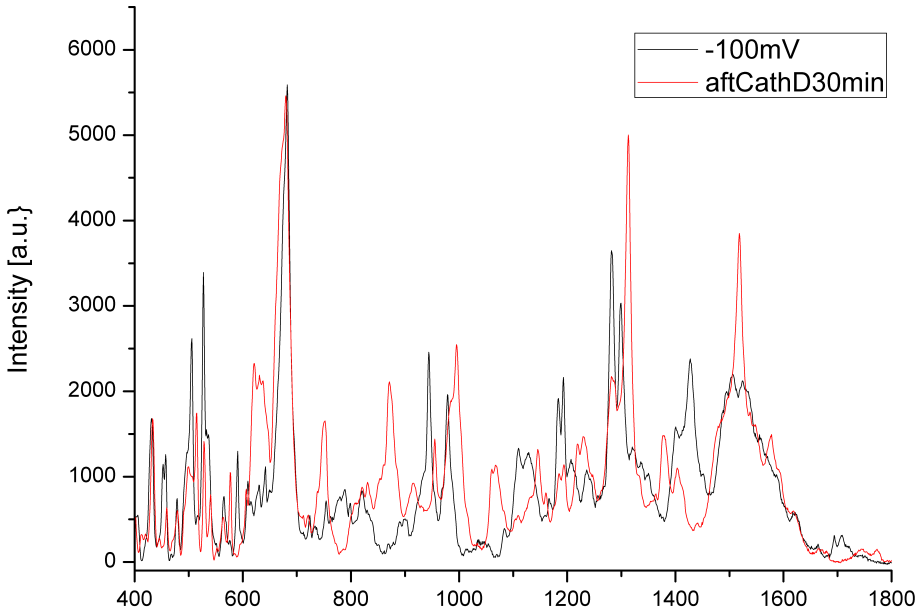

b

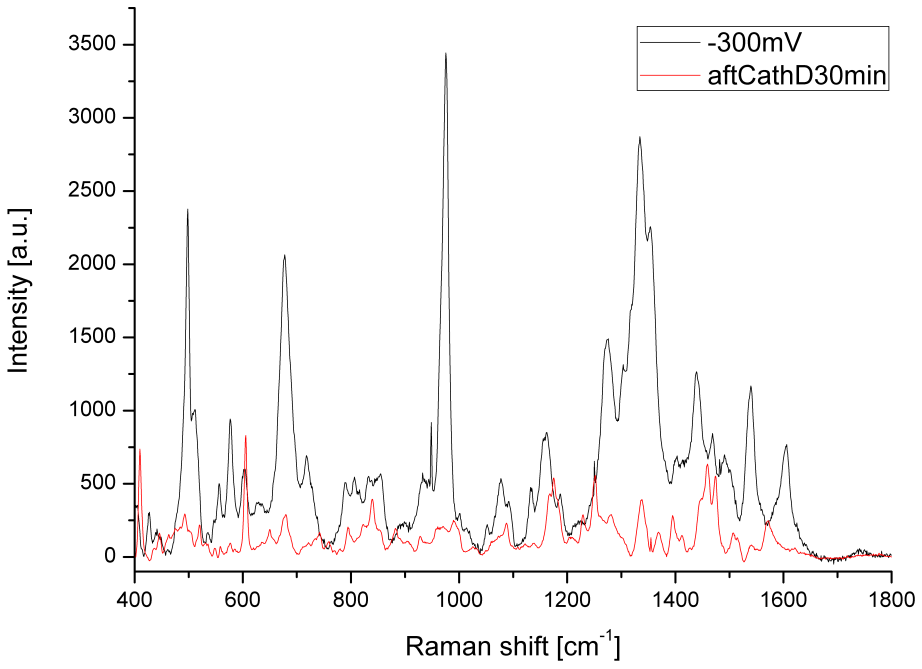

FIGURE 4.17: Digestion experiment with cathepsin D at -100 mV and -300 mV.All spectra were recorded at the stated potential either before or after cathepsin D treatment. Spectra are averages of 25 acquisitions.

4.2.4.5 Prediction of Restriction sites by the AA library

While the data in section 4.2 gives quantitative information about the peptide cleavage, it does not give any structural or chemical information. Raman spectroscopical data of biological systems is in general so complex and hard to predict, either by computational means or comparison to literature values, that this can be seen as a major drawback of this technique. In the following section it is shown that in the case of a peptide chain, a library consisting of its building blocks (the amino-acids) can be used to to predict its spectrum or to workout the constituents of a peptide on the basis of its spectrum.

The normalized spectra of the as described AA homopeptide library were then used to reconstruct the spectrum of the whole peptide to find the best fit with the fragment left on the NS surface after the digest with cathepsin D. Figure 4.18 compares the experimentally measured spectrum of the digested peptide, at -250 mV with 1 U of cathepsin D after one hour at 37 °C, with the Raman model obtained from the AA library for the surface bound possible fragments Asp-Asn-Arg-Ser-Ala (DNRSA) and Asp-Asn-Arg-Ser-Ala-Phe (DNRSAF). The reason for focusing on these fragments is that this is the location of the closest cleavage site for cathepsin D.[84] The first remarkable observation here is that both the spectra DNRSA and DNRSAF show many similarities with the Raman features of the measured spectrum, for example between 440 cm^{-1} and 560 cm^{-1}. The similarity is such that for example in the range between 600 cm^{-1} and 700 cm^{-1}, peak positions and intensities match between the experimental and the model data. Furthermore when comparing the spectra of the model peptides with the experimental some features can be found which are represented in the longer one with the phenylalanine at the end, but not the one up to the alanine. Examples for this are the features at 1220 cm^{-1} and 1540 cm^{-1}, which can be assigned to the aromatic ring stretches of the Phe.[171, 172] On the other hand other features, like at 1330 cm^{-1}, which can neither be found in the constructed spectra and therefore seem to be characteristic for a molecular vibration not able to simulate by the Raman library.

To analyse Raman spectra one by one is rather laborious and time consuming work which is also prone to human bias. Therefore it is in many cases better to

work with automatic correlations by statistical functions. Correlation by direct comparison between every possible peptide fragment model and the experimental data should give a value which makes it possible to determine length of the residual AA chain. As described above a possibility to normalize Raman spectroscopic data, especially SERS data, is to use the first derivative, resulting in an output representing the peaks and the rate of their in-/decline and automatically decreasing the background. When using the spearman correlation to compare the digest with all the possible models, there is an increase of the correlation factor up to the point of the first Phe as seen in Figure 4.18b. Correlations between further models further than Phe drops in a manner which appears congruent with possible cleavage sites of cathepsin D.[84] This confirms with high confidence that we can observe the digestion of a gold surface bound peptide by cathepsin D and also gives an indication between different cleavage sites and the shortest possible fragments. For comparison 4.18b also shows the correlation between model peptides and the spectra for complete and folded AS35 peptide after the digestion experiment at -100 mV. Here we observe a continuous increase in correlation between model spectra and measurement up to the point where the bend in the peptide could be predicted with slight decrease in the correlation factor after this point. This might be caused by some digestion at the N-terminal end.

a

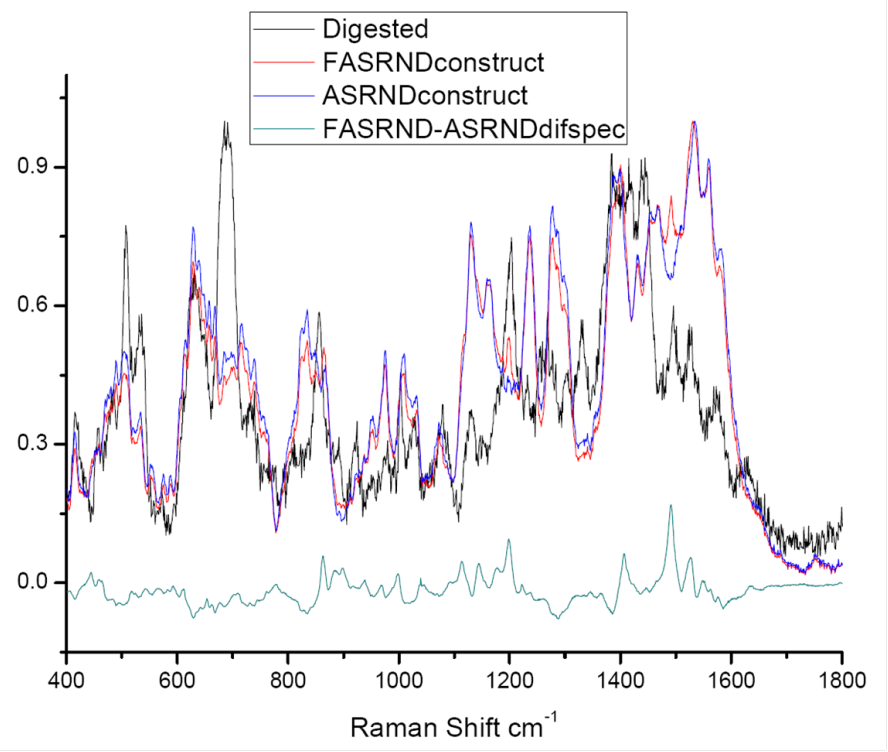

b

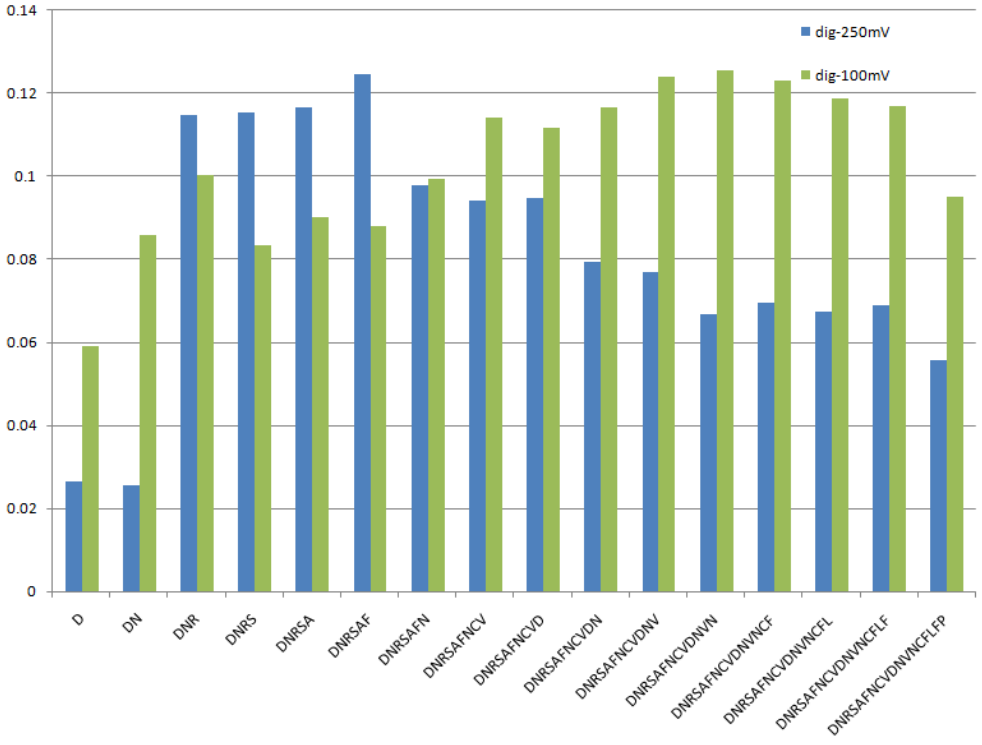

FIGURE 4.18: a) Spectral comparison between constructed peptides DNRSA and DNRSAF and the Spectrum acquired after digest at -250 mV, inclusive the difference spectrum between the models DNRSAF-DNRSA. b) Spearman Cross-correlation comparison between constructed peptides of AS35 up to Proline and the same digestion experiment.

4.2.5 Detection of cathepsin D binding on NS-AS35

As already shown, it was possible to gain information about the redox dependence of the conformational changes of the the peptide and also its digest with cathepsin D. Another very exciting finding is, as we were able to observe in the digestion experiment shown in Figure 4.16 a strong signal increase at distinct Raman shifts which could be attributed to binding of cathepsin D to the residual peptide on the gold particle surface. This suggests that while cathepsin D, is able to bind to the peptide it is not able to cleave this close to the surface. The protease seems to be bound at this point as this signal can be found after 30 min incubations with cathepsin D, but only bound weakly as the signal is lost after a simple wash with buffer and does not make a denaturation of the protease with 1 M acetic acid necessary. Figure 4.19a shows once more the Raman signal after incubation and Figure 4.19b the crystal structure of the binding site of the protein. The active site is reported to be especially deep and flanked by aromatic amino-acids, like phenylalanine and tyrosine. An assignment of the extremely strong feature at 1258 cm^{-1} and strong and sharp features at 670 cm^{-1}, 854 cm^{-1}, 1002 cm^{-1} or 1425 cm^{-1} in the "bound" correlates well with the spectra of Tyr and Phe (Figure 4.19b).[165, 171, 173] Other signal increased features seem to be further enhanced like the stretch at 1498 cm^{-1}, which although also a Phe stretch can already be found in the peptide spectrum. This suggests that in addition to measurement of peptide structure and digestion, NS-AS35 can be used as a detector for cathepsin D

4.2.6 Detection of MCF7 breast cancer over-expressed cathepsin D - excreted and in living cells

In order to investigate the use of NS-AS35 as a cathepsin D sensor, we used the breast cancer cell line - MCF7. MCF7 cells are known to overexpress the gene for cathepsin D and also affects the transport mechanisms of this protease which is normally only found in or close to the lysosome. Pro-cathepsin D and the active form cathepsin D is in these cells even excreted into the extracellular environment,

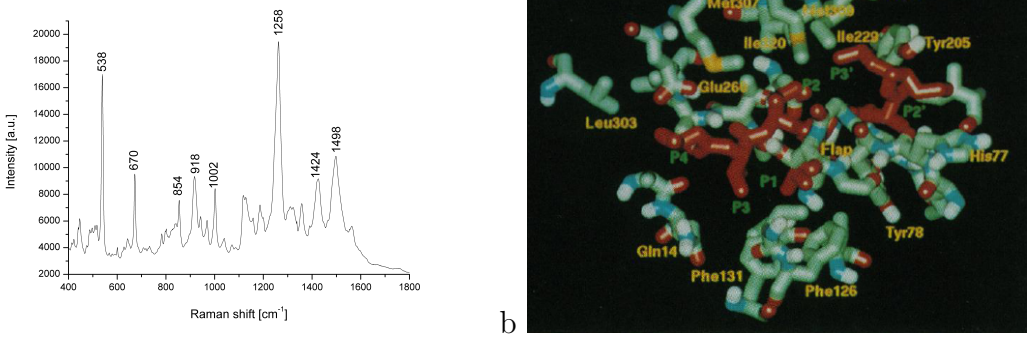

a b

FIGURE 4.19: a) Raman spectrum of cathepsin D bound to NS-AS35 b) Crystal structure of active site of cathepsin D with Phenylalanines and Tyrosines flanking the binding groove.[174]

whereupon Pro-cathepsin D exhibits cell metastasis activity, and therefore is a promising prognostic marker for breast cancer diagnosis.[175]

Therefore it was tested if the low extracellular cathepsin D extracellular levels can be detected with the above reported system, either by observing the digestion of the NS linked AS-35 peptide or the direct detection of Raman shifts which have been observed during the incubation with purified cathepsin D. Therefore acidified supernatant of cultured MCF7 cells also containing 15 % of foetal calf serum was taken and put on a sensor spot after adjusting the redox potential to -300 mV by the GSH/GSSG redox couple. Raman acquisition was conducted as described, before, after 1 h of incubation and after digestion and cleaning of the sensing area. The data shown in Figure 4.20 shows the Raman acquisitions with the expected spectral changes, stronger signal in the beginning and slight decrease after the digest and the characteristic features of the cathepsin D interaction during protease contact time. The integrals of the spectra in Figure 4.20 describe the difference before and after digestion. This proves the general possibility to use NS-AS35 SERS based system for the diagnosis of the breast cancer marker cathepsin D.

Another interesting experiment concluding this project is to give the intracellular detection of cathepsin D which should only be possible in the intracellular environment where the necessary oxidative requirements for the disulfide cleavage preside. It was already clarified that NS can be transferred into lysosomes but also into the cytosol of NIH/3T3 Fibroblast as shown in Chapter 3. Very recently

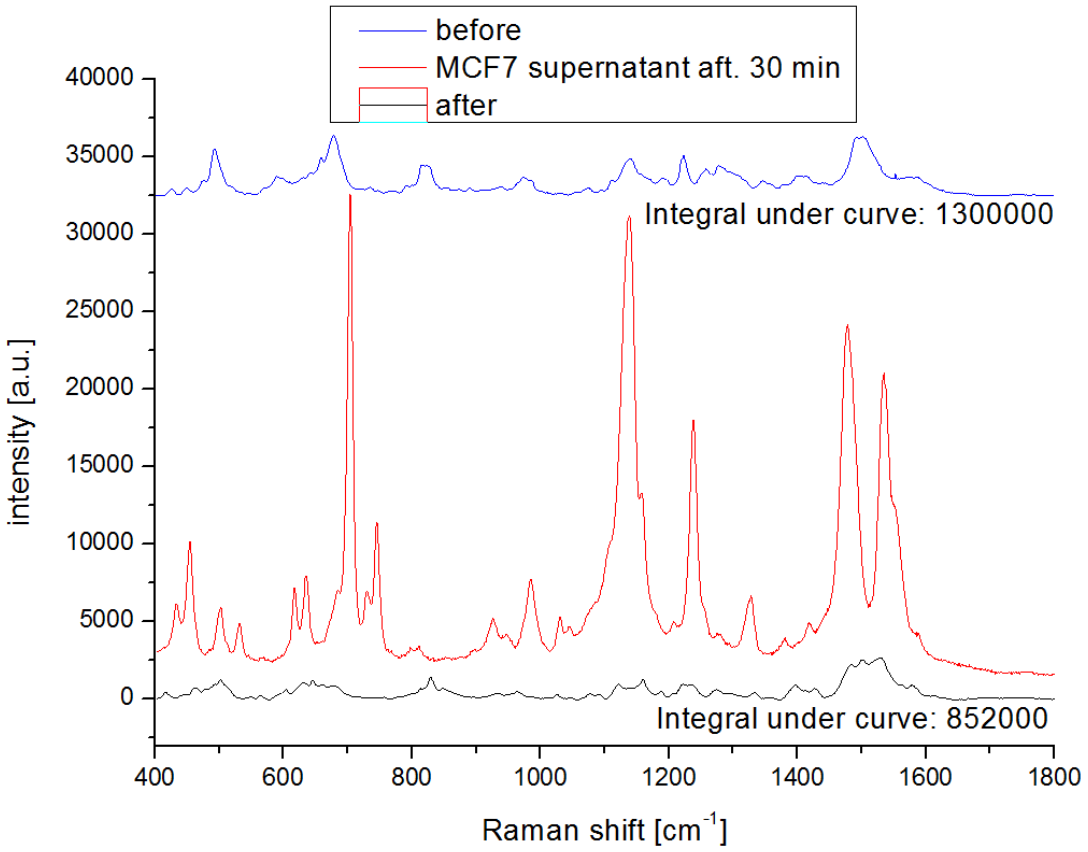

FIGURE 4.20: Spectra of experiment testing the ability to detect cathepsin D in the media of a MCF7 culture. Graphs show the digestion before, during (after 30 min) and after incubation with supernatant. Also comparing the changes in the integrals between starting and endpoint observing the digestion.

it was shown that protein complexed nanoparticle aggregates can be transferred into the cytosol of MCF7 by a similar mechanism as shown in Chapter 3 (Bale *et al.* (2010)) without the involvement of lysosomes.[164] Furthermore in Chapter 3 it was demonstrated that nanoshells can be transferred into cells independent of cellular uptake mechanisms and efficiently by incubating the particles in a serum free media. This allowed entry of naked NS into the cells and direct contact to the cytosolic environment.[118] In this case, the cell incubation experiment NS were modified with the thiol modified HS-AS35 peptide and blocked with MCH. Cells were seeded and grown overnight on quartz 1 mm thick slides then incubated in serum free media at a concentration of 300 fM (corresponds to ∼1000 NS/cell in this incubation) of the NS-AS35 sensor over 1 hour before washing with PBS and transfer into the Raman setup for spectral acquisition. In order to find NS a map,

over a monolayer of MCF7 cells, consisting of 10x10 spectra with a pitch of 5 μm in every direction taken with 10 seconds of acquisition time at each point and a laser power of 0.5 mW with the 785 nM HeNe laser using the same 50x water immersion objective with an NA of 0.8 as as previously described. The spectral range in this experiment was also kept in scanning mode between 400-1800 cm^{-1}.

Of these 100 spectra 3 different kinds of spectral types could be distinguished. The most abundant spectra (67/100) were uniform background spectra with features of the quartz coverslip and background fluorescence of the underlying glass petri dish shown in Figure 4.21a. Spectra with weak features on top of the background signal, as shown in Figure 4.21b, could be found in 27 cases. After background correction and analysis by comparison with the peptide library in the same way as for the digest on the surface bound NS-AS35 aggregates (derivative correlation), it was possible to trace these features back to the peptide as an origin. Furthermore this data (Figure 4.21d) suggests that the acquired signal is actually from a AS35 covered particle, which might be partially digested as can be seen in Figure 4.16c, the comparison with the model peptide. This is a promising result which in principal shows that digestion can be observed intracellular, but has to be investigated and proven in further work. Finally another 6 spectra could be found displaying similar features to the once which have been attributed to the binding of cathepsin D. The spectrum in Figure 4.21d as a representative spectrum shows strong features at the same shifts, as for example the Tyrosine ring breathing mode at $\sim$1250 cm^{-1}.

Overall this result suggests that we could observe the activity of cathepsin D in the breast cancer cell line MCF7, e.g. the digestion of the peptide in the same way as on the array and also can evaluate the signal of the digested peptide and its fragments still attached to the nanoparticle. Also the detection of the protease of interest is intracellularly possible and can be specifically interpreted and assigned.

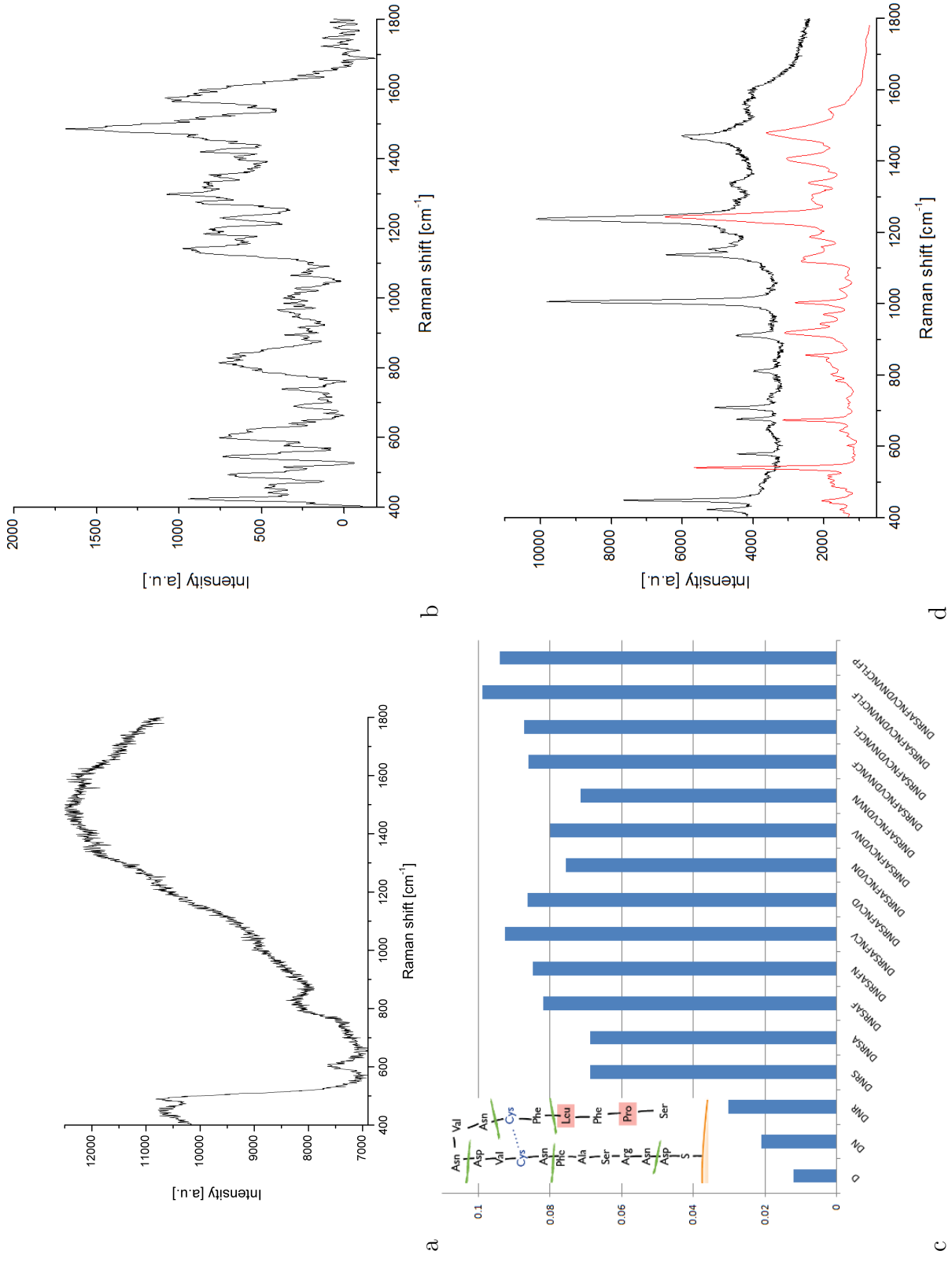

FIGURE 4.21: a) One of 67 background spectra of experiment with MCF7 cells b) Spectrum of NS-AS35 found intracellular c) Crosscorrelation spectrum in b) to determine the grade of digestion d) One of 6 spectra showing characteristic signal indicating the presence of cathepsin D. Spectrum in red for comparison overall from Figure 4.19a

4.3 Conclusion Nanoshells for Labelfree protein detection

To realize the goal of protein detection two different approaches were explored. In both methods the NS surface was modified with a biological molecule which binds or interacts with a protein of interest and the applicability of these approaches for intracellular application was assessed.

The first approach used an aptamer. The thrombin binding aptamer was selected because of its secondary structure which is supposed to assume a stacked G-quadruplex conformation on interaction with thrombin and because it is extremely well characterized. Initially the best conditions for the surface functionalization with the 5' thiol modified aptamer were investigated and the condition yielding the highest amount of DNA was studied by XPS. The best results for the gold particle modification were found yield the best cover in a buffer containing 120 mM NaCl, crucial for the formation of the gold-thiol bond, and 10 mM of $MgCl_2$ and KCl which stabilize the stacked G-quadruplex. This buffer was also used for all further *in situ* sensing experiments. Raman investigations of the TBA modified surface have shown that it is necessary to protect the gold surface with mercaptohexanol (MCH) which does not interact with the functional groups of DNA or other surrounding molecules. By forming a mixed monolayer of TBA and MCH it was possible to avoid binding of DNA to the surface therefore making it available for interaction with target protein. The baseline spectrum for the NS-TBA sensor shows only very weak signal with the most prominent peak at 1090 cm^{-1} being assignable as the PO_2 stretch. Since the intensity of this peaks is relatively invariant, it was used as an internal standard. Incubating the modified NS with human α thrombin led to spectral changes which have been assigned to certain DNA stretches. The appearance of this DNA related strong signal is due to the assembly of the stacked G-quadruplex structure on target interaction. The strong enhancement can be explained by the interaction between the stacked Guanosin-DNA bases orientated perfectly towards the surface plasmon of the nanoparticle surface. This signal can be reliably observed down to a concentration of 50 aM. The limit of detection for the sensor lies at 0.1 fM.

Theoretically single molecule detection should be possible with this approach. The incubation of the protein sensing platform with other proteins like trypsin, insulin, serum albumin or even a human serum didn't provide similar signals. Therefore this platform can be deemed to be a very sensitive sensor for the detection of proteins.

A melting experiment in which the spectral changes during the heating of the sensor platform was observed. This showed that the signal is actually formed by the structural changes due to stacked G-quadruplex formation. Here a similar aptamer which was selected for its stacked G-quadruplex secondary structure was used. The insulin binding aptamer (IBA) was also fixed to the NS surface with a 5' thiol modification. But when Raman measurements were conducted the signals which previously were assigned to the stacked DNA complex, appeared in the spectra in the binding buffer without the target protein. Therefore it seems that depending on the G-quadruplex forming aptamer certain buffer conditions have to be found to prevent self-folding as in the case of TBA which only forms during target binding in the employed buffer conditions. But this finding made a different observation possible. As it was not clear to this point if the strong Raman signals were induced by the DNA secondary structure formation. Melting slowly decreased the signal at a temperature above 40 °C but recovery of the characteristic signal was reached again after cooling to RT. Further application of the IBA for protein sensing was not investigated as a utilization of G-quadruplex aptamer was not a viable approach for the intracellular application due to the dependence on the surrounding environment. Nonetheless, this has great potential for the SERS mediated sensing of proteins *in situ* on microarrays, can be controlled. In a proof-of-principle experiment the self-folding NS-IBA was internalized into cells and it was possible to acquire Raman spectra from the folded G-quadruplex aptamer from inside cells, but without the interaction with a target protein, showing that the aptamer secondary structure is also stable inside cells.

The second approach investigated involves the peptide a3(IV)N1 which plays a role during signaling events in the fatal autoimmune disease Goodpasture's syndrome, in which kidney and lung cells are attacked by T-Cells. In order to study the peptide, which is preferably forming a finger like closed secondary structure containing a disulfide bond stabilizing this confirmation we assembled the peptide on

the surface of NS. The best way of modifying the sensing surface was investigated, by analysing the highest reproducibility in Raman spectra, therefore showing the best conformity on the gold particle surface. Reacting the C-terminal end of the peptide with cysteamine in high excess, providing a thiol function, was found to yield the best results. Here again it was important to form a mixed monolayer of the peptide with MCH to prohibit nonspecific interaction of the rest of the peptide with the surface. The peptide modified sensor was be used to detect the activity of the aspartyl protease cathepsin D. The protease is only able to digest the peptide with cleaved, reduced, disulfide. To gain information about the redox potential of this process disulfide reduction was probed by using the Glutathione redox pair in a range between -100 mV and -300 mV. A screening experiment showed that reduction of the disulfide bond of the AS35 peptides occurred at around -180 mV to -200 mV and seemed to reach an endpoint at -300 mV. Based on these results, digestion of the surface bound AS35 peptide was studied. To confirm the opening of the peptide digestion experiments with cathepsin at different potentials showed $\sim$70% fold decreases in the case when digestion were conducted at potentials over -250 mV. Whereas no changes in Raman signal and intensities could be found when the digestion experiment was done at -100 mV. This confirms that the redox potential controls the conformation of the peptide. Furthermore, through the acquisition of a homopeptide AA we constructed *in silico* peptide spectra and Spearman correlation with the spectra after the digest made it possible to determine the residual fragments on the NS surface. This simple way of sequence prediction is novel and very valuable as this makes complicated computational spectral prediction unnecessary.

Lastly, it was possible to show that a direct detection of cathepsin D is possible, as strong signals appear during the incubation of the NS-AS35 with the protease which can be mostly assigned to aromatic AA (Phenylalanines and Tyrosines) which are found at the opening of the active site of cathepsin D are not observable in the same way when looking only at the peptide, or are even found in the peptide sequence. This enables either indirect detection, via the digest of the NS surface bound peptide or direct detection of the strong Raman features provided by the protein of interest.
With this different possible applications are tested. The first one involved the

detection of extracellular cathepsin D excreted from MCF7 cells into TC media. Incubation of the sensor with media taken from a MCF7 culture resulted in digestion of the peptide and during the incubation the same strong features indicating the presence of cathepsin D could be found. Another, final experiment combined all the different aspects of this work, transferring NS surface modified with HS-AS35 into the cytosol of MCF7 cells where an abundance of the protease is available and looking at the behavior of its Raman signature. It was shown that NS-AS35 sensor can be successfully observed intracellular, even suggested that digestion might be detected similar to the *in vitro* experiments. Conclusive it was even possible to read out the characteristic features for the protease cathepsin D. This concludes the definition of the initial project to investigate feasible ways for intracellular protein detection by SERS and shows that the idea of unlabeled protein detection in cells is first of all possible and bears great promise for future applications in host-pathogen interaction research and should be pursued.

Chapter 5

Cell Raman and CARS imaging

5.1 Raman and Coherent anti-Stokes Raman scattering for the investigation of MCMV infected cells

This part of the work shows the potential of using different non-enhanced Raman techniques for the investigation of viral infection and host-pathogen interactions. First native Raman studies show the feasibility and the value of this spectroscopy technique and is followed by using CARS for investigating MCMV infection by imaging lipid droplets.

5.1.1 Single cell Raman studies for the investigation of MCMV infection in NIH/3T3 fibroblasts

Although native Raman spectroscopy as described above has its problems in live cell applications through inherently weak signal leading to long exposure times and laser powers, Raman spectra still carry a lot of valuable information. Thus, for the investigation of NIH/3T3 fibroblasts infection with MCMV first native Raman studies were conducted to find out which species of molecules, DNA, proteins, or lipids, undergo a major change during the infection process. At first Raman spectra of detached healthy 3T3 cells were taken. A suspension of trypsinized cells was placed between quartz cover slip and slide (10 μl). Spectra were taken with maximum power ∼16 mW and 150 seconds acquisition time on an experimental optical tweezing Raman system. [38] To provide statistical significance, spectra of 50 different cells were taken and averaged. For every cell spectrum a measurement was acquired next to the cell for background correction and then subtracted from each spectra. This was done to correct for auto-fluorescence of the substrate and surrounding media. Cells were infected with a multiplicity of infection (MOI) of 1.5 and incubated for 22h before 50 separate infected cells were selected and spectra of cells were averaged and water background corrected, as for the acquisitions of healthy cells. Infected cells were identified through morphological changes like a swelling and rounding of the cell and increase of the size of the nucleus, which are obvious after an infection time of 22 hours. The acquired spectra are shown in Figure 5.1.

For comparison of noninfected and infected cells the spectra were normalized to the Raman band of phenylalanine at 1004-1009 cm^{-1} rather than to that of the lipid CH_2 deformation stretch at 1450 cm^{-1} as the lipid proportion in infected cells could be considerably changed in infected cells (Figure 5.1). Spectral changes can be observed by direct visual comparison. In Table 5.1 assignments of Ramanshifts, according Jess *et al.* 2006 comparing hamster ovarian cells with and without cancer on the same Raman system, [38] and visible changes between healthy and infected cells, positive/negative signs denominate the difference between the two kinds of spectra. For example we see an increase for DNA related peaks like at around 788 cm^{-1}, 900 cm^{-1} and 1054 cm^{-1} which can be assigned to the bases C,U and

T, ribose-phosphates and CN vibrations, respectively. We also see decrease of the intensities for other molecular stretches in the infected cells, like for example higher intensities of the Raman bands at 725 cm^{-1}, 1072 cm^{-1}, 1133 cm^{-1}, 1269 cm^{-1}, 1451 cm^{-1} and 1666 cm^{-1}. These features can all be assigned to different modes of lipids. This led to the idea to further investigate the relation between intracellular lipid structures and MCMV infection in NIH/3T3 cells. For this coherent anti-Stokes Raman (CARS) imaging was applied, because it has the ability to image changes in lipid formations and structures directly.

TABLE 5.1: Comparison of Ramanshifts of infected and noninfected NIH/3T3 cells. [38]

detached	noninfected	infected	differences	assignment
617	625	621	0	C-C twist Phe
642	648	647	-	C-C twist Tyr
669	671		-	C-S stretch Cys
725	730	722	-	CH_2 rocking/ A
754	753	763	-	sym. Breath Trp
781	789	788	++	DNA: O-P-O; C, U, T
830	834	832	-	O-P-O stretch DNA
853	858	859	-	Tyr, collagen
897	900	903	+	ribose-phosphate, saccharides
936	946	943	0	C-C stretch backbone
1004	1009	1009	0	sym. Ring breath Phe
1037	1037	1037	0	C-H bending mode Phe
1054	1054	1055	+	vib(CC, CN), p(CH3)
1176	1072	1072	-	C-C v C-O stretch lipids
1095	1090		+	C-C stretch, O-P-O stretch
1135	1133		-	C-C stretch lipids
1185	1185		-	C, G, A
1210	1215	1215	-	Try and Phe vibr(C-C)
1261	1272	1269	-	=C-H in plane bending (lipids)
1318	1317	1308	-	def(CH2) collagen, A, C
1341	1349	1351	+	CH3, CH2 collagen wagging mode
1451	1457	1449	–	def(CH2) lipids
1581	1575	1576	0	A, C, G
1663	1667	1666	-	C=C lipid stretch

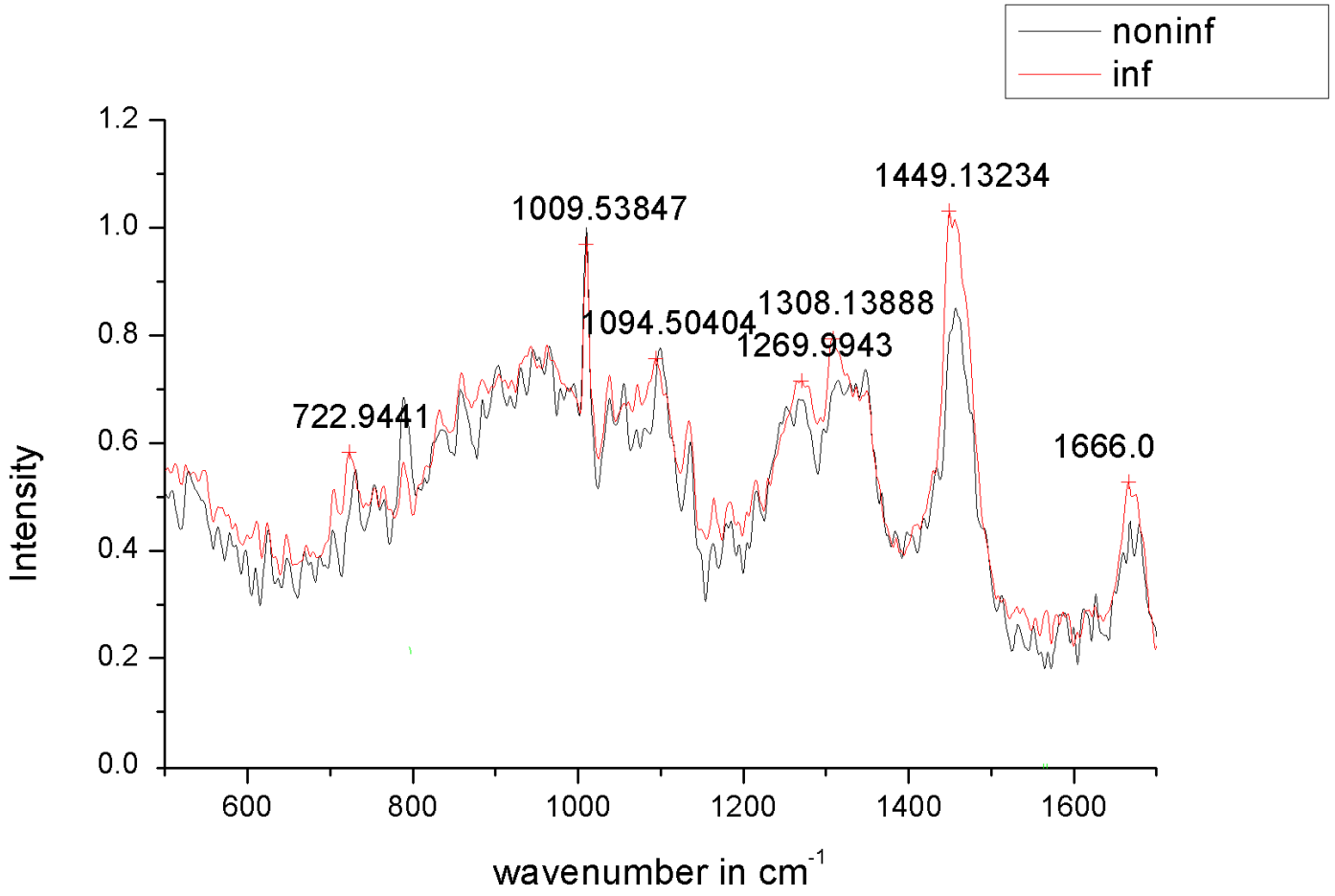

FIGURE 5.1: Spectra for noninfected and infected cells normalized to Phe peak. Underneath is shown the comparison of both by subtraction noninf/inf signal subtracted.

5.2 CARS imaging for the investigation of changes in lipid amount and conformation during MCMV infection

5.2.1 Imaging of fixed NIH/3T3 cells

CARS has the ability to image certain Raman bands and yield background fluorescence free signal by phase matched photon excitation. Therefore it is possible to observe changes in the amount and distribution of specific intracellular compounds during host/pathogen interaction.

5.2.1.1 Healthy fixed cells during CARS imaging

CARS images of 3T3 fibroblast cells were recorded for the CH_2 vibration at 2845 cm^{-1} which due to its high signal intensity and specificity for lipids, is interesting for the investigation of changes in lipid concentration during infection. Figure 5.2 shows confocal image slices of a NIH/3T3 fibroblast grown on and fixed to glass coverslips. The cell nucleus appears dark as inside the nucleus the amount of lipids is less than in the cytosol where lipid droplets, vesicles and organelles can be found. Inside the nucleus the slices, show some intranuclear inhomogeneity, caused by structural features. The fibroblast cell features are very well visible by imaging at the CH_2 stretch and the thickness of the fixed cells can be estimated to 4.5 μm. The high intensity spots are caused by lipid droplets coated in a phospholipid monolayer membrane, these are used by the cells as storage for energy reserves, hydrophobic compounds (e.g. cholesterol) and as a reservoir for lipid membrane building blocks. During this work with the a deterioration of these droplets was observed in the fixed cells with storage time of about 3-10 days, leading to bigger and more diffuse bright spots; this was also reported by Fujimoto *et al.* [176]. This is an effect of the fixing procedure with formaldehyde which only cross-links the NH-containing compounds (proteins,peptides...). This has to be taken into consideration for further investigations as a comparison of different cell samples is only possible when the lipid droplets are not deteriorated (ie imaging carried out

immediately). The size (FWHM) of the smallest lipid droplets visible in Figure 5.2 is 0.48 μm, slightly larger than the calculated resolution of the microscope, 0.38 μm.

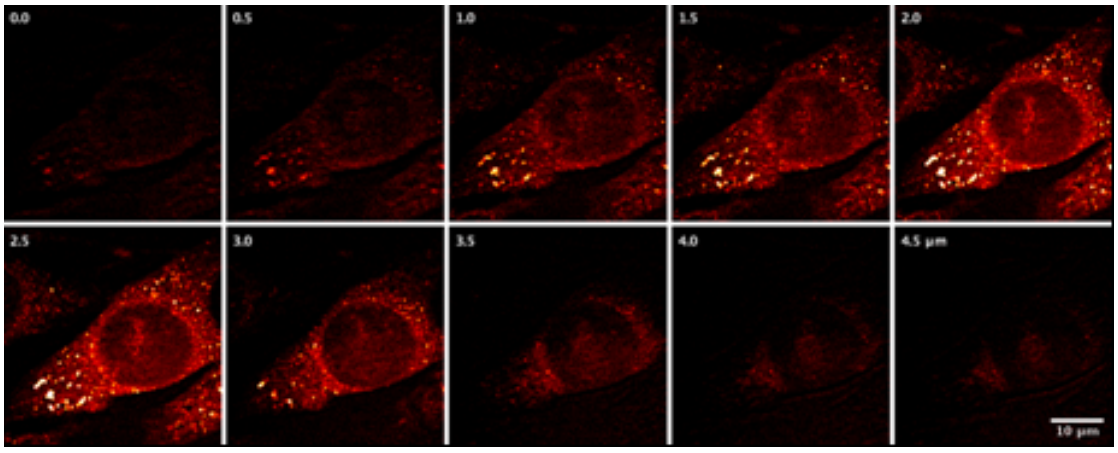

FIGURE 5.2: CARS images of the fibroblast cell at increasing depths.

5.2.1.2 MCMV infected fixed cells during CARS imaging

Cells infected with cytomegalovirus at an MOI of 1, as described in the Materials and Methods section, for 2 days were also imaged at the same CH_2 vibration. Figure 5.3 shows infected cells with the characteristic morphological changes, like a rounded cell shape, [100] contrary to the triangular stretched shape of the shown healthy fibroblast cell. We also observe the expansion of the nucleus. We can further observe areas showing very strong lipid signal, which might be explained by the compression of intracellular compartments by the nuclear expansion. Images of different cells even showed the appearance of a ring like area of high CH_2 signal. This might be caused by the recruitment of lipid droplets towards the nuclear membrane to take part in viral particle assembly and transport as recently reported for the hepatitis C virus (HCV) by McLaughlan *et al.* 2008. [177] The diameter of the nucleus in image 5.3a is 22 μm compared to 10-15 μm in healthy fibroblast cells. The nucleus can expand almost until, in later stages of infection, the whole cell seems to be filled out (images not shown).

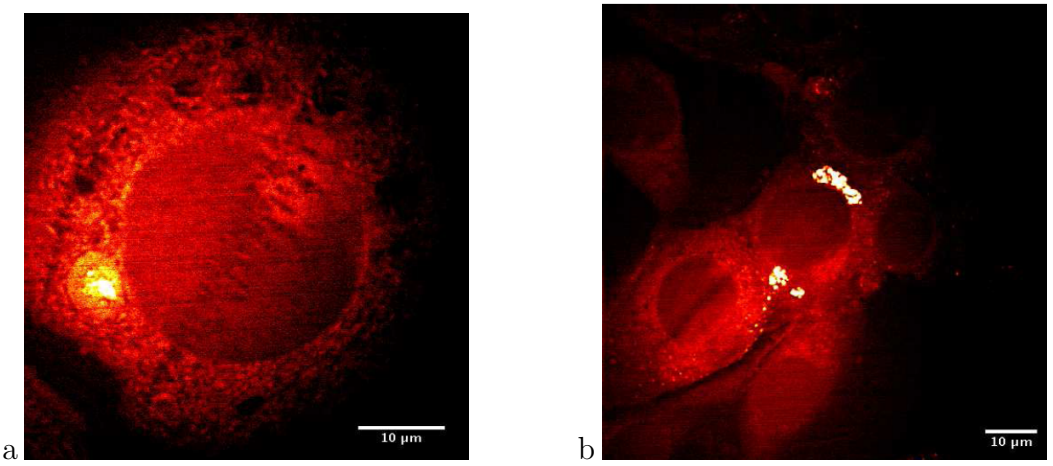

FIGURE 5.3: CARS images of fibroblast cell after 2 days of infection with MCMV at a MOI of 1. The images show the increased nuclear size and also rounding of the observed cells.

Infection of NIH/3T3 mouse fibroblast cells was confirmed by using a genetically-modified version of the Smith strain of MCMV expressing the green fluorescent protein (GFP) under the control of the immediate-early promoter 2 (IE2), constructed by Angulo *et al.*.[99, 100] The IE2 is known to promote very early viral protein expression and is the only of three CMV promotor proteins that is essential for successful infection. This allows concurrent two-photon fluorescence and CARS imaging of the fixed samples and the early timepoint of expression makes it attractive for the detection of viral infection. Although the CARS signal wavelength, 593 nm, overlaps the tail of the GFP emission spectrum no fluorescence signal was observed in the CARS detection channel, this is due to the use of narrow band pass filters for CARS which blocks the GFP emission maximum around 509 nm. The cells visible in the CARS image, 5.4(A), show again the characteristic morphological changes, e.g. nuclear expansion and rounding of the cell. Lipid droplets are also visible as bright spots in these cases as well. Figure 5.4B shows the TPF image of GFP which is expressed together with the viral originated proteins in the cytosol. Remarkable is that we find areas in a cell which seem to be totally depleted of fluorescence. Coincidental these are the areas identified as lipid droplets with CARS imaging which is obvious in the superimposed picture containing the CARS as well as the TPF image in 5.4(D). The observed effect was to be expected as the hydrophile GFP has no means to enter lipid droplets. This means that we are able to do label free studies on lipid droplets and on the other

hand have the simultaneous ability to detect fluorescence signals from one or more fluorescent proteins during viral infection. Co-localization gives then information about interaction and correlation of viruses infection with lipid droplets. This same set of images also shows that we observe the infection of cells at different stages in this experiment, as some of the cells already show morphological signs of infection but very low GFP intensity. Others, however, show very bright green fluorescence and also lipid droplet aggregation. The meaning of this is that to obtain homogenous infection a synchronization step has to be included in the infection protocol. A simply form of synchronization is a 30 min cold treatment, at 4 ° directly after exposure to the MCMV virus. This was then conducted in every experiment hereafter.

5.2.1.3 Investigation of the timecourse of MCMV infection in NIH/3T3 fibroblasts

To elucdiate the above mentioned stages of infection with GFP modified MCMV we conducted an infection time course and CARS/TPF imaging experiment. Cells were grown on polylysine coated glass cover slips as described above and the infection with GFP-MCMV was interrupted by fixing the cells at different timepoints(0.5, 3, 6, 9, 12, 24, 48, 96h). We observed concurrently the start of the GFP production inside the cells with TPF and also the change in the lipid composition/ lipid droplet structures inside the cells. Figure 5.5 and 5.8 show representative images of the samples at the mentioned timepoints. Over the course of the experiment different stages can be observed. In the beginning, 0.5 and 3 h, the initial stage of infected cells show nearly no green fluorescence, weak signal can be attributed to autofluorescence of the cellular proteins, the lipid droplets are small and distributed homogenously. Although no morphological changes can be observed the infection is indicated by green fluorescing spots, which might be attributed to GFP just be completed in the Golgi apparatus, final folding, and therefore localized in distinct areas. Further evidence for this we see after 6 h where more of these bright green areas appear and also GFP signal becomes more obvious all over the cells, the infection of the cells is well on its way. Also, the nuclei are enlarged at this timepoint. Regarding the lipid droplets conclusive statements

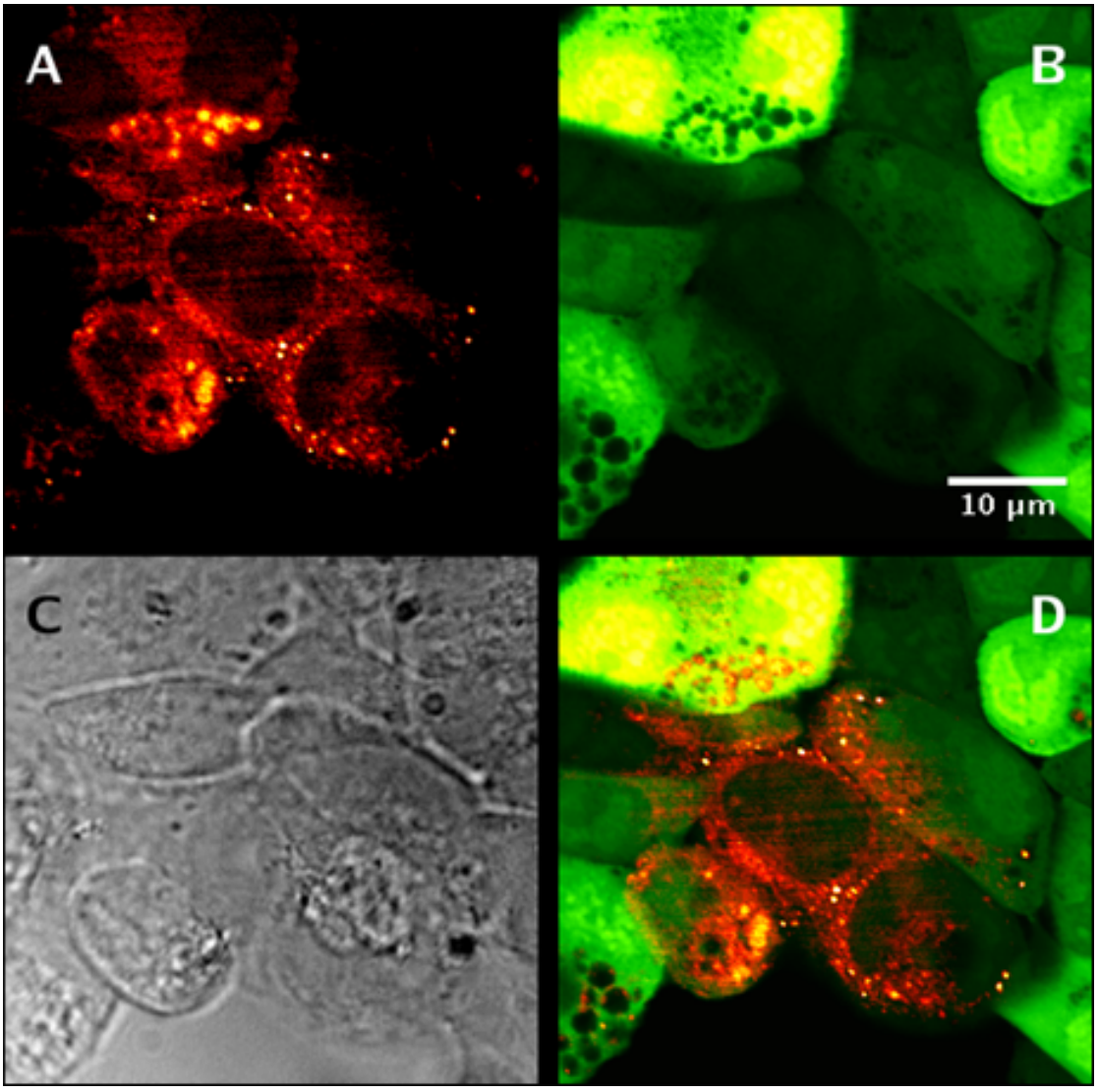

FIGURE 5.4: CARS images of NIH/3T3 cells at a Raman shift of 2845 cm^{-1} (A). As after 2 day of infection with a gen modified MCMV which expresses the green fluorescent protein with the IE 3. A two-photon image of GFP from the same set of cells is shown in (B). A bright field image was recorded (C). The CARS and GFP images are overlayed (D)

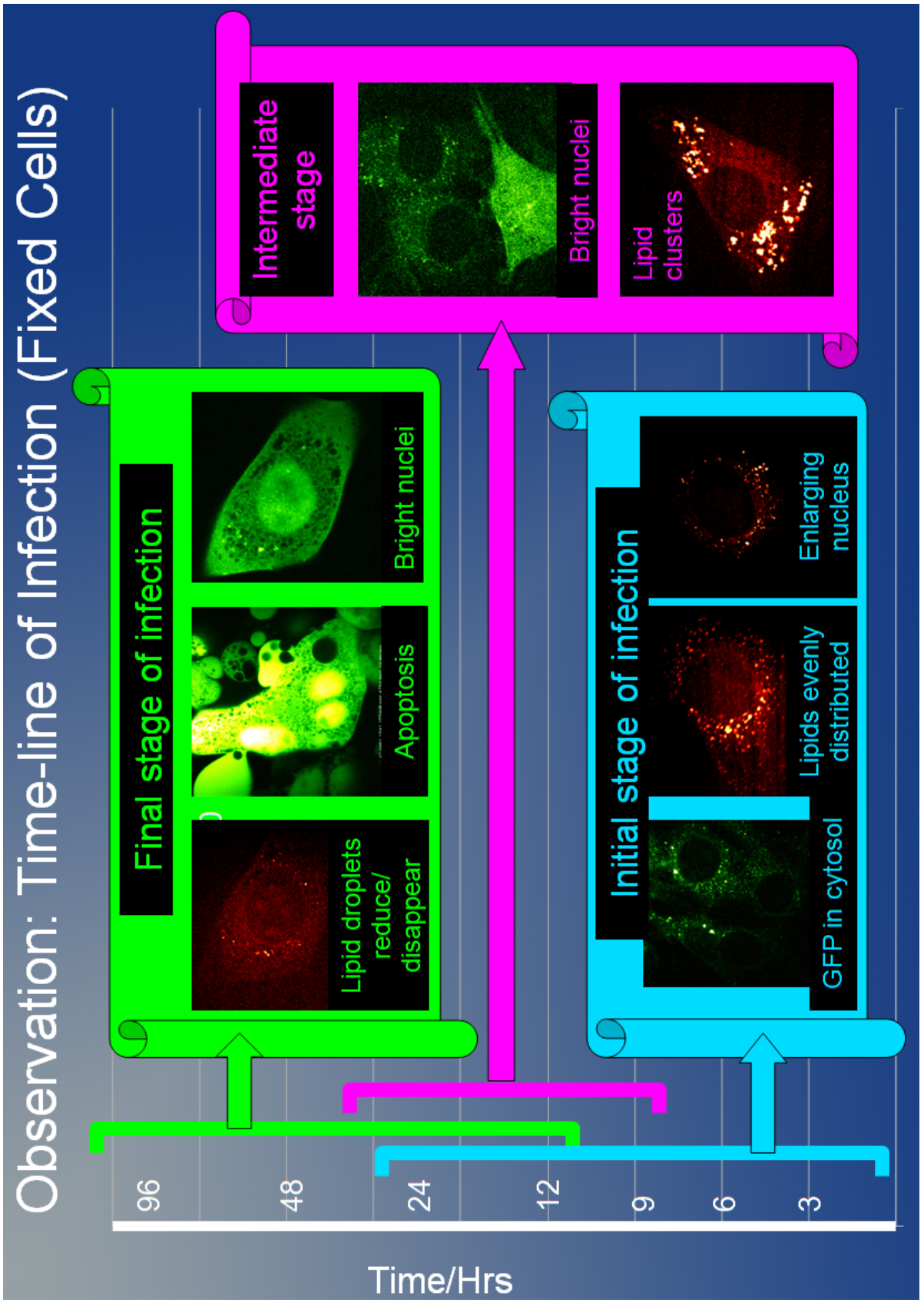

FIGURE 5.5: Chart describing the different stages of infection observed by CARS and TPF imaging

can not be done, there appear to more of them, but the distribution is still very similar to healthy cells. Figure 5.89h shows higher fluorescence signal and slightly more clustering of lipiddroplets.

Furthermore we see a higher amount of lipid droplets which tend to gather or form clusters around the nucleus. This intermediate stage of infection also shows between 12 h and 48 h a migration of lipid droplets towards cell-cell boundaries, which might suggest that the virus is using the intracellular lipid droplet transport mechanisms. The motion of lipid droplets especially towards the cell-cell interface suggests that the virus exploits lipid droplets for further infection. Similar results have been shown with HCV using CARS. [178] Another noteworthy observation is the increase of GFP inside the nucleus, which is not easily explained but could be a result of the active deterioration of the nuclear laminar by the virus as reported by Muryani *et al.* 2002, but would not explain the accumulation of GFP inside the nucleus. [179] The GFP signal inside the nuclei is unexpected because the gene-construct does not include a nuclear target sequence as some of the viral proteins do. On the other hand this could be further evidence of the employment of lipid droplets for viral protein transport as an increase of lipid droplets around the nucleus can be observed at the same time. We therefore suggest that the lipid droplets are used as shuttles for the transportation of viral proteins or transfer of the completed virus towards the cell membrane. Further studies have to be conducted before this can be conclusively proven

After 48 h the images show that the cells undergo apoptosis, which the virus suppresses during the infection. The image at 96h nicely shows the fragmentation of the nucleus and as a result of the whole cell. The higher concentration of GFP in the nuclear fragments makes it easy to distinguish from cytosol derived fragments to nuclear fragments. Another interesting observation is the dependence on infection stage of the amount of lipids. This seems to decrease in the later stages of infection to near background signal. For now it is not possible to quantify the imaging results, but will be solved in the future. Another problem of the above described experiments is the use of fixed cells. Although the handling is seemingly unproblematic and fixed cells have been applied to date in all kinds of experiments, we observed a deterioration of lipid structures, a diffusion of lipid boundaries, when

samples are not immediately imaged. Therefore the next section describes live cell imaging experiments.

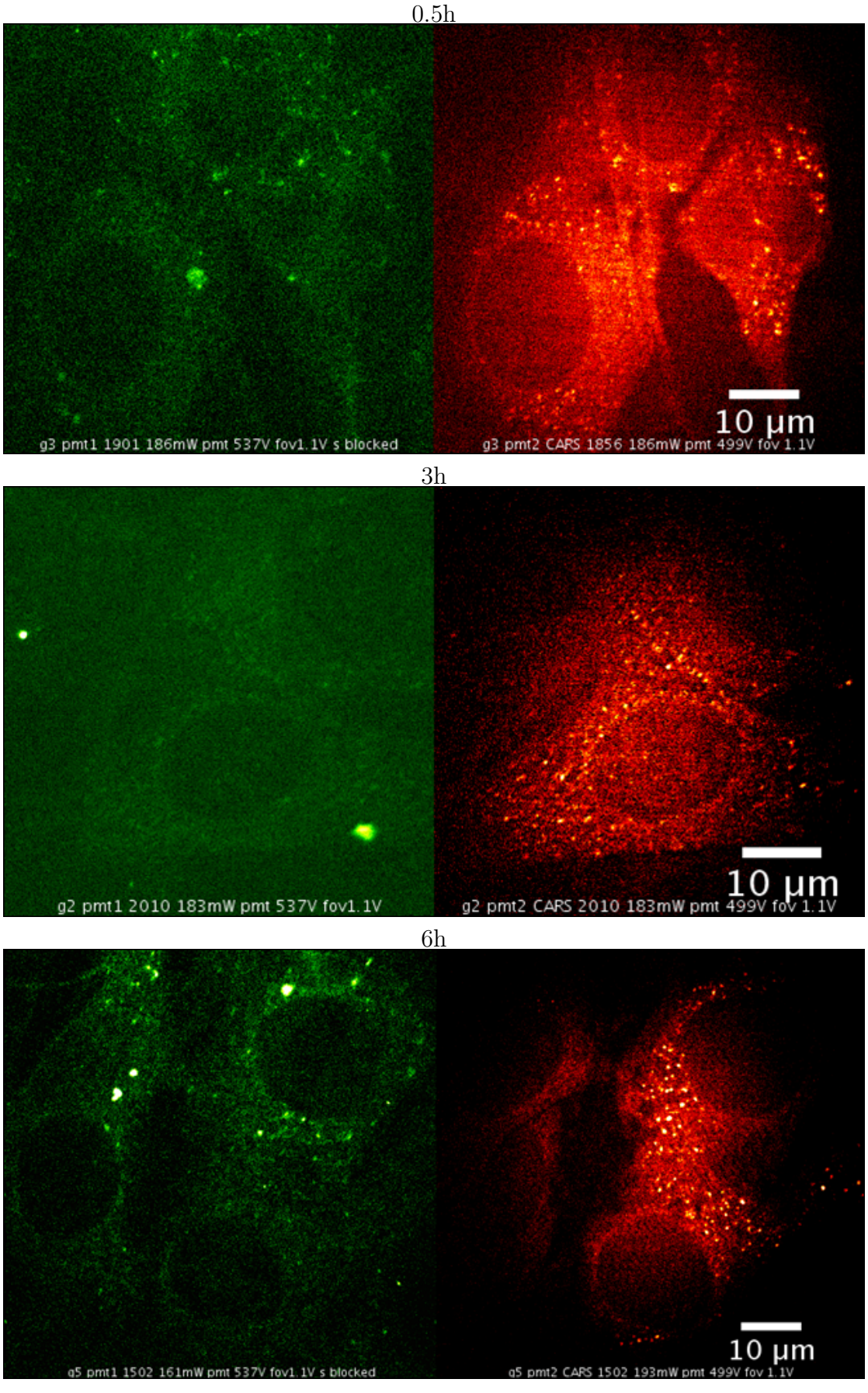

FIGURE 5.6: Fixed MCMV infected fibroblast cells at timepoints 0.5 h, 3 h and 6 h after infection imaged simultaneously with CARS and TPF.

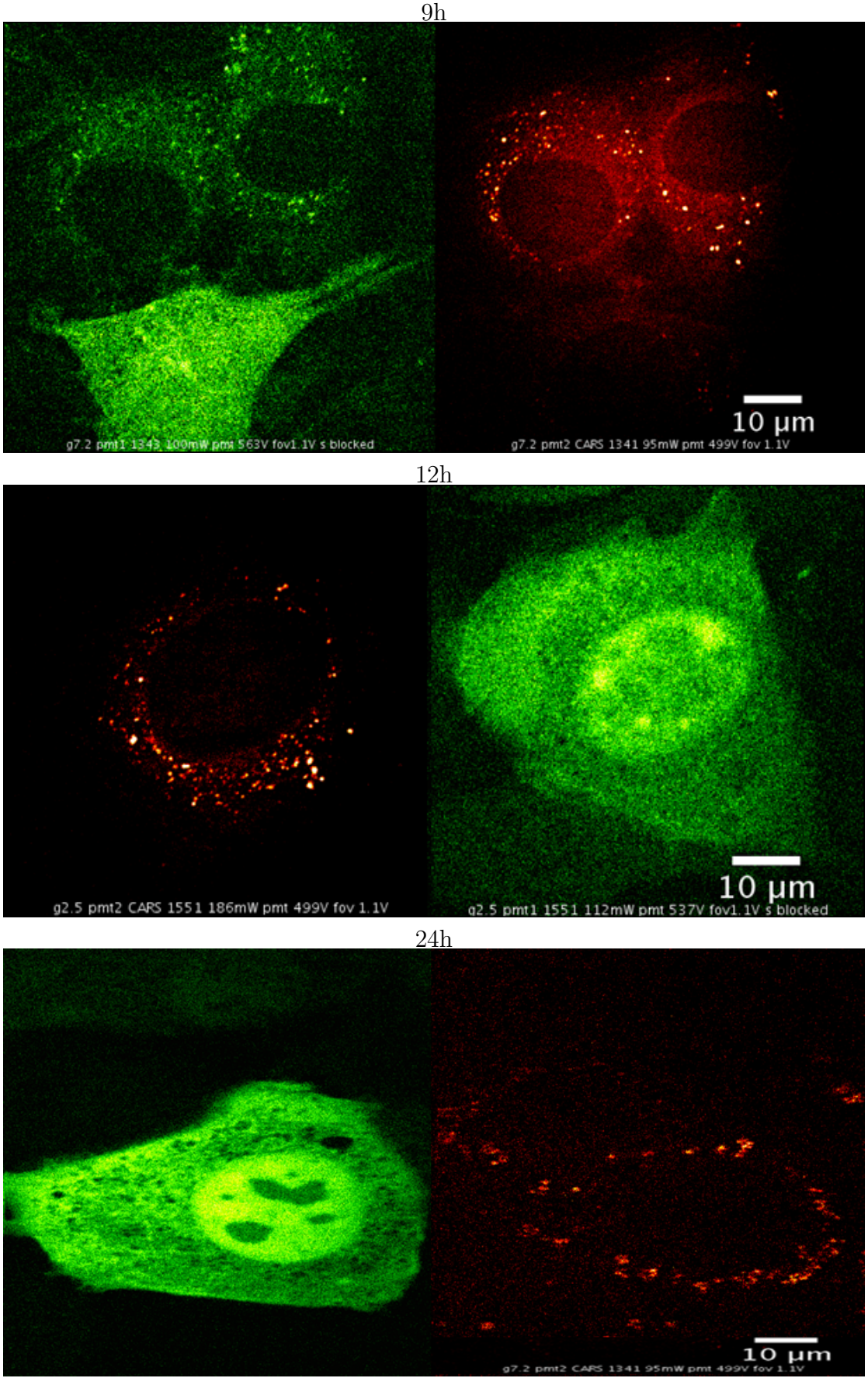

FIGURE 5.7: Fixed MCMV infected fibroblast cells at timepoints 9h, 12h and 24h after infection imaged simultaneously with CARS and TPF.

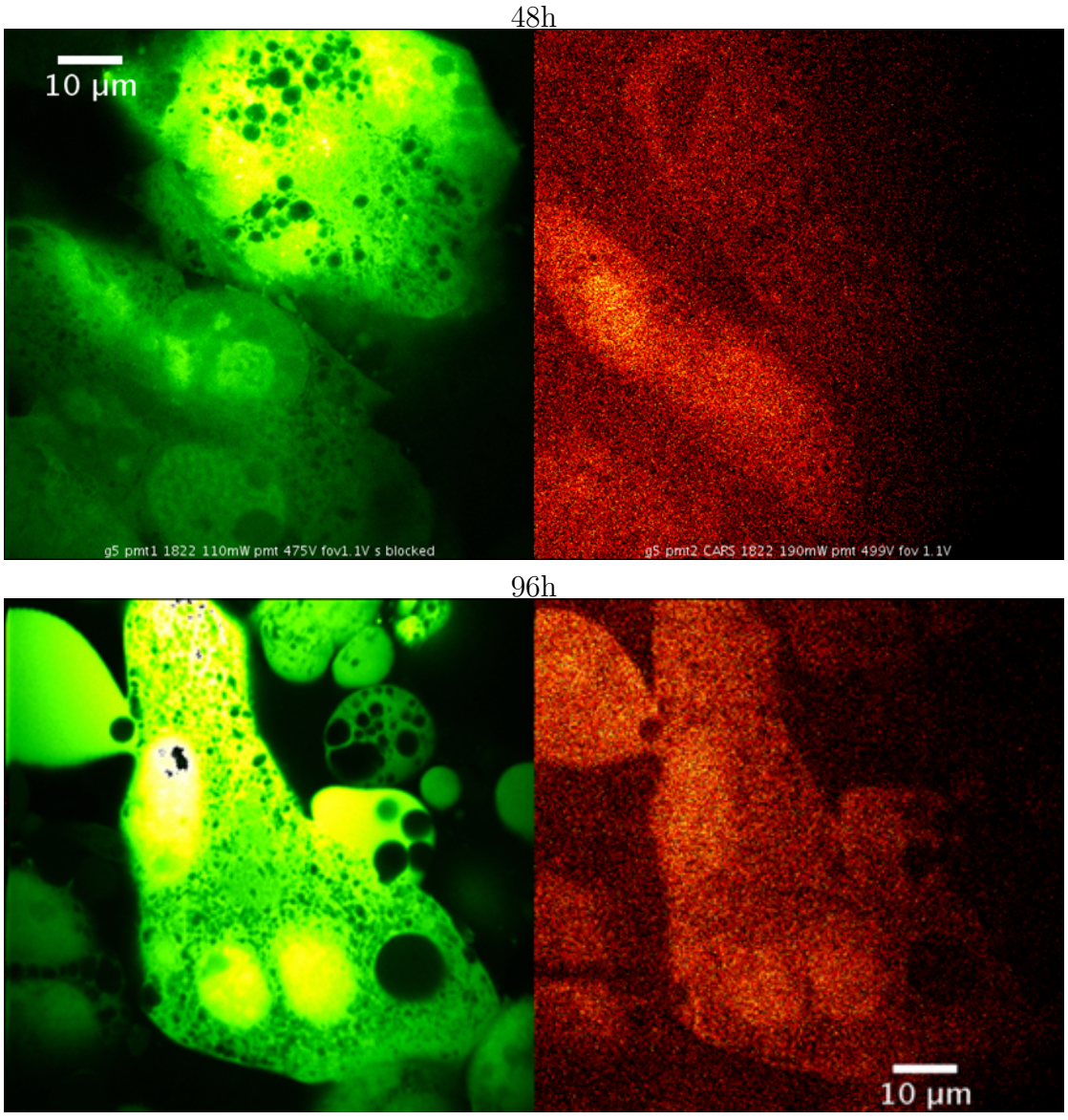

FIGURE 5.8: Fixed MCMV infected fibroblast cells at timepoints 48h and 96h after infection imaged simultaneously with CARS and TPF.

5.2.2 CARS imaging on living NIH/3T3 fibroblasts

For live cell imaging a chamber was designed and fabricated, which could be implemented in the above described and used imaging setup and was able to provide detection in the forward and backward direction. Initial questions to be answered were, is the sealed chamber enough to keep the cells healthy over a longer period of time. Furthermore, how much laser power can the cells withstand during an imaging experiment and is it possible to image one cell over the course of hours or days.

5.2.2.1 Live cell imaging

The constructed chamber was first tested loaded with cells and proved to keep the temperated chamber at 37±0.2 degrees stable over 7 days. The incubated cells grew normally and after reopening of the chamber the phenolred stained media indicated that neutral pH was maintained. Therefore we suspect that the CO_2 concentration stayed relatively constant in a sealed chamber as was also reported by Stevenson *et al.* 2008, who used a Carrel flask as a simple sealed cell culture chamber. [101] First imaging experiments were conducted to test for the best laser power to be used and whether the cells experience detrimental effects. The lowest possible laser power, still leading to good CARS signal of cellular lipids, has been found to lie around 30 mW ps-pulses for live cell imaging on our system. But even with this relatively low energy cells rounded up after 10-20 min of constant scanning. Therefore we found that it is not possible to carry out long timecourse experiments on only one cell, for now.

5.2.2.2 Investigation of MCMV infection in living cells with CARS

As the images of living cells showed promising results a similar infection experiment as carried out on fixed cells was conducted on live cells. The further advantage of live cell imaging is that we only work with one cell population, not and this is different to the fixed cell timecourse experiment where cells are grown on different slides in quasi identical conditions. Therefore we follow the course of infection

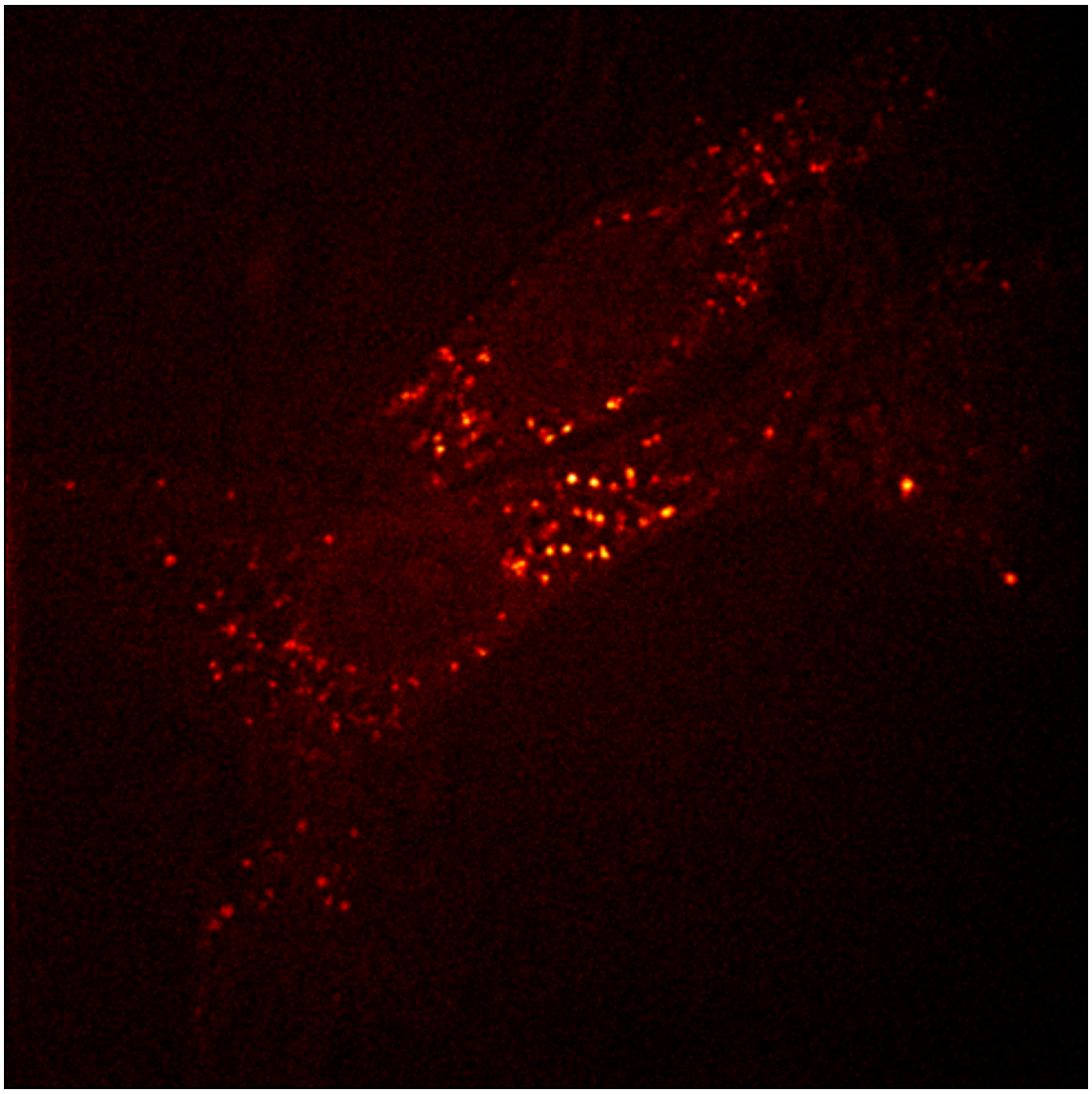

FIGURE 5.9: Representative image of living and healthy NIH/3T3 fibroblast

without any further intervention, for example temperature fluctuations during handling or fixation.

In this experiment the cells were seeded at 50 % confluence and infected with the GFP-MCMV construct at a MOI of 1 and imaged at 1 h hour intervals for three days. Figures 5.10 show representative acquired images for different stages of infection. In the initial stage (0.5-3 h after infection) nearly no green fluorescence could be found (Figures 5.10a) and the lipid droplet distribution is homogenous as in the above shown healthy cells in Figure 5.9. Between 6 and 48 h of infection

morphological changes become visible, such as an increase in the nuclear diameter. Furthermore the lipids seem to form bigger aggregates in this period, gathering around the nucleus. The droplets also seem to aggregate to a higher extent near the membrane, especially where a cell-cell interface can be found as shown in Figure 5.10b. This result is similar and even better than in the fixed cell experiment and strengthens the suggestion of a relationship between lipid droplets and viral assembly and possible transportation as describe above. Furthermore, a possible cell-cell infection mechanism via the cell-cell boundary, seems more probable with images of this kind as a trend of lipid droplets moving towards a neighboring cell is well visible. Figure 5.10b even shows two cells which seem to have different GFP intensities but also show different amounts and localisations of lipid droplets in both cells. For now, proper quantification of this kind of information is not available on the employed set-up. If the fully assembled viral particles use the lipid droplets as shuttles which move them to cell-cell interface membranes this would suggest that infection depends strongly on lipid droplets. In the final stage after 48h CH_2 CARS intensity again drops to a very low level and the cells are flooded with GFP gaining high TPF signal. Furthermore cell death through apoptosis can be observed the same way as in the fixed cell experiment (Figure 5.10c). It is thus possible with the constructed incubation chamber stage to image living cells directly, non-invasively and allows imaging of biological process conveniently by CARS imaging, giving information about localisation and amount of lipids and their droplets during biological processes like the infection of murine NIH/3T3 fibroblasts with MCMV.

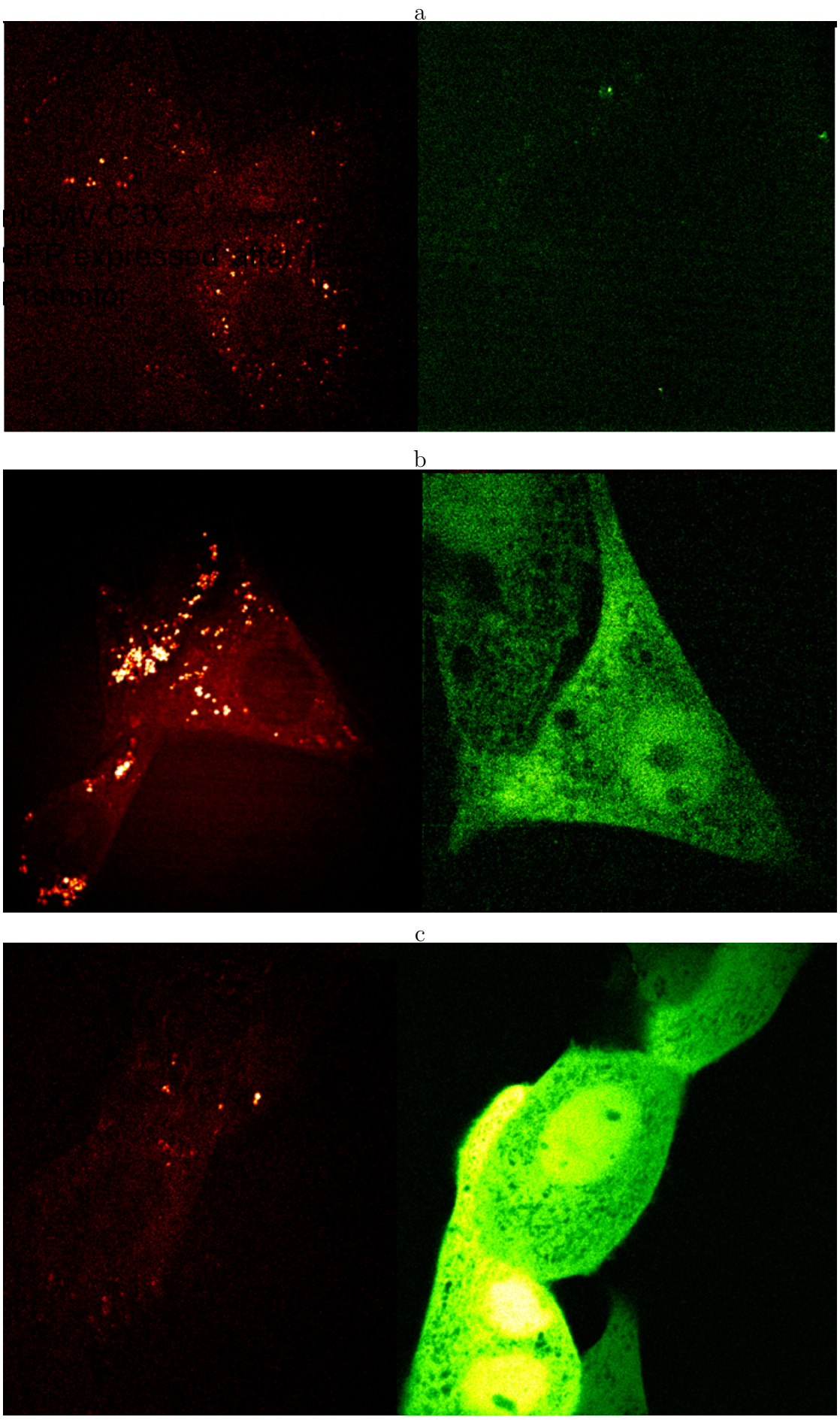

FIGURE 5.10: CARS and TPF of GFP-MCMV infected fibroblast cells during a) initial, b) intermediate and c) final stage of infection

5.3 CARS as a powerful imaging tool for TC applications

This final part of this work investigated a further Raman spectroscopy based technique, coherent anit-stokes Raman. CARS imaging was used to investigate the changes of intracellular lipid changes during the infection of NIH/3T3 fibroblasts with the β herpes virus cytomegalovirus in order to find information about the relationship between lipid droplets and the infection processes. Initial native Raman signals of single healthy and MCMV infected fibroblast cells showed specific differences for DNA as well as for lipid stretches like at 1470 cm^{-1} and 1666 cm^{-1}. The observed intensity increase suggested a possible increase of lipid compound and thus CARS imaging was employed to elucidate this finding.

It was first shown that signal can be obtained by observing the CH stretch of lipids at 2845 cm^{-1} of NIH/3T3 cells fixed on glass coverslips. The images made it easy to distinguish between the cellular membrane, the nucleus and lipid droplets. The visibility of this kind of intracellular lipid storage unit by CARS imaging has been reported before working with a different system to the Syncro-locked CARS system used in this work. [158] The behavior of the lipid droplets during an infection process was first observed in an experiment using fixed cells infected with MCMV over 2 days. Here an interesting clustering and localization of high lipid amounts, probably lipid droplets, near the nuclear membrane was observed and suggested a relationship between the infection process and lipid droplet arrangement. To be sure of infection, a GFP expressing virus of the same phenotype was utilized to show the actual infection event. This was possible because of the two photon excitation capability of fluorescent dyes and the coincidence that the employed **509** nm laser line overlaps with the excitation range of GFP. Two photon fluorescence (TPF) gave reliable information about infection and also to some extent the stage of infection the cells are in. Therefore a timecourse on fixed cell experiment was conducted to give information of the infection over the whole process of infection. For this cells were infected and the infection process stopped at regular timepoints over a period of 4 days. It was possible to separate the whole process into 3 possible stages of infection with certain characteristics regarding the TPF and CARS

signals. In the initial stage between 0-9h the lipid droplet distribution showed only slight differences to uninfected cells and only during the later hours of this stage GFP-TPF signal can be detected sparsely in the cytosol. The intermediate stage between 9-24 hours is typified as an increase of GFP in the cytosol confirming the infection with the virus. The lipid droplets amount starts to increase and an accumulation and aggregation of droplets around the nuclear membrane could be observed. This leads to the final stage where a decrease of the lipid amount was observed accompanied with an increase in fluorescence. In this time period apoptosis induced fragmentation and cell death could be observed.

CARS imaging was also conducted on living cells with an incubation chamber specially designed and constructed for this purpose. In live cell experiments CARS images of the same quality could be observed on healthy cells. Experiments on MCMV infected cells NIH/3T3s confirmed the findings of the fixed cell experiments. Interpretation of these results suggest that also in MCMV infection, like in HCV infection, lipid droplets might be used as transport vehicles for the viral constituents in the cell and the probably fully assembled viral particle towards the cellular membrane. This hypothesis would explain the decrease in lipid droplet amount in the final stage of infection, which is worth investigating in future work.

This shows that CARS imaging can be a very useful tool for the investigation of host/pathogen interactions which promises in future to be more and more versatile and might at some point be the technique of choice in biological studies.

Chapter 6

Conclusions

In the past decade SERS has become a hugely important technique for the study of biological systems. Its utility has been demonstrated in a variety of systems spanning from fundamental studies of drug/membrane interactions to applications in *in vitro* diagnostics. One of the challenges in measuring reliable, quantitative SERS spectra is the development of reliable, reproducible surfaces on which to measure these spectra. Nanoshells are an excellent example of such an engineered nanostructure whose absorbance can be tuned to work well within biological systems and whose strong plasmon resonance allows SERS spectra to be collected from single particles under very gentle illumination conditions. The broad utility of SERS makes it an attractive alternative to fluorescence for intracellular imaging and can be used to measure for example pH inside mouse fibroblast cells. Importantly, delivery of NS to cells can be controlled and shows promise for selective targeting of specific organelles. In a complex living system such as a cell it is important to establish that adding an imaging contrast agent such as a modified nanoparticle does not have an adverse effect on physiology. Investigations using a variety of assays have determined that cells continue to grow in an unperturbed manner and do not undergo either programmed or necrotic cell death. Future studies involving cell responses on nanoparticle incubations should deal with possible metabolic and gene regulatory effects, like up/down regulation of proteins or signaling peptides, for the various kinds of particles and their resulting biosensors.

The surface sensitivity of SERS allows conformational changes to be measured and we have used this aspect to probe conformational switching in a G-quadruplex oligonucleotide. The ability to probe conformational changes has led us to use SERS to measure protein concentration on the basis of changes in aptamer structure caused by protein binding. This finding opens the door to a general method of protein detection using SERS and structure-switching aptamers, although new methods of aptamer selection and design may be required in order to generate a broader suite of functional aptamers. As a probe of biomolecular structure, SERS is not limited to investigations of nucleic acid structure and it was possible to successfully design a peptide based sensor giving information about redox potential changes and a simple way of detecting a specific protein in *in vitro* and more importantly made *in vivo* measurements possible. Furthermore a novel way of spectra prediction with the help of an amino-acid library and statistical functions was established, giving the opportunity to analyse Raman spectra not based on complicated vibrational assignments. Improvement in data processing and analysis with the help of different statistical methods will lead to an increase of information obtained from SERS sensing experiments.

Since several research groups have established the principal of intracellular SERS imaging, there is a need for a much greater array of modified nanoparticles which can probe (for example) a larger range of protein concentrations, biomolecular interactions, small molecule concentrations or states such as redox potential. Furthermore, in order to ensure that measurements are made in specific locations, there is a need to improve targeting of nanoparticles to specific organelles in a predictable and reproducible manner. While this will entail a considerable effort, it is essential to ensure the translation of this technique from a niche area of physical science research to a technique of choice for life-scientists. Similar nano probes might even lead to devices able to be implanted for medical diagnostics in various diseases as the data acquisition is gentle and very sensitive.

Another Raman based method, coming of age for imaging, is coherent anti-Stokes Raman scattering and its application was presented here to investigate the lipid structural changes of cells during the process of infection. This technique is not dependent on any Raman label, but has the general ability to detect every molecule on the basis of its characteristic vibrations. In this work we were able to show that

the lipid structure of a mammalian cell line during the infection with a herpesvirus changes depending on the phase of infection. Lipids were chosen because of their abundance but also because of the strength of their Raman signal and biological relevance. This technique showed promising results for the application of fixed and living cells but still struggles with high laser powers damaging the sample, especially living organisms. In contrast to other Raman techniques CARS is very young technique with lots of room for improvement on the side of tune-ability to different kinds of molecules, therefore investigations of different types of cellular compounds, like proteins and DNA, and also on the side of instrumentation to decrease acquisition time and laser power to make it more suitable life-science research. When technical problems like quantification of signal possible by analytical means. To quantify data a standard has to be introduced to each measurement to make them comparable and then a signal normalizing and thresholding algorithm, capturing only the cells of interest, has to be created for the data analysis. Further work has to be conducted on a more gentle way of CARS live cell imaging, with lower laser powers and if possible also lower acquisition times, to prevent (two)photon-damage, and also finding a way of characterizing photo-damage on single cells would be useful. Optimization of optics and alignment, but also better detection systems might be beneficial.

The presented work shows the potential of these exciting novel techniques, which will emerge in future as leading molecular imaging methods for research but also for clinical work.

Appendix A

Supporting graphs

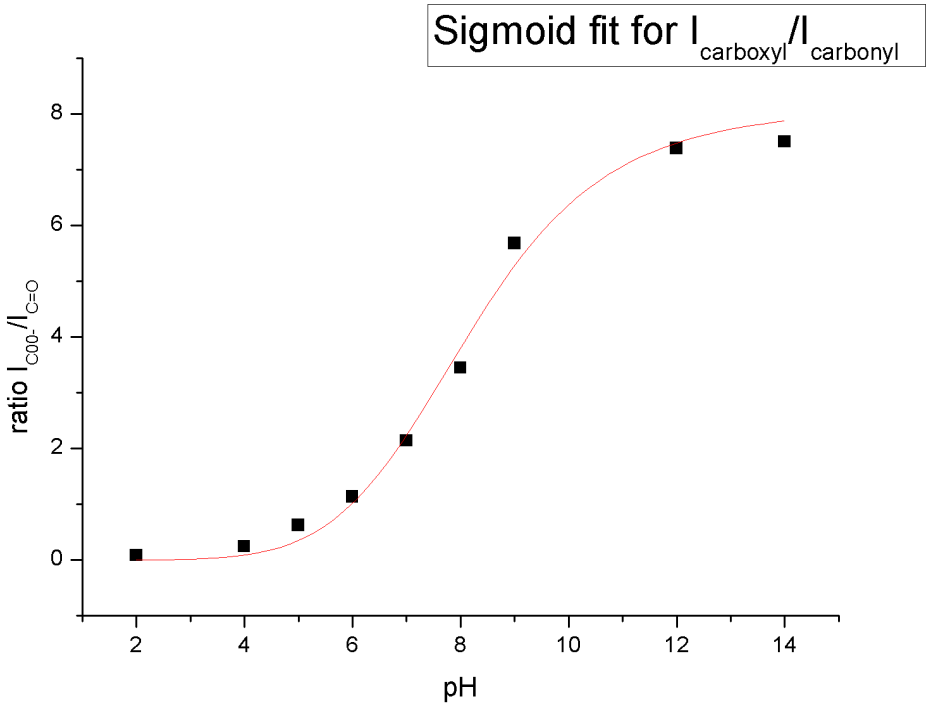

FIGURE A.1: Calibration curve for pH sensing applications

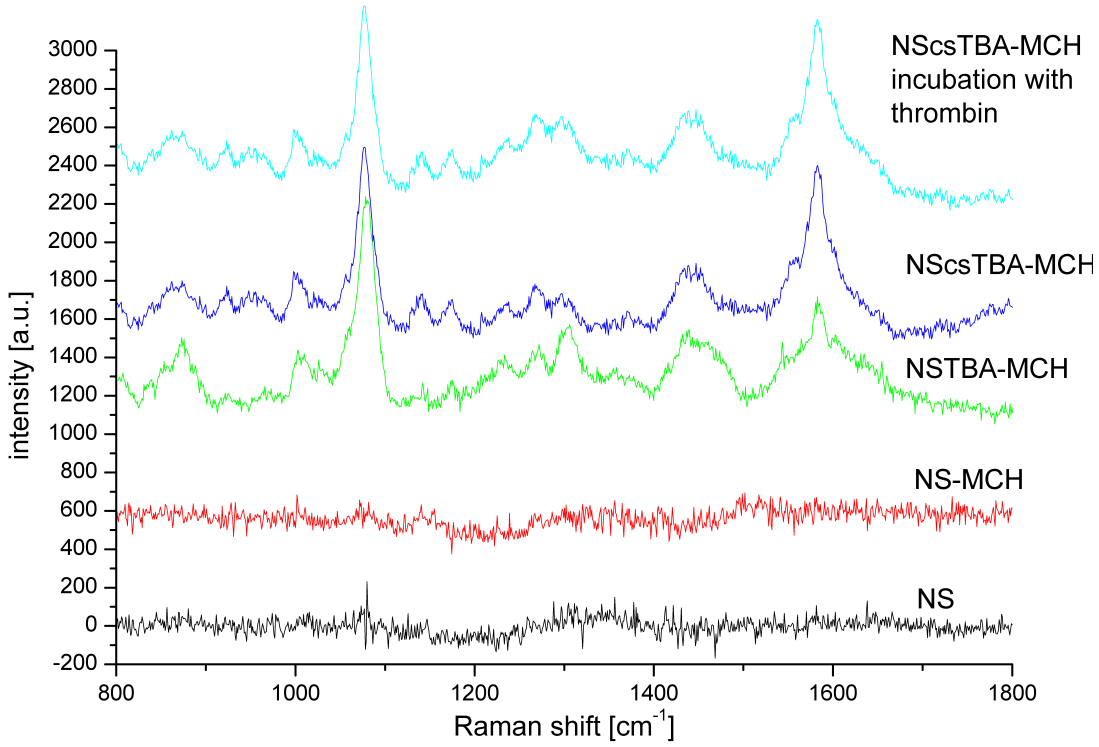

FIGURE A.2: Spectra with control sequence oligonucleotides for NSTBA incubated in buffer and with thrombin.

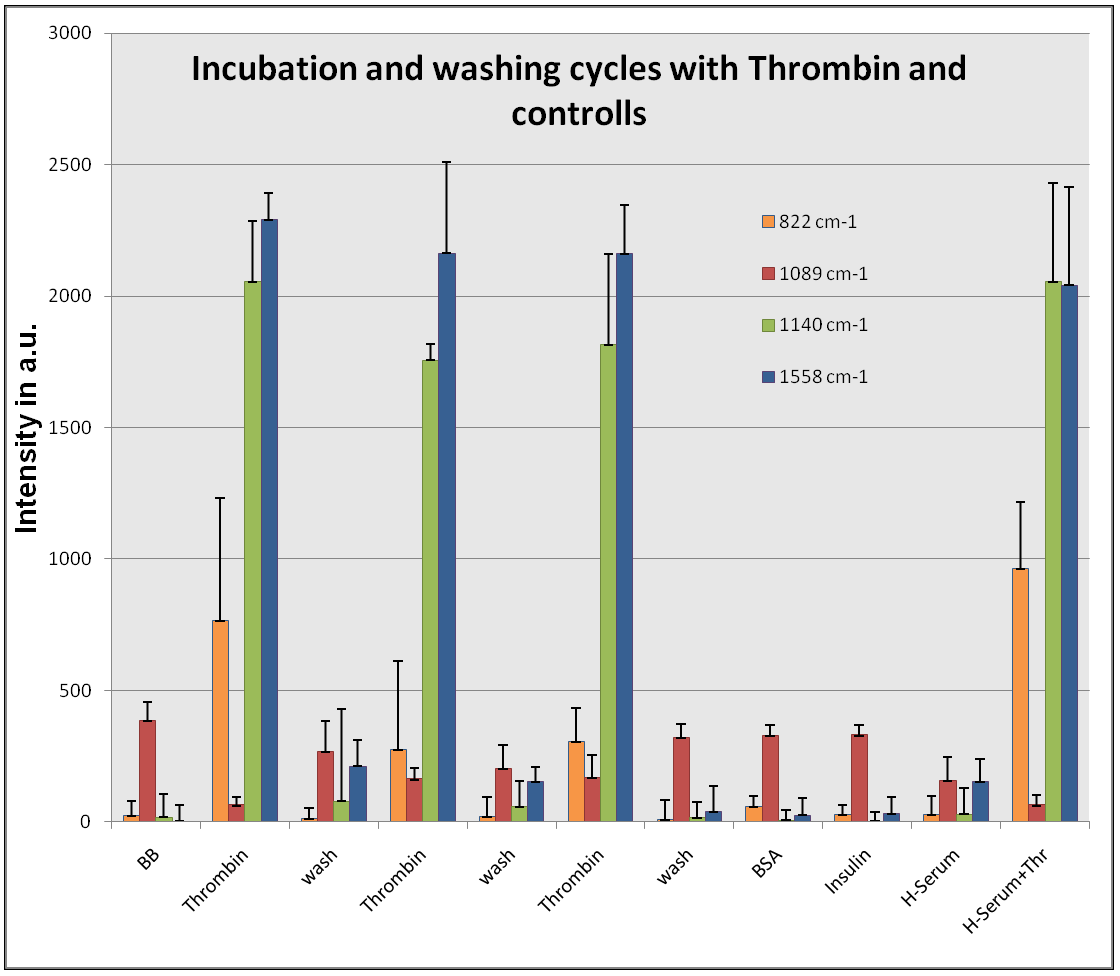

FIGURE A.3: NS-TBA sensor reproducibility experiment inclusive error bars showing 2x standard deviation 10 spectra

Bibliography

[1] R. Calinger. *A Contextual History of Mathematics*. John Wiley & Sons, 1999.

[2] L.S. Taylor. 1998. URL http://www.ece.umd.edu/~taylor/optics.htm.

[3] C.E. Ganeau. *Memoires pour l'histoire des sciences et des beaux arts*. Paris: Impr. de S. A. S., 1990.

[4] K.E. Kalumuck. *Towards CARS Endoscopy*. Kendall/Hunt Publishing Company, 2000.

[5] Brian Larson. *NDT Education Resource Center*, 2001-2010. URL http://www.ndt-ed.org/index_flash.htm.

[6] D. Wöhrle, M.W. Tausch, and W.-D. Stohrer. *Photochemie - Konzepte, Methoden, Experimente*. Wiley-VCH Verlag GmbH, 1998.

[7] M.E. Phelps. Pet: the merging of biology and imaging into molecular imaging. *Journa of Nuclear Medicine*, 41:661–681, 2000.

[8] R. Alford, M. Ogawa, P.L. Choyke, and H. Kobayashi. Molecular probes for the in vivo imaging of cancer. *Molecular Biosystems*, 5:1279–1291, 2009.

[9] A. Saraste, S.G. Nekolla, and M. Schwaiger. Cardiovascular molecular imaging: an overview. *Cardivascular Research*, 83:643–652, 2009.

[10] A. Signore, S.J. Mather, G. Piaggio, G. Malviya, and R.A. Dierckx. Molecular imaging of inflammation/infection: Nuclear medicine and optical imaging agents and methods. *Chemical Review*, 110:3112–3145, 2010.

[11] R. K. Gupta, S. S. Patterson, S. Ripp, M. L. Simpson, and G. S. Sayler. Gupta, r. k. and patterson, s. s. and ripp, s. and simpson, m. *FEMS Yeast Research*, 4:305, 2003.

[12] G. S. Lipshutz, C. A. Gruber, Y. Cao, J. Hardy, C.H. Contag, and K.M. Gaensler. In utero delivery of adeno-associated viral vectors: intraperitoneal gene transfer produces long-term expression. *Molecular Therapie*, 3:284–289, 2001.

[13] N.Kh. Tafreshi, M. Sadeghizadeh, R. Emamzadeh, B. Ranjbar, H. Naderi-Manesh, and S. Hosseinkhani. Chemiluminescent and bioluminescent analysis of plant cell responses to reactive oxygen species. *Biochemistry*, 412: 27–32, 2008.

[14] S.W. Hell and J. Wichmann. Breaking the diffraction resolution limit by stimulated emission: stimulated emission depletion fluorescence microscopy. *Optics Letters*, 19:780–82, 1994.

[15] S.T. Hess, T.P. Girirajan, and M.D. Mason. Ultra-high resolution imaging by fluorescence photoactivation localization microscopy. *Biophysical Journal*, 91:4258–4272, 2006.

[16] G. Patterson, M. Davidson, S. Manley, and J. Lippincott-Schwartz. Superresolution imaging using single-molecule localization. *Annual Reviews of Physical Chemistry*, 61:345–367, 2010.

[17] E. Hutter and D. Maysinger. Gold nanoparticles and quantum dots for bioimaging. *Microscopy Research and Tecnique, ahead of print*, 2010.

[18] A.K. Kenworthy. Imaging proteinprotein interactions using fluorescence resonance energy transfer microscopy. *Methods*, 24:289–296, 2001.

[19] J. River and Bravo J. Megias, D. and. Sorting nexin 6 interacts with breast cancer metastasis suppressor-1 and promotes transcriptional repression. *Journal of Cellular Biochemistry, accepted*, 2010. URL DOI10.1002/jcb.22874.

[20] J.S. Burmeister, L.A. Olivier, W.M. Reichert, and G.A. Truskey. Application of total internal reflection fluorescence microscopy to study cell adhesion to biomaterials. *Biomaterials*, 19:307–325, 1998.

[21] D.K. Hoover, E.-J. Lee, and M.N. Yousaf. Total internal reflection fluorescence microscopy of cell adhesion on patterned self-assembled monolayers on gold. *Langmuir*, 25:2563–2566, 2009.

[22] J.Z. Zhang. Biomedical applications of shape-controlled plasmonic nanostructures: A case study of hollow gold nanospheres for photothermal ablation therapy of cancer. *Journal of Physical Chemical Letters*, 1:686–695, 2010.

[23] M. Dahan, S. Levi, C. Luccardini, P. Rostaing, B. Riveau, and Triller A. Diffusion dynamics of glycine receptors revealed by single-quantum dot tracking. *Science*, 302:442–445, 2003.

[24] K.S. Kim, W. Hur, S.-J. Park, S.W. Hong, J.E. Choi, E.J. Goh, and S.K. Yoon SK, Hahn. Bioimaging for targeted delivery of hyaluronic acid derivatives to the livers in cirrhotic mice using quantum dots. *ACS Nano*, 4: 3005–3014, 2010.

[25] L.T. Rosenblum, N. Kosaka, M. Mitsunaga, P.L. Choyke, and H. Kobayashi. In vivo molecular imaging using nanomaterials: General in vivo characteristics of nano-sized reagents and applications for cancer diagnosis. *Molecular Membrane Biologie*, 0:1–12, 2010.

[26] B. Nikoobakht and M.A. El-Sayed. Preparation and growth mechanism of gold nanorods (nrs) using seed-mediated growth method. *Chemical Materials*, 15:1957–1962, 2003.

[27] Y.H. Su, W.H. Lai, W.Y. Chen, M.H. Hon, and S.H. Chang. Surface plasmon resonance of gold nano-sea-urchin. *Applied Physics Letters*, 90:181905–1 – 181905–3, 2007.

[28] J.E. Millstone, G.S. Metraux, and C.A. Mirkin. Controlling the edge length of gold nanoprisms via a seed-mediated approach. *Advanced Functional Materials*, 16:1209–1214, 2006.

[29] Z.R. Shen, K. Miyabayashi, M. Higashimoto, T. Shimoda, and M. Miyake. Single-crystalline gold nanodisks prepared by the shape transformation under uv irradiation from nanoparticles protected with discotic liquid crystalline ligands. *Chemistry Letters*, 37:1276–1277, 2008.

[30] T. Pham, J. B. Jackson, N. J. Halas, and T. R. Lee. Preparation and characterization of gold nanoshells coated with self-assembled monolayers. *Langmuir*, 18(12):4915–4920, 2002.

[31] P.S. Kumar, I. Pastoriza-Santos, B. Rodriguez-Gonzalez, F.J. Garcia de Abajo, and L.M. Liz-Marzan. High-yield synthesis and optical response of gold nanostars. *Nanotechnology*, 19:1–6, 2008.

[32] C.C. Berry, J.M. de la Fuente, M. Mullin, S.W.L. Chu, and A.S.G. Curtis. Nuclear localization of hiv-1 tat functionalized gold nanoparticles. *IEEE Translational Nanobioscience*, 6:262–269, 2007.

[33] P.S. Ghosh, C.-K. Kim, G. Han, N.S. Forbes, and V.M. Rotello. Efficient gene delivery vectors by tuning the surface charge density of amino acid-functionalized gold nanoparticles. *ACS Nano*, 2:2213–2218, 2008.

[34] C.J. Mu, D.A. LaVan, R.S. Langer, and B.R. Zetter. Self-assembled gold nanoparticle molecular probes for detecting proteolytic activity invivo. *ACS Nano*, 4:1511–1520, 2010.

[35] D.P. ONeal, L.R. Hirsch, N.J. Halas, Payne J.D., and J.L. West. Photothermal tumor ablation in mice using near infrared-absorbing nanoparticles. *Cancer letters*, 209:171–176, 2004.

[36] E. Oh, M.-Y. Hong, D. Lee, S.-H. Nam, H.C. Yoon, and H.-S. Kim. Inhibition assay of biomolecules based on fluorescence resonance energy transfer (fret) between quantum dots and gold nanoparticles. *Journal of the American Chemical Society*, 127:3270–3271, 2005.

[37] E. Smith and G. Geoffrey Dent. *Modern Raman Spectroscopy - A practical Approach*. John Wiley & Sons, 2006.

[38] P.R.T. Jess, V., V. Garcs-Shavez, A.C. Riches, C.S. Herrington, and K. Dholakia. Simultaneous raman micro-spectroscopy of optically trapped and stacked cells. *Journal of Raman Spectroscopy*, 2007.

[39] Roux K. "immunoglobulin structure and function as revealed by electron microscopy". *International Archive of Allergy Immunology*, 120:85–99, 1999.

[40] M. Fleischmann, P.J. Hendra, and A.J. McQuillan. Raman spectra of pyridine adsorbed at a silver electrode. *Chemical Physics Letters*, 2:163–166, 1974.

[41] D.L. Jeanmaire and R.P. Van Duyne. Surface raman spectroelectrochemistry part i. heterocyclic, aromatic and aliphatic amines adsorbed on the anodized silver electrode. *J. Electroanal. Chem.*, 84:1–20, 1977.

[42] R.B.M. Schasfoort and A.J. Tudos. *Handbook of Surface Plasmon Resonance*. RSC Publishing, 2008.

[43] L. Novotny and B. Hecht. *Prinicples of Nano-Optics*. Cambridge University Press, 2006.

[44] S. Nie and S. R. Emory. Probing single molecules and single nanoparticles by surface-enhanced raman scattering. *Science*, 275:1102–1106, 1997.

[45] K. Ryu, A.J. Haes, H.Y. Park, S. Nah, H. Kim, J.Chung, Yoon M.Y., and S.H. Han. Use of peptide for selective and sensitive detection of an anthrax biomarker via peptide recognition and surface-enhanced raman scattering. *Journal of Raman Spectroscopy*, 41:121–124, 2010.

[46] M. Feng and H. Hiroyasu Tachikawa. Surface-enhanced resonance raman spectroscopic characterization of the protein native structure. *Journal of the American Chemical Society*, 130:74437448, 2008.

[47] A. MacAskill, D. Crawford, D. Duncan Graham, and K. Faulds. Dna sequence detection using surface-enhanced resonance raman spectroscopy in a homogeneous multiplexed assay. *Anal. Chem.*, 81:81348140, 2009.

[48] J. Kneipp, H. Kneipp, B. Wittig, and K. Kneipp. One- and two-photon excited optical ph probing for cells using surface-enhanced raman and hyper-raman nanosensors. *Nano Letters*, 7:2819–2823, 2007.

[49] E. Potma, J. Jones, D.Cheng, X.S. Xie, and J. Ye. High-sensitivity coherent anti-stokes raman scattering microscopy with two tightly synchronized. *Optics Letters*, 2002.

[50] F. Lgar, C.L. Evans, and X.S. Ganikhanov, F. Xie. Towards cars endoscopy. *Optics Express*, 14:4427–4431, 2006.

[51] A. Hopt and E. Neher. Highly nonlinear photodamage in two-photon fluorescence microscopy. *Biophysical Journal*, 80, 2001.

[52] International Union of Pure and Applied Chemistry. *Compendium of Chemical Terminology*. Internet edition.

[53] Pier G.B., Lyczak J.B., and Wetzler L.M. *Immunology, Infection, and Immunity*. ASM Press, 2004.

[54] H. Park, L. Chen, Y.H. Lee, S.W. Son, and J. Choo. Sers imaging of her2-overexpressed mcf7 cells using antibody-conjugated gold nanorods. *Physical Chemistry Chemical Physics*, 11:7444 – 7449, 2009.

[55] M.J. Farabee. *online*, Anti-body mediated immunity, 2001. URL http://www.emc.maricopa.edu/faculty/farabee/biobk/biobookimmun.html.

[56] C. Tuerk and L. Gold. Systematic evolution of ligands by exponential enrichment: Rna ligands to bacteriophage t4 dna polymerase. *Science*, 249: 505–510, 1990.

[57] M. Djordjevic. Selex experiments: New prospects, applications and data analysis in inferring regulatory pathways, biomolecular engineering. 24:179–189, 2007.

[58] B.H.J. Bunka and Stockley P.G. Aptamers come of age - at last. *Nature Reviews*, 4:589–596, 2006.

[59] A. Nitsche, A. Kurth, A. Dunkhorst, O. Pnke, H. Sielaff, W. Junge, D. Muth, F. Scheller, W. Stcklein, C. Dahmen, G. Pauli, and A. Kage. One-step selection of vaccinia virus-binding dna aptamers by monolex,. *BMC Biotechnology*, 4:48–54, 2007.

[60] K. N. Heck, B. G. Janesko, G. E. Scuseria, N. J. Halas, and M. S. Wong. Observing metal-catalyzed chemical reactions in situ using surface-enhanced raman spectroscopy on pd-au nanoshells. *Journal American Chemical Society*, 2008.

[61] Y.-J. Liu, Z.-Y. Zhang 1, R.A. Dluhy, and Y.-P. Zhao. The sers response of semiordered ag nanorod arrays fabricated by template oblique angle deposition. 2010. URL 10.1002/jrs.2567.

[62] D.G. Duff, A. Baiker, and P.P. Edwards. A new hydrosol of gold clusters. 1. formation and particle size variation. *Langmuir*, 9:2301–2309, 1993.

[63] S.E. Skrabalak, J. Chen, L. Au, Li-X. Lu, X, and Y. Xia. Gold nanocages for biomedical applications. *Advanced Materials*, 19:3177–3184, 2007.

[64] B.E. Brinson, J.B. Lassiter, C.S. Levin, R. Bardhan, N. Mirin, and N.J. Halas. Nanoshells made easy: Improving au layer growth on nanoparticle surfaces. *Langmuir*, 24:14166–14171, 2008.

[65] F. Lux, F. Lerouge, J. Bosson, L. Lemercier, G. Andraud, G. Vitrant, P.L. Baldeck, F. Chassagneux, and S. Stephane Parola. Gold hollow spheres obtained using an innovative emulsion process: towards multifunctional au nanoshells. *Nanotechnology*, 20:355603–355609, 2009.

[66] R.A. Alvarez-Puebla, D.J. Ross, G.-A. Nazri, and R.F. Aroca. Surface-enhanced raman scattering on nanoshells with tunable surface plasmon resonance. *Langmuir*, 21:10504–10508, 2005.

[67] Huang C.C., Hwu J.R., Su W.C., Shieh D.B., Tzeng Y., and Yeh C.S. Surfactant-assisted hollowing of cu nanoparticles involving halide-induced corrosion-oxidation processes. *Chemistry*, 12(14):3805–3810, 2006.

[68] M.R. Rasch, K.V. Sokolov, and B.A. Korgel. Limitations on the optical tunability of small diameter gold nanoshells. *Langmuir*, 25(19):11777–11785, 2009.

[69] C.L. Nehl, N.K. Grady, G.P. Goodrich, F. Tam, N.J. Halas, and J.S. Hafner. Scattering spectra of single gold nanoshells. *Nano Letters*, 4(12):2355–2359, 2004.

[70] E. Prodan, P. Nordlander, and N.J. Halas. Electronic structure and optical properties of gold nanoshells. *Nano Letters*, 3:1411–1415, 2003.

[71] A.S. Kirakosyan and T.V. Shahbazyan. Vibrational modes of metal nanoshells and bimetallic core-shell nanoparticles. *Journal of Chemical Physics*, 129:34708.1–34708.7, 2008.

[72] B.E. Brinson, J.B. Lassiter, C.S. Levin, R. Bardhan, N. Mirin, and N.J. Halas. Nanoshells made easy: Improving au layer growth on nanoparticle surfaces. *Langmuir*, 24:14166–14171, 2008.

[73] S.L. Westcott, , J.B. Jackson, C. Radloff, and N. J. Halas. Relative contributions to the plasmon line shape of metal nanoshells. *PHYSICAL REVIEW B*, 66:155431–1–5, 2002.

[74] B.E. Brinson, J.B. Lassiter, C.S. Levin, R. Bardhan, N. Mirin, and N.J. Halas. Nanoshells made easy: improving au layer growth on nanoparticle surfaces. *Langmuir*, 24(24):14166–14171, 2008.

[75] T.C. Preston and R. Signorell. Growth and optical properties of gold nanoshells prior to the formation of a continuous metallic layer. *ACSNano*, 3(11), 2009.

[76] Y. Wanga, W. Qiana, Y. Tana, and S. Dinga. A label-free biosensor based on gold nanoshell monolayers for monitoring biomolecular interactions in diluted whole blood. *Biosensors and Bioelectronics*, 23(7):1166–1170, 2008.

[77] S. W. Bishnoi, C. J. Rozell, C. S. Levin, M. K. Gheith, B. R. Johnson, D. H. Johnson, and N. J. Halas. All-optical nanoscale ph meter. *Nano Letters*, 6 (8):3277–3281, 2006.

[78] R. Bardhan, N. K. Grady, J. R. Cole, A. Joshi, and N. J. Halas. Fluorescence enhancement by au nanostructures: nanoshells and nanorods. *ACS Nano*, 3 (3):744–52, 2009.

[79] C.S. Levin, J. Kundu, B.G. Janesko, G.E. Scuseria, R.M. Raphael, and N.J. Halas. Interactions of ibuprofen with hybrid lipid bilayers probed by complementary surface-enhanced vibrational spectroscopies. *Journal Physical Chemistry B*, 112:14168–14175, 2008.

[80] P. Zhang and Y. Guo. Surface-enhanced raman scattering inside metal nanoshells. *Journal of the American Chemical Society*, 131:3808–3809, 2009.

[81] S. Lal, S.E. Clare, and N.J. Halas. Nanoshell-enabled photothermal cancer therapy: Impending clinical impact. *Accounts of Chemical Research*, 41(12): 1842–1851, 2008.

[82] E.W. Goodpasture. "the significance of certain pulmonary lesions in relation to the etiology of influenza". *American Journal of Medical Sciences*, 158: 863–870, 1919.

[83] *Dorlands Medical Dictionary.* Elsevier, 2007.

[84] J. Zou, S. Hannier, L.S. Cairns, R.B. Baker, A.J. Rees, A.N. Turner, and R.G. Phelps. Healthy individuals have goodpasture autoantigen-reactive t cells. *Journal of the American Nephorological Society*, 19:396–404, 2008.

[85] H. Rochefort, F. Capony, and M. Garcia. Cathepsin d: a protease involved in breast cancer metastasis. *Cancer Metastasis Reviews*, 9:321–331, 1990.

[86] E. Liaudet-Coopman, M. Beaujouin, D. Derocq, M. Garcia, M. Glondu-Lassis, V. Laurent-Matha, C. Prébois, H. Rochefort, and F. Vignon. Cathepsin d: newly discovered functions of a long-standing aspartic protease in cancer and apoptosis. *Cancer Letters*, 237:167–179, 2006.

[87] R. Moger, P. Montcourrier, T. Maudelonde, J.P. Brouillet, A. Pagès, and F. Laffargue. Cathepsin d immunostaining in paraffin-embedded breast cancer cells and macrophages. correlation with cytosolic assay. *Human Pathology*, 25:863–871, 1994.

[88] J.P. Brouillet, F. Dufour, G. Lemamy, M. Garcia, N. Schlup, and J. Grenier. Increased cathepsindlevel in serum of patients with metastatic breast carcinoma detected with a specific procathepsin d immunoassay. *Cancer*, 79: 2132–2136, 1997.

[89] H.D. Soule, J. Vazguez, A. Long, S. Albert, and M. Brennan. A human cell line from a pleural effusion derived from a breast carcinoma. *Journal of the National Cancer Institute*, 51:1409 1416, 1973.

[90] D.H. Lee, D. Wenkert, M.P. Whyte, M.T. Trese, and O.A. Cruz. Congenital blindness and osteoporosispseudoglioma syndrome. *Journal of American Association for Pediatric Ophthalmology and Strabismus*, 7:75–77, 2003.

[91] T.C. Mettenleiter, B.G. Klupp, and H. Granzow. Herpesvirus assembly: An update. *Virus Research*, 143:222–235, 2009.

[92] T.C. Mettenleiter. *Pseudorabies virus. and Encyclopedia of Virology.* Elsevier, Oxford, 2008.

[93] P.D. Jadzinsky, G. Calero, C.J. Ackerson, D.A. Bushnell, and R.D. Kornberg. Structure of a thiol monolayerprotected gold nanoparticle at 1.1 resolution. *Science*, 318(430), 2007.

[94] Thermo Fisher Scientific Inc. Edc (1-ethyl-3-[3-dimethylaminopropyl]carbodiimide hydrochloride). URL http://www.piercenet.com/products/browse.cfm?fldID=02030312.

[95] J.X. Cheng, A. Volkmer, and X.S. Xie. Theoretical and experimental characterization of coherent anti-stokes raman scattering microscopy. *Journal of Optical Society of America B*, 19(6):1363–1375, 2002.

[96] L.S. Ma, R.K. Shelton, M.M. Kapteyn, H.C. andMurnane, and J. Ye. Sub-10-femtosecond active synchronization of two passively mode-locked ti : sapphire oscillators. *Physical Reviews A*, 64(2):artno. 21802, January 2001.

[97] Y. Y Takagi, T. Kobayashi, K. Yoshihara, and S. Imamura. Multiple-and single-shot autocorrelator based on two-photon conductivity in semiconductors. *Optics Letters*, January 1992.

[98] T. Minamikawa, M.Araki T.Kobayashi M. Tanimoto, N.Hashimoto, and S. Fujita, K.Kawata. Jitter reduction of two synchronized picosecond mode-locked lasers using balanced cross-correlator with two-photon detectors. *Applied Physics Letters*, 89(19), 2006.

[99] P. Ghazal, M. Messerle, K. Osborn, and A. Angulo. An essential role of the enhancer for murine cytomegalovirus in vivo growth and pathogenesis. *Journal Virology*, 77:3217–3228, 2003.

[100] A. Angulo, P. Ghazal, , and M. M Messerle. The major immediate-early gene ie3 of mouse cytomegalovirus is essential for viral growth. *Journal Virology*, 74(23):11129–11136, 2000.

[101] D.J. Stevenson, D.J. Carnegie, B. Agate, F. Gunn-Moore, and K. Dholakia. Long-term cell culture on a microscope stage: The carrel flask revisited. *Microscopy and Analysis*, 22:9–11, 2008.

[102] Chithrani B. D., , Ghazani A. A., , and Chan W. C. W. Determining the size and shape dependence of gold nanoparticle uptake into mammalian cells. *Nano Letters*, 6(4):662–668, 2006.

[103] L. Cognet, C. Tardin, D. Boyer, D. Choquet, P. Tamarat, and B. Lounis. Single metallic nanoparticle imaging for protein detection in cells. *Proceedings of the National Academy of Sciences of the United States of America*, 100(20):11350–5, 2003.

[104] Y. Hu, T. Litwin, A. R. Nagaraja, B. Kwong, J. Katz, N. Watson, and D. J. Irvine. Cytosolic delivery of membrane-impermeable molecules in dendritic cells using ph-responsive core-shell nanoparticles. *Nano Letters*, 7(10):3056–3064, 2007.

[105] N. Jarvis, R. M.and Law, I. T. Shadi, P. O'Brien, J. R. Lloyd, and R. Goodacre. Surface-enhanced raman scattering from intracellular and extracellular bacterial locations. *Analytical Chemistry*, 80(17):6741–6, 2008.

[106] L. L. Ma, M. D. Feldman, J. M. Tam, A. S. Paranjape, K. K. Cheruku, T. A. Larson, J. O. Tam, D. R. Ingram, V. Paramita, J. W. Villard, J. T. Jenkins, T. Wang, G. D. Clarke, R. Asmis, K. Sokolov, B. Chandrasekar, T. E.

Milner, and K. P. Johnston. Small multifunctional nanoclusters (nanoroses) for targeted cellular imaging and therapy. *ACS Nano*, 2009.

[107] O. Harush-Frenkel, E. Rozentur, S. Benita, and Y. Altschuler. Surface charge of nanoparticles determines their endocytic and transcytotic pathway in polarized mdck cells. *Biomacromolecules*, 9:435–443, 2 2008.

[108] S. Kumar, N. Harrison, R. Richards-Kortum, and K. Sokolov. Plasmonic nanosensors for imaging intracellular biomarkers in live cells. *Nano Letters*, 7(5):1338–43, 2007.

[109] I. H. El-Sayed, X. Huang, and M. A. El-Sayed. Surface plasmon resonance scattering and absorption of anti-egfr antibody conjugated gold nanoparticles in cancer diagnostics: Applications in oral cancer. *Nano Letters*, 5: 829–834, 5 2005.

[110] J. M. Dubach, D. I. Harjes, and H. A. Clark. Fluorescent ion-selective nanosensors for intracellular analysis with improved lifetime and size. *Nano Letters*, 7(6):1827–1831, 2007.

[111] A. M. Gobin, M. H. Lee, N. J. Halas, W. D. James, R. A. Drezek, and J. L. West. Near-infrared resonant nanoshells for combined optical imaging and photothermal cancer therapy. *Nano Letters*, 7:1929–1934, 7 2007.

[112] L. R. Hirsch, A. M. Gobin, A. R. Lowery, F. Tam, R. A. Drezek, N. J. Halas, and J. L. West. Metal nanoshells. *Ann Biomed Eng*, 34:15–22, 1 2006.

[113] C. Liu, C. C. Mi, and B. Q. Li. Energy absorption of gold nanoshells in hyperthermia therapy. *IEEE Trans Nanobioscience*, 7(3):206–14, 2008.

[114] A. A. Bhirde, V. Patel, J. Gavard, G. Zhang, A. A. Sousa, A. Masedunskas, R. D. Leapman, R. Weigert, J. S. Gutkind, and J. F. Rusling. Targeted killing of cancer cells in vivo and in vitro with egf-directed carbon nanotube-based drug delivery. *ACS Nano*, 3(2):307–316, 2009.

[115] A. D. Maynard, R. J. Aitken, T. Butz, V. Colvin, K. Donaldson, G. Oberdorster, M. A. Philbert, J. Ryan, A. Seaton, V. Stone, S. S. Tinkle, L. Tran, N. J. Walker, D. Warheit, and B. Safe handling of nanotechnology. *Nature*, 444(7117):267–269, 2006.

[116] J. Muller, I. Decordier, P. H. Hoet, N. Lombaert, L. Thomassen, F. Huaux, D. Lison, and M. Kirsch-Volders. Clastogenic and aneugenic effects of multi-wall carbon nanotubes in epithelial cells. carcinogenesis. *Carcinogenesis*, 29 (2):427–433, 2008.

[117] C. A. Poland, R. Duffin, I. Kinloch, A. Maynard, W. Wallace, A . H., A. Seaton, V. Stone, S. Brown, W. MacNee, and K. Donaldson. Carbon nanotubes introduced into the abdominal cavity of mice show asbestos-like pathogenicity in a pilot study. *Nature Nano*, 3(7):423–428, 2008.

[118] M.A. Ochsenkühn, P.R.T. Jess, H. Stoquert, K. Dholakia, and C.J. Campbell. Nanoshells for surface-enhanced raman spectroscopy in eukaryotic cells: Cellular response and sensor development. *ACS Nano*, 3(11):3613–3621, 2009.

[119] H. Dumortier, S. Lacotte, G. Pastorin, R. Marega, W. Wu, D. Bonifazi, J.-P. Briand, M. Prato, S. Muller, and A. Bianco. Functionalized carbon nanotubes are non-cytotoxic and preserve the functionality of primary immune cells. *Nano Letters*, 6(12):3003–3003, 2006.

[120] C. E. Talley, L. Jusinski, C. W. Hollars, S. M. Lane, and T. Huser. Intracellular ph sensors based on surface-enhanced raman scattering. *Analytical Chemistry*, 76(23):7064–7068, 2004.

[121] H.-W. Tang, X. B. Yang, J. Kirkham, and D. A. Smith. Probing intrinsic and extrinsic components in single osteosarcoma cells by near-infrared surface-enhanced raman scattering. *Analytical Chemistry*, 79(10):3646–3653, 2007.

[122] R. Shukla, V. Bansal, M. Chaudhary, A. Basu, R. R. Bhonde, and M. Sastry. Biocompatibility of gold nanoparticles and their endocytotic fate inside the cellular compartment: a microscopic overview. *Langmuir*, 21(23):10644–54, 2005.

[123] N. Wong Shi Kam and H. Dai. Carbon nanotubes as intracellular transporters for proteins and dna: An investigation of the uptake mechanism and pathway. *Angewandte Chemie*, 118(4):591–595, 2006.

[124] H. Jin, D. A. Heller, R. Sharma, and M. S. Strano. Size-dependent cellular uptake and expulsion of single-walled carbon nanotubes: Single particle tracking and a generic uptake model for nanoparticles. *ACS Nano*, 3(1): 149–158, 2009.

[125] L. R. Hirsch, J. B. Jackson, A. Lee, N. J. Halas, and J. L. West. A whole blood immunoassay using gold nanoshells. *Analalytical Chemistry*, 75(10): 2377–81, 2003.

[126] S.J. Oldenberg, S.L. Westcott, and N.J. Halas. Nanoengineering of optical resonances. *Chemical Physics Letters*, pages 243–247, 1998.

[127] R. A. Alvarez-Puebla, D. J. Ross, G. A. Nazri, and R. F. Aroca. Surface-enhanced raman scattering on nanoshells with tunable surface plasmon resonance. *Langmuir*, 21(23):10504–8, 2005.

[128] A. M. Gobin, M. H. Lee, N. J. Halas, W. D. James, R. A. Drezek, and J. L. West. Near-infrared resonant nanoshells for combined optical imaging and photothermal cancer therapy. *Nano Letters*, 7(7):1929–34, 2007.

[129] J. B. Lassiter, J. Aizpurua, L. I. Hernandez, D. W. Brandl, I. Romero, S. Lal, J. H. Hafner, P. Nordlander, and N. J. Halas. Close encounters between two nanoshells. *Nano Letters*, 8(4):1212–8, 2008.

[130] C. L. Nehl, N. K. Grady, G. P. Goodrich, F. Tam, N. J. Halas, and J. H. Hafner. Scattering spectra of single gold nanoshells. *Nano Letters*, 4(12): 2355–2359, 2004.

[131] C. S. Levin, S. W. Bishnoi, N. K. Grady, and N. J. Halas. Determining the conformation of thiolated poly(ethylene glycol) on au nanoshells by surface-enhanced raman scattering spectroscopic assay. *Analytical Chemistry*, 78 (10):3277–3281, 2006.

[132] B.J. Marquis, K.L. Braun, and C.L. Haynes. Analytical methods to assess nanoparticle toxicity. *Analyst*, 134:425–439, 2009.

[133] A. Kerma, O. Uzun, Y. Hu, Y. Hu, H.-S. Han, N. Watson, S. Chen, D. J. Irvine, and F. Stellacci. Surface-structure-regulated cell-membrane penetration by monolayer-protected nanoparticles. *Nature Materials*, 7(7):588–595, 2008.

[134] J. Rejman, V. Oberle, I. S. Zuhorn, and D. Hoekstra. Size-dependent internalization of particles via the pathways of clathrin- and caveolae-mediated endocytosis. *Biochemical Journal*, 377(1):159–169, 2004.

[135] I. R. Nabi and P. U. Le. Caveolae/raft-dependent endocytosis. *Journal of Cell Biology*, 161(4):673–677, 2003.

[136] R. G. W. Anderson. Multiple endocytic pathways. *Journal of Investigative Dermatology*, 99(5):7–9, 1992.

[137] M.H. Chowhudry, C.J. Campbell, E. Theofanidou, L. Seung Joon, G. Baldwin, A . Sing, A.T. Yeh, J. Crain, P. Ghazal, and G.L. Cote. Surface enhanced raman spectroscopy (sers) for the detection of intracellular constituents using gold nanoshells. *Progress in biomedical optics and imaging*, 7(22):609905.1–609905.8, 2006.

[138] Y. Roiter, M. Ornatska, A. R. Rammohan, J. Balakrishnan, D. R. Heine, and S. Minko. Interaction of nanoparticles with lipid membrane. *Nano Letters*, 8(3):941–944, 2008.

[139] J. Kneipp, H. Kneipp, M. McLaughlin, D. Brown, and K. Kneipp. In vivo molecular probing of cellular compartments with gold nanoparticles and nanoaggregates. *Nano Letters*, 6(10):2225–2231, 2006.

[140] C. Eggeling, C. Ringemann, R. Medda, G. Schwarzmann, K. Sandhoff, S. Polyakova, V. N. Belov, B. Hein, C. von Middendorff, A. Schonle, and S. W. Hell. Direct observation of the nanoscale dynamics of membrane lipids in a living cell. *Nature*, 457(7233):1159–1162, 2009.

[141] A.M. Alkilany, C.R. Hexel, T.J. Shaw, C.J. Murphy, and M.D. Wyatt. Cellular uptake and cytotoxicity of gold nanorods: Molecular origin of cytotoxicity and surface effects. *Small*, 5(6):701–708, 2009.

[142] S. Lal, S. E. Clare, and N. J. Halas. Surface-enhanced raman scattering on tunable plasmonic nanoparticle substrates. *Proceedings of the National Academy of Sciences of the United States of America*, 101(52):17930–17935, 2004.

[143] M. Cooper. Label-free screening of bio-molecular interactions. *Analytical and Bioanalytical Chemistry*, 377(5):834–842, 2003.

[144] C. E. Talley, J. B. Jackson, C. Oubre, N. K. Grady, C. W. Hollars, S. M. Lane, P. Huser, T. R. Nordlander, and N. J. Halas. Surface-enhanced raman scattering from individual au nanoparticles and nanoparticle dimer substrates. *Nano Letters*, 5(8):1569–1574, 2005.

[145] J. Kneipp, H. Kneipp, B. Wittig, and K. Kneipp. One- and two-photon excited optical ph probing for cells using surface-enhanced raman and hyper-raman nanosensors. *Nano Letters*, 7(9):2819–2823, 2007.

[146] R.L. Rich and D.G. Myszk. Higher-throughput, label-free, real-time molecular interaction analysis. *Analytical Biochemistry*, 361(1):1–6, 2007.

[147] J. G. Duguid, V. A. Bloomfield, J. M. Benevides, and G. J. Thomas. Dna melting investigated by differential scanning calorimetry and raman spectroscopy. *Journal of Raman Spectroscopy*, 71(6):3350–3360, 1996.

[148] K. Willets. Surface-enhanced raman scattering (sers) for probing internal cellular structure and dynamics. *Analytical and Bioanalytical Chemistry*, 394(1):85–94, 2009.

[149] C.-C. Lin, Y.-M. Yang, Y.-F. Chen, T.-S. Yang, and H.-C Chang. A new protein a assay based on raman reporter labeled immunogold nanoparticles. *Biosensors and Bioelectronics*, 24:178–183, 2008.

[150] J. Jiwei Chen, J. Jianhui Jiang, X. Xing Gao, G. Guokun Liu, G. Guoli Shen, and r. Ruqin Yu. A new aptameric biosensor for cocaine based on surface-enhanced raman scattering spectroscopy. *Chemistry*, 14(27):8374–8382, 2008.

[151] Y. Wang, H. Wei, B. Li, W. Ren, S. Guo, S. Dong, and E. Wang. *Chemical Communications*, 28:5220–5222, 2007.

[152] H.J. Zheng, P.C. Jiang, J.-H. Shen, G.-L. Yu, and R.-Q. Liu. Electrostatic interaction based approach to thrombin detection by surface-enhanced raman spectroscopy. *Analytical Chemistry*, 81:87–93, 2008.

[153] K. Padmanabhan and A. Tulinsky. An ambiguous structure of a dna 15-mer thrombin complex. *Acta Crystallographica Section D*, 52(2):272–282, 1996.

[154] S. Ogasawara and H. Maeda. Reversible photoswitching of a g-quadruplex. *Angewandte Chemie*, 121:1–5, 2009.

[155] C. Sealy. Self-assembly leaves no stain: Nanoparticles. *Nanotoday*, 1:13, 2006.

[156] C.E. Talley, J.B. Jackson, C. Oubre, N.K. Grady, C.W. Hollars, S.M. Lane, T.R. Huser, P. Nordlander, and N.J. Halas. Surface-enhanced raman scattering from individual au nanoparticles and nanoparticle dimer substrates. *Nano Letters*, 5(8):1569–1574, 2005.

[157] T.M. Herne and M.J. Tarlov. Characterization of dna probes immobilized on gold surfaces. *Journal of the American Chemical Society*, (38):2016–2020, 1997.

[158] B. E. Billinghurst, S. A. Oladepo, and G. R. Loppnow. ph-dependent uv resonance raman spectra of cytosine and uracil. *The Journal of Physical Chemistry B*, 113(20):7392–7397, 2009.

[159] J. Moger, Gribbon, A. P. Sewing, and M. G. Winlove. Feasibility study using surface-enhanced raman spectroscopy for the quantitative detection of tyrosine and serine phosphorylation. *Biochimica et Biophysica Acta (BBA) - General Subjects*, 1770(6):912–918, 2007.

[160] S. Yarasi, B.E. Billinghurst, and G.R. Loppnow. Vibrational properties of thymine, uracil and their isotopomers. *Journal of Raman Spectroscopy*, 38 (9):1117–1126, 2007.

[161] D.Tam F.Halas N.J. Barhoumi, A.Zhang. Surface-enhanced raman spectroscopy of dna. *Journal of the American Chemical Society*, 130(16):5523–5529, 2008.

[162] E.Takase M.Hasegawa H.Morita Y.Yamazaki H.Sode K.Ikebukuro K. Yoshida, W.Mochizuki. Selection of dna aptamers against insulin and construction of an aptameric enzyme subunit for insulin sensing. *Biosensors and Bioelectronics*, 24(5):1116–1120, 2009.

[163] R.C. Maher, L.F. Cohen, E.C. Le Ru, P.G. Etchegoin, and J.C. Gallop. Temperature-dependent anti-stokes/stokes ratios under surface-enhanced raman scattering conditions. *Journal of Physical Chemistry B*, 110:6797–6803, 2006.

[164] S.S. Bale, S.J. Kwon, D.A. Shah, A. Banerjee, J.S. Dordick, and R.S. Kane. Nanoparticle-mediated cytoplasmic delivery of proteins to target cellular machinery. *ACS Nano*, 2010. URL 10.1021/nn901586e.

[165] F. Wei, D. Zhang, N.J. Halas, and J.D. Hartgerink. Aromatic amino acids providing characteristic motifs in the raman and sers spectroscopy of peptides. *Journal of Physical Chemistry B*, 112:9158–9164, 2008.

[166] M. Feng and H. Tachikawa. Surface-enhanced resonance raman spectroscopic characterization of the protein native structure. *Journal of the American Chemical Society*, 130(23):74437448, 2008.

[167] F.Q. SCHAFER and G.R. BUETTNER. Redox envrionment of the cell as viewed through the redox stater of the glutathione disulfide/glutathione couple. *Free Radical Biology & Medicine*, 30(11):1191–1212, 2001.

[168] E. Podstawka, G. Niaura, and L.M. Proniewicz. Potential-dependent studies on the interaction between phenylalanine-substituted bombesin fragments and roughened ag, au, and cu electrode surfaces. *The Journal of Physical Chemistry B*, 114:1010–1029, 2010.

[169] E. Podstawka, Y. Ozaki, and L.M. Proniewicz. Part iii: Surface-enhanced raman scattering of amino acids and their homodipeptide monolayers deposited onto colloidal gold surface. *Applied Spectroscopy*, 59:1516–1526, 2005.

[170] J.L. Myers and A.D. Well. *Research Design and Statistical Analysis*. Lawrence Erlbaum, 2003.

[171] F. Ota, S. Higuchi, Y. Gohshi, K. Furuya, M. Ban, and M. Kyoto. Some considerations of the sers effect of l-phenylalanine in the near-infrared region using silver colloid solution. *Journal fo Raman spectroscopy*, 28:849–854, 1997.

[172] J. De Gelder, K. De Gussem, P. Vandenabeele, and L. Luc Moens. Reference database of raman spectra of biological molecules. *Journal of Raman spectroscopy*, 38, 2007.

[173] A.L. Jenkins, R.A. Larsen, and T.B. Williams. Characterization of amino acids using raman spectroscopy. *Spectrochimica Acta Part A*, 61:1585–1594, 2005.

[174] E.T. Baldwin, T.N. Bhat, S. Gulnik, M.V. Hosur, R.C. Sowder, R.E. Cachau, J. Collins, A.M. Silva, and J.W. Erickson. Crystal structures of native and inhibited forms of human cathepsin d: Implications for lysosomal targeting and drug design. *Proc. Natl. Acad. Sci.*, 90:6796–6800, 1993.

[175] H. Rochefort, F. Capony, and M. Garcia. Cathepsin d: A protease involved in breast cancer metastasis. *Cancer and Metastasis Reviews*, 9:321–331, 1990.

[176] T. Fujimoto, J. Ohsaki, Y . Cheng, M. Suzuki, and Y. Shinohara. Lipid droplets: a classic organelle with new outfits. *Histochemical Cell Biology*, 130(2):263–279, 2008.

[177] J. Mclauchlan. Lipid droplets and hepatitis c virus infection. *BBA - Molecular and Cell Biology of Lipids*, pages 1–8, 2009.

[178] R.K. Lyn, D.C. Kennedy, S.M. Sagan, D.R. Blais, A.F. Rouleau, Y.Pegoraro, X.S. Xie, A. Stolow, and J.P. Pezacki. Direct imaging of the disruption of hepatitis c virus replication complexes by inhibitors of lipid metabolism. *Virology 394 (2009) 130142*, 394:130142, 2009.

[179] W. Muranyi, J. Haas, M. Wagner, G. Krohne, and U.H. Koszinowski. Cytomegalovirus recruitment of cellular kinases to dissolve the nuclear lamina. *Science*, 297:854–857, 2002.